

Lithogeochemical vectors for hydrothermal processes in the Strange Lake peralkaline granitic REE-Zr-Nb deposit

Alexander P. Gysi^{*1}, Anthony E. Williams-Jones² and Patrick Collins³

¹Department of Geology and Geological Engineering, Colorado School of Mines, 1516
Illinois Street, Golden, CO 80401

²Department of Earth and Planetary Sciences, McGill University, 3450 University Street,
Montreal, Quebec, Canada, H3A 2A7

³Vulcan Minerals Incorporated, 333 Duckworth Street, St. John's, Newfoundland &
Labrador, Canada, A1C 1G9

* Corresponding author: e-mail, agysi@mines.edu

Tel: +1 303 273 3828

Revised manuscript submitted to Economic Geology

21 ABSTRACT

22 Extreme enrichment and post-magmatic hydrothermal mobilization of the rare earth
23 elements (REE), Zr and Nb have been reported for a number of anorogenic peralkaline
24 intrusions, including the world-class REE-Zr-Nb deposit at Strange Lake, Quebec,
25 Canada. Establishing lithogeochemical vectors for these types of deposits is a challenging
26 task because the effects of hydrothermal processes on element distribution are poorly
27 known and the relationships of alteration types to mineralization stages have not been
28 well documented. Here, we present results of a detailed mineralogical and geochemical
29 investigation involving a dataset of over 500 mineral and bulk rock analyses of a NE-SW
30 section through the potential ore zone at Strange Lake. Based on these data, we develop a
31 model that explains the role of hydrothermal processes in concentrating metals in
32 peralkaline granitic systems, and identify lithogeochemical vectors for their exploration.

33 The B Zone, located along the northwestern margin of the Strange Lake pluton,
34 contains a lens-shaped pegmatite-rich domain comprising sub-horizontal sheets of
35 pegmatites hosted by granites with a total indicated resource of 278 Mt grading 0.93
36 wt.% total rare earth oxides (TREO), of which 39 % are heavy (H)REE. Within this
37 resource, there is an enriched zone containing 20 Mt of ore grading 1.44 wt.% TREO, of
38 which 50 % are HREE. The pegmatites are characterized by a core enriched in quartz,
39 fluorite and light (L)REE fluorocarbonates, and a granitic border enriched in
40 zirconosilicates and granitic minerals. The pegmatite sheets and surrounding granites
41 evolved in three essential stages: I) a magmatic stage, II) a near neutral hydrothermal
42 stage involving their interaction with NaCl-bearing orthomagmatic fluids, and III) an
43 acidic hydrothermal stage (comprising high (IIIa) and low (IIIb) temperature substages)
44 that resulted from their interaction with pegmatite-sourced HCl-HF-bearing fluids. Stage
45 IIIa led to pseudomorphic mineral replacement reactions (e.g., Na-Ca exchange during
46 replacement of zirconosilicates) and formation of an aegirinization/hematization halo
47 around the pegmatites. In contrast, Stage IIIb, which was responsible for the
48 hydrothermal mobilization of Zr and REE, is manifested by fluorite and quartz veins,
49 zircon spherules, gadolinite-group minerals, gittinsite and ferriallanite-(Ce) and a
50 pervasive replacement of the granite by these minerals. The distribution of REE, Zr, Nb
51 and Ti was controlled by the competition between hydrothermal fluids and the stability of

primary REE-F-(CO₂) minerals [e.g., bastnäsite-(Ce) host to LREE], zirconosilicates (i.e., Na-zirconosilicates and zircon host to HREE and Zr), Nb-Ti-minerals (i.e., pyrochlore host to Nb, and narsarsukite host to Ti) and the stability of secondary LREE-silicates [i.e., ferriallanite-(Ce)], HREE-silicates [i.e., gadolinite-(Y)], zirconosilicates (i.e., gittinsite and zircon) and Nb-Ti-minerals (i.e., titanite and pyrochlore).

Lithogeochemical vectors were identified to distinguish between the high temperature acidic alteration (IIIa) using CaO/Na₂O (indicator of Ca-metasomatism) and Fe₂O₃/Na₂O ratios (indicator of aegirization/hematization), and the low temperature acidic alteration (IIIb) using the CaO/Al₂O₃ ratio (indicator of Ca-F-metasomatism). Bulk rock compositional data show that alteration was accompanied by an enrichment of HREO and ZrO₂ at the deposit scale, whereas the LREO were not selectively enriched. A 2-D geochemical model of the deposit indicates that the LREO are more dispersed, whereas HREO and ZrO₂ are selectively distributed. These variations in LREE/HREE are also reflected in the mineral chemistry, especially in hydrothermal zircon crystals showing an unusual LREE enrichment and HREE depletion, contrasting with pseudomorphs, which are enriched in HREE. Hydrothermal ferriallanite-(Ce) and gadolinite-group minerals also show a clear trend of REE depletion with Ca enrichment. Controlling factors for the hydrothermal mobilization of LREE, HREE and Zr were temperature, pH and the availability of fluoride ions (F⁻) in the fluid for the dissolution of zircon, and chloride ions (Cl⁻) for the complexation of the REE. The study of rare hydrothermal minerals in conjunction with field observations and the evaluation of variations in bulk rock composition, allowed us to develop a new model for the hydrothermal evolution stage of Strange Lake.

75 **Introduction**

76 Recent advances in high technology industries have created a large increase in demand
77 for the “critical” metals and a need to develop robust models of ore genesis to facilitate
78 their successful exploration. Peralkaline and alkaline igneous complexes are highly
79 enriched in some of these metals, including the REE (in particular the HREE) and other
80 high-field strength elements (HFSE), notably Zr, Ti and Nb. The high alkali and fluorine
81 content of the corresponding melts leads to depolymerization, a decrease in the solidus
82 temperature and a lowering of the viscosity of these melts, all of which combine to
83 facilitate incorporation of the above metals in these magmas (Manning, 1981; Linnen and
84 Keppler, 2002; Thomas et al., 2012; Bartels et al., 2013). Minerals that host the REE and
85 other HFSE in these deposits include fluorocarbonates [e.g., bastnäsite-(Ce) and parisite-
86 (Ce)], phosphates [e.g., xenotime-(Y) and monazite-(Ce)], silicates [e.g., allanite-(Ce)
87 and gadolinite-group minerals] and zirconosilicates (e.g., zircon, eudyalite, gittinsite).
88 Some intrusive complexes are sufficiently enriched in these elements to host potential
89 mineral resources for exploitation, such as the peralkaline granitic pluton at Strange Lake
90 (Salvi and Williams-Jones, 2006; Gysi and Williams-Jones, 2013) and the nepheline-
91 aegirine syenite at Nechalacho both in Canada. Even though these igneous complexes
92 are of magmatic origin, subsolidus re-equilibration and alteration make it difficult to
93 separate igneous processes of critical metal enrichment from those involving
94 hydrothermal fluids.

95 At Strange Lake, critical metal enrichment was initially attributed to igneous
96 fractionation (Miller, 1986, 1990; Boily and Williams-Jones, 1994). However, Salvi and
97 Williams-Jones (1990, 1996, 2006) subsequently provided evidence for significant
98 mobilization of the metals by hydrothermal fluids. These studies identified a high

temperature saline orthomagmatic fluid (~20-25 wt.% NaCl equivalent; homogenization temperatures Th of 300 to 360 °C) accompanied by an immiscible hydrocarbon-bearing fluid, and a low temperature Ca-bearing fluid (~10-25 wt.% NaCl equivalent; Th of 90 to 225 °C). Recently, Gysi and Williams-Jones (2013), have built on this work by using mineralogical observations and thermodynamic calculations to develop a quantitative model, in which fluid exsolution from the magma and acidic alteration, led to hydrothermal mobilization of the REE and other HFSE within and beyond the host pegmatites. Most recently, Vasyukova and Williams-Jones (2014, and 2016) have shown that separation of an immiscible fluoride melt from the silicate magma, and preferential concentration of the REE in the fluoride melt **also** may have played an important, previously unrecognized, role in the magmatic concentration of the REE. It is therefore becoming increasingly clear that the extraordinary concentration of critical metals at Strange Lake was due to a complex interplay of igneous and hydrothermal processes.

In this study, we focus on the hydrothermal stage of the evolution of the peralkaline granites and pegmatites and the associated metal mobilization. Our purpose was to determine: (1) the mineral assemblages related to the different alteration stages; (2) how the changes in bulk rock and mineral chemistry are related to the chemistry of the hydrothermal fluids, and (3) the scale and mechanism of REE, Zr and Nb mobilization and concentration. Using this information, we developed lithogeochemical vectors, which we believe will aid in the exploration for similar granite-hosted REE/HFSE ore deposits in anorogenic settings.

Geological setting and lithology

1
2
3
4 122 *The Strange Lake pluton*
5

6 123 Strange Lake is ~6 kilometer wide mid-Proterozoic (1240 Ma; Pillet et al., 1989; Miller
7
8
9 124 et al., 1997) peralkaline granitic pluton located in northeastern Canada along the border
10
11 125 between Quebec and Labrador. The pluton consists of anorogenic (A-type) granites
12
13 126 surrounded by a fluorite/hematite breccia, and is hosted in Aphebian gneiss and Elsonian
14
15 127 monzonite (Fig. 1A). The presence of roof pendants of gneiss and monzonite in the
16
17 128 Strange Lake granite and low trapping pressures estimated from orthomagmatic fluid
18
19 129 inclusions (Salvi and Williams-Jones, 1992) indicate a shallow level of emplacement.
20
21 130 Two different granite types have been recognized based on their feldspar mineralogy
22
23 131 (Nassif, 1993). In the central and southern part of the pluton, the rocks consist of
24
25 132 hypersolvus granite (perthitic K-feldspar). These rocks are surrounded by a later
26
27 133 subsolvus granite (two feldspars, albite and microcline), which is host to two pegmatite-
28
29 134 rich ore zones. This reverse zoning of the granites has been ascribed to feldspar
30
31 135 fractionation and fluid saturation during crystallization (Nassif, 1993). However, a
32
33 136 similar reverse zoning could result from a later batch of melt forcing its way to the
34
35 137 margins during multiphase intrusion cycles (Vigneresse, 2007). The latter hypothesis is
36
37 138 supported by field observations, which indicate that the first batch of melt was less
38
39 139 hydrous as evidenced by the occurrence of late interstitial amphibole, and the second
40
41 140 batch of melt was saturated with H₂O at an early stage of crystallization, with amphibole
42
43 141 occurring as early phenocrysts (Siegel and Williams-Jones, 2015). This indicates that
44
45 142 successive intrusions of variably evolved melts likely affected H₂O saturation, alkali
46
47 143 content and HFSE enrichment (i.e., REE, Zr, Nb and Ti).
48
49
50
51
52
53
54
55
56
57
58
59
60
61
62
63
64
65

Potential ore zones

Two potential ore zones have been recognized, the Main Zone located in the central part of the pluton and the B Zone located in the northwest (Fig. 1A). The B Zone, which is the target of current exploration, consists of a lens-shaped pegmatite spine hosted by subsolvus granite, and covers an area of ~400,000 m² (Fig. 1B). The pegmatites consist of a series of flat-lying sheets dipping gently to the northeast (Fig. 1C). The total indicated mineral resource is 278 Mt ore grading 0.93 wt.% total rare earth oxide (TREO), 1.92 wt.% ZrO₂ and 0.18 wt.% Nb₂O₅ (www.questrareminerals.com). The highest grades are within the pegmatite spine where there is an indicated resource of 20 Mt ore grading 1.44 wt.% TREO, 2.59 wt.% ZrO₂ and 0.34 wt.% Nb₂O₅. This zone also has the highest proportion of heavy (H)REO (50%, versus 39% for the entire deposit). A list of REE-, Nb- and Zr-bearing ore minerals and their occurrences is given in Table 1.

This study is based on a detailed sampling of four drill cores (Fig. 1B: BZ11176; BZ10027; BZ10078; BZ11109) across a NE-SW section of the pegmatite spine. Four additional samples containing hydrothermal veins were also considered (see the Supplementary Online Material Tables for a list of samples). The detailed geological map (Fig. 1B) and element distribution of the deposit (Fig. 2) are based on data made available by Quest Rare Minerals Ltd for over 23,000 drill core samples. As exemplified in Figure 2, the spatial distribution of LREO, HREO and ZrO₂ concentrations is related primarily to the distribution of the pegmatites, which contain the highest concentrations of these elements; concentrations are significant in the surrounding subsolvus granite but generally lower. Five domains displaying variable relative metal concentrations can be recognized (Fig. 2). Zone 1 (pegmatite spine) is highly enriched in LREO, HREO and

1
2
3
4 168 ZrO_2 , whereas zones 2 to 5 (granite) have highly variable relative LREO, HREO and
5
6 169 ZrO_2 concentrations. The overall enrichment of the REE and Zr in the granite (Zones 2 to
7
8
9 170 4) below the pegmatite sheets, and the presence of irregular patches in the granite that are
10
11 171 enriched/depleted in metals to depths of >150 m below them, suggests a post-magmatic
12
13 172 hydrothermal metal mobilization on a scale of hundreds of meters.
14
15
16
17
18

19 174 *Petrography*

20
21 175 The granite in the B Zone is pervasively altered to a depth of >150 m (Fig. 3). However,
22
23 176 the primary magmatic textures are relatively well preserved. Thus, it is possible to
24
25 177 observe amphibole cumulate layers up to 20 cm thick and ellipsoidal inclusions of fine-
26
27 178 grained granite with a diameter of ~5-10 cm. The least altered granite is porphyritic with
28
29 179 euhedral to subhedral arfvedsonite phenocrysts (~0.5-0.8 cm) or nearly equigranular with
30
31 180 smaller (<0.4 cm) arfvedsonite crystals. The matrix consists of fine-grained (<0.2 cm)
32
33 181 anhedral albite, K-feldspar and quartz (Fig. 3A). Zirconosilicate minerals can be observed
34
35 182 in hand samples with an estimated modal proportion ranging between 5 and 10 vol.% of
36
37 183 the rock. They commonly occur as rectangular pale yellow subhedral phenocrysts (0.5-1
38
39 184 cm) of vlasovite ($\text{Na}_2\text{ZrSi}_4\text{O}_{11}$) with poikilitic inclusions of feldspar and arfvedsonite.
40
41 185 White to pinkish gagarinite-(Y) $[\text{NaCa}(\text{Y,Ce})\text{F}_6]$ crystals occur interstitially and in
42
43 186 patches with a modal proportion of <5 vol.%. Fine-grained (50-100 μm) euhedral
44
45 187 pyrochlore $[(\text{Na,Ca})_2\text{Nb}_2\text{O}_6(\text{OH,F})]$, <1 vol. %, is only distinguishable in thin section.
46
47 188 Titanium-bearing minerals comprise dark brown rectangular primary narsarsukite
48
49 189 $[\text{Na}_2(\text{Ti,Fe}^{3+})\text{Si}_4\text{O}_{10}(\text{O,F})]$ phenocrysts (1-2 cm) and, more rarely, patches of radially
50
51 190 grown dark brown-orange astrophyllite crystals; these minerals comprise <5 vol.% of the
52
53
54
55
56
57
58
59
60
61
62
63
64
65

191 rock.

192 The pegmatites form sheets that range from a few centimeters up to 10 meters in

193 thickness that are mineralogically zoned into border and core zones (Fig. 4), hereafter

194 referred to as border and core pegmatite, respectively (Gysi and Williams-Jones, 2013).

195 Most of the pegmatite sheets are highly altered and primary features are rarely preserved.

196 The least altered border pegmatites, however, are similar in mineralogy to the granite,

197 whereas the core pegmatite consists of quartz, variable proportions of zircon and fluorite

198 and REE-F-(CO₂) minerals. Thin pegmatite dikes (~3 to 5 cm thick) are unzoned and

199 have a mineralogy similar to the border pegmatite, albeit with a higher modal proportion

200 of quartz. The border pegmatites contain large (>1 to 5 cm) to medium (~1 cm) size

201 subhedral K-feldspar crystals (between ~40 and 60 vol. %). Quartz forms subhedral to

202 interstitial crystals (>40 vol. %). Rarely preserved euhedral arfvedsonite crystals (2 to >3

203 cm in length) make up <10 vol.% of the rock. Large boat-shaped pseudomorphs (up to 3

204 cm in diameter), consisting of zircon/quartz or gittinsite/quartz (10-40 vol.%), occur

205 among the K-feldspar and quartz crystals. Previous studies of the Main Zone pegmatites

206 have determined that the pseudomorphs represent former elpidite (Na₂ZrSi₆O₁₅ · 3H₂O)

207 crystals (Salvi and Williams-Jones, 1995). Only pseudomorphs, (i.e., no relicts of

208 primary zirconosilicates), however, have been found in the B Zone. Pseudomorphs after

209 narsarsukite (now consisting of titanite and quartz; Salvi and Williams-Jones, 1995), of 1

210 to >3 cm in diameter, locally form cumulate-like textures (Fig. 4B). In addition to the

211 main rock-forming minerals, referred to above, there are large numbers of fine-grained

212 REE and HFSE minerals (Table 1), many of which are of hydrothermal origin, including

213 members of the gadolinite-group, which are accompanied by fluorite and quartz (Fig.

214 4E). Finer grained aplites form layers varying between ~20 and 30 cm in thickness
215 around some of the borders of the pegmatite sheets.

217 Analytical and sampling methods

218 Bulk rock samples were collected from drill cores following geological core logging.
219 Mineralized samples and pegmatites were marked out with a nominal length of 0.5 to 1.0
220 m, while the remaining core was usually sampled at 2 m interval lengths; each drill hole
221 was sampled from top to bottom. Sample intervals typically do not cross alteration
222 boundaries or lithological contacts where either of these features is sharp; where
223 gradational contacts occur, samples were divided so as to minimize the mixing of
224 lithological or alteration types. Bulk rock samples were analyzed by Actlabs Ltd. using
225 several techniques described in their Code-8 REE Assay + F, the Code-4 Litho-Quant
226 (11+) Major elements fusion and the Code-4E XRF for Nb protocols. The REE were
227 analyzed in fused lithium meta- and tetraborate pellets dissolved in dilute nitric acid
228 followed by inductively coupled plasma mass spectrometry (ICP-MS). Fluorine
229 concentrations were determined using a fluoride ion sensitive electrode and other major
230 elements were analyzed in digested samples using ICP optical emission spectrometry
231 (OES). Niobium was analyzed separately by X-ray fluorescence (XRF) in pressed
232 powder pellets.

233 Mineral compositions were determined in 30 µm-thick carbon-coated thin
234 sections using a JEOL JXA-8900L electron microprobe (EMP). The beam current was 30
235 nA and the acceleration voltage was 20 kV. The beam diameter was 1-5 µm for zircon
236 and 10 µm for ferriallanite-(Ce), gadolinite-group minerals, vlasovite, gittinsite,

pyrochlore and titanite. Counting times and standards employed in the analyses are given in Appendix Table A1, together with detection limits based on repeated analyses of standards. Backscattered electron photomicrographs (BSE) were taken using a 1 µm beam diameter and 20 nA acceleration voltage. Element X-ray maps were produced using wavelength dispersive spectrometers (WDS) with a beam current of 50 nA, an acceleration voltage of 20 kV and a dwell time of 60 ms. A list of all samples, and a compilation of bulk rock and mineral chemical data can be found in the Supplementary Online Material Tables.

Metasomatic Processes

The evolution of the Strange Lake B-Zone granites and pegmatites can be subdivided into three different stages related to different rock textures and mineral assemblages. These are: I) a magmatic stage, II) a near neutral hydrothermal stage (alkali metasomatism) and III) an acidic hydrothermal stage.

Alkali metasomatism

The alkali metasomatism comprises: i) Na-metasomatism with albitization of the granite in which primary K-feldspar was replaced by albite (Fig. 5A) and ii) K-metasomatism (potassic alteration) of the pegmatites in which albite lamellae were replaced by microcline (Fig. 5B). The albitization is interpreted to have been earlier than the potassic alteration because it occurred pervasively in the granite, even in the less altered subsolvus granite of the central part of the pluton, whereas the potassic alteration was restricted to the borders of the pegmatite sheets. The alteration of the K-feldspar can be described by

the reaction:



As is evident from the distribution of K and Na in the large crystal illustrated in Figures 5C and D, the replacement of albite by K-feldspar in the pegmatites proceeded with the development of large heterogeneous microcline crystals having highly variable domains with respect to their K/Na ratios.

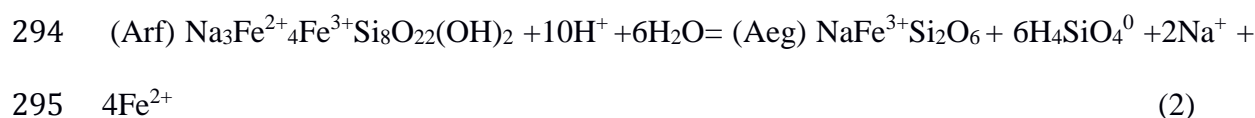
A possible explanation for the sodic metasomatism of the granite and the potassic metasomatism of the pegmatites is that the former occurred at higher temperature. This would be consistent with the observation that the equilibrium constant for Reaction 1 is given by the activity ratio of the cations (aK^+/aNa^+), and increases with increasing temperature. Thus, for a given K^+/Na^+ ratio in the fluid, the right hand side of Reaction (1) or formation of albite would be favored by higher temperature and the left hand side of this reaction or formation of K-feldspar by lower temperature. This does not rule out the possibility that the K/Na ratio of the fluid evolved to higher values in the pegmatites, thereby promoting potassic alteration of the latter.

Acidic alteration

The acidic alteration was part of the evolution of the pegmatites, as shown previously by Gysi and Williams-Jones (2013), and involved pegmatite-sourced low pH fluids that produced complex alteration assemblages, which varied with temperature and the extent to which the rock buffered pH. These fluids were responsible for the hydrothermal mobilization of REE/HFSE in the late stage development of the pegmatite spine and infiltrated the surrounding granites. The acidic alteration is characterized by the following

283 alteration textures/types: i) the pseudomorphic replacement of Na- by Ca-zirconosilicates
 284 (Ca-metasomatism), ii) aegirinization/hematization, iii) the formation of late stage quartz
 285 and fluorite veins (Ca-F-metasomatism), iv) phyllic alteration and v) brecciation. These
 286 alteration textures/types have been subdivided according to whether they occurred at high
 287 temperature (e.g., pseudomorphic replacement reactions), and low temperature (e.g.,
 288 quartz/fluorite vein formation).

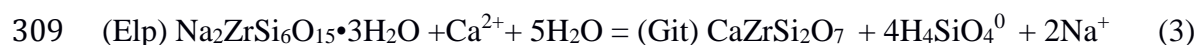
289 Aegirinization/hematization is manifested by the variable replacement of
 290 arfvedsonite by aegirine and/or hematite in both the granite and the pegmatites (Figs. 3
 291 and 4). The original igneous porphyritic textures are preserved in this alteration type,
 292 which is manifested by a distinctive alteration halo around the pegmatite spine. The
 293 reaction of arfvedsonite to aegirine leads to the release of Si, Na and Fe as follows:



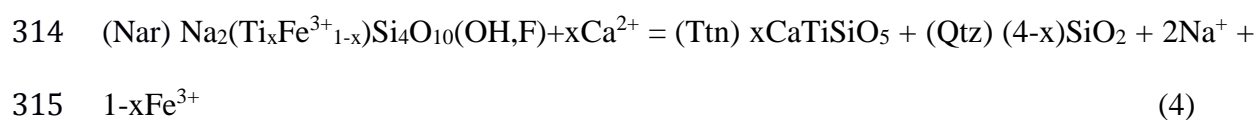
296 which leads to the formation of hydrothermal quartz and hematite (if oxidized) or
 297 magnetite. Three modes of occurrences of aegirinization/hematization have been
 298 distinguished in the granite, namely hematite replacement of arfvedsonite in crystal cores
 299 (Fig. 3B), pervasive replacement of arfvedsonite by aegirine (Fig. 3C) and replacement of
 300 arfvedsonite rims by aegirine ± hematite. Aegirinization is particularly intense around the
 301 pegmatite spine, suggesting that the pegmatites were the cause of alteration, and that
 302 acidic alteration and aegirinization/hematization are closely related. Hematization is more
 303 widespread than aegirinization, and also occurs pervasively in the granite (after aegirine
 304 and arfvedsonite) and as hematite veins.

305 Calcium-metasomatism is interpreted to have occurred pervasively along the

borders of the pegmatites and patchily in the granite, and is manifested by Ca-zirconosilicate (gittinsite and armstrongite) pseudomorphs, which formed after Na-zirconosilicates (i.e., vlasovite and elpidite) according to the reaction:



and Na-Ti-bearing minerals (narsarsukite) by titanite and quartz according to the reaction:



Reactions (3) and (4) indicate that quartz may form, depending on temperature and the activity of Na^+ .

Calcium-F-metasomatism is manifested by the assemblage ferriallanite-(Ce) \pm gittinsite \pm zircon \pm fluorite \pm quartz (Fig. 3D), and macroscopically in the granite by the white-purple color of the rock matrix. The presence of quartz/fluorite veins (Fig. 6), which crosscut aegirinized arfvedsonite and pseudomorphs (see further below), indicates that Ca-F-metasomatism postdated aegirinization/hematization and Ca-metasomatism. Moreover, whereas the latter two alteration types involved pervasive replacement and were restricted to the pegmatite spine, Ca-F-metasomatism extended well into the surrounding granite and involved the formation of veins and the filling of vugs by REE-Zr mineralization. Most of the veins are subvertical, ~0.5 to 2.5 cm thick, and can be subdivided into quartz-, quartz-fluorite-, fluorite- and hematite-types. They are

1
2
3
4 329 interpreted to represent one of the latest hydrothermal event that affected the B Zone.
5
6 330 Colloform fluorite layers in quartz-fluorite veins indicate a progressive growth of the
7
8 331 mineral from a low temperature hydrothermal fluid (Fig. 6C). The quartz-fluorite- and
9
10 332 quartz-veins are either barren or mineralized, with the latter containing ferriallanite-(Ce)
11
12 333 \pm titanite \pm gadolinite-group minerals \pm chlorite. A sample from a drill core to the NE of
13
14 334 the B Zone (Figs. 1, 6D) contains a contact between pegmatite/granite that is both micro-
15
16 335 brecciated and filled with fluorite. The formation of quartz/fluorite/hematite veins was
17
18 336 accompanied by the late formation of breccias and micro-breccias (Figs. 6D and E).

19
20
21 337 Acidic hydrothermal activity also gave rise to phyllic alteration textures with the
22
23 338 late stage replacement of primary silicate minerals (i.e., K-feldspar and arfvedsonite) by
24
25 339 K-, Fe- and Al- phyllosilicates. Phyllic alteration is generally restricted to the border
26
27 340 pegmatite where it is extensive, but also is observed locally in the adjacent granite,
28
29 341 commonly as phyllosilicate-filled micro-fractures in K-feldspar and arfvedsonite. The
30
31 342 phyllosilicates comprise Al varieties (compositions ranging between donbassite and
32
33 343 dickite-halloysite-kaolinite, and pyrophyllite), Fe-rich varieties (chamosite and
34
35 344 ferrosudoite) and K-bearing varieties (muscovite and ferroccladonite) (Gysi and
36
37 345 Williams-Jones, 2013). Excess cations for some analyzed crystals may indicate the
38
39 346 presence of Li as polyolithionite (Gysi and Williams-Jones, 2013).

40
41
42 347

43 348 **Mineral paragenesis**

44
45 349 The mineral paragenesis in the B Zone was reconstructed from textural relationships
46
47 350 involving the different minerals, using a combination of optical microscopy, scanning
48
49 351 electron microscopy and element maps prepared using the EMP. These are illustrated in

Figures 7–11. Minerals were interpreted as magmatic based on textural relationships, for example if they occur as phenocrysts (e.g., arfvedsonite) or as isolated relict crystals displaying dissolution/corrosion textures [e.g., bastnäsite-(Ce) and pyrochlore]. The latter was especially the case for minerals in the pegmatites where it is more difficult to distinguish between magmatic and hydrothermal minerals. Hydrothermal minerals were recognized on the basis of replacement and dissolution textures and their presence in veins and breccia cement.

Magmatic REE/HFSE minerals

The REE/HFSE minerals interpreted as magmatic are the Na-zirconosilicates, pyrochlore, the REE-F-CO₂-minerals [gagarinite-(Y), bastnäsite-(Ce) and fluocerite-(Ce)] and the Na-Ti-bearing minerals (Fig. 8). The dominant Na-zirconosilicate in the granite is vlasovite (Figs. 7A and 8A), which forms interstitial intergrowths with feldspar and quartz, and contains inclusions of euhedral albite and fragmented albitized K-feldspar and arfvedsonite. Vlasovite also displays evidence of post-magmatic exsolution of zircon+quartz and a patchy Ca-F metasomatic overprint by gittinsite and quartz or fluorite and zircon. The dominant zirconosilicate (elpidite) in the pegmatites is boat-shaped and is represented by pseudomorphs of either zircon and quartz or gittinsite and quartz (Fig. 8D). Gagarinite-(Y) formed interstitially to the primary silicate minerals, and is the dominant REE-F-mineral in the granite. In the cores of the pegmatites, bastnäsite-(Ce) and fluocerite-(Ce) relicts were replaced by hydrothermal fluorite and/or quartz. The occurrence of REE-F-CO₂-minerals that have been replaced in both the granites and pegmatites has therefore been interpreted to indicate a magmatic or late magmatic-

hydrothermal origin for these minerals (Gysi and Williams-Jones, 2013). The main
magmatic Ti- and Nb-bearing minerals are narsarsukite and pyrochlore, respectively. The
latter is also host to significant concentrations of LREE. Pyrochlore forms euhedral
crystals on the surface of K-feldspar or arfvedsonite, and occurs as aggregates in quartz.
The crystals must have been relatively resistant to corrosion during alteration as
pyrochlore relicts are found throughout the B Zone. Some of the pyrochlore may also be
of hydrothermal origin as its crystals occur as clusters in hydrothermal quartz.
Narsarsukite was identified by Birkett et al. (1996) in several localities in the pluton, but
only occurs as rectangular prismatic pseudomorphs replaced by titanite and quartz (Figs.
4B and 8F) in the B Zone. Other REE minerals that occur in pseudomorphs are cerite-
(Ce) $[\text{Ce}_9\text{Fe}(\text{SiO}_4)_6(\text{SiO}_3)(\text{OH})_4]$ in the granite and kainosite-(Y)
 $[\text{Ca}_2\text{Y}_2(\text{SiO}_3)_4(\text{CO}_3)\cdot\text{H}_2\text{O}]$ in the pegmatite. Relicts of these minerals, however, are rare
in the B Zone.

Hydrothermal REE/HFSE minerals

Secondary zirconosilicates and REE-bearing silicates occur as early alteration and late
stage vein assemblages in both the granite and the pegmatite sheets (Figs. 7 and 9). Based
on the common occurrence of hydrothermal minerals in the B Zone, we estimate that
>90% of primary REE- and Zr-minerals were replaced by hydrothermal equivalents.

The secondary LREE-bearing silicate is ferriallanite-(Ce), which occurs as
elongated crystal intergrowths that formed by replacement of albite and arfvedsonite
during chemical dissolution-precipitation reactions, or filled micro-fractures and pores in
the rock matrix. The micro-fractures occur in K-feldspar and arfvedsonite/aegirine, with

ferriallanite-(Ce) being accompanied by fluorite and quartz. These microtextures preserve evidence of dissolution of primary minerals but do not involve secondary phyllosilicates. The ferriallanite-(Ce) crystals are chemically zoned, as illustrated by backscattered electron images and element maps; La and Ce are concentrated in micro-domains, whereas the Nd distribution is more homogeneous (Fig. 10A). On a micron scale, Y is enriched in small domains. Ferriallanite-(Ce) also occurs in late stage quartz veins, as intergrowths with quartz and fluorite. (Fig. 9D and F)

The HREE-bearing silicates are dominantly gadolinite-group minerals that form concentrically zoned spherules. In the granite, these minerals occur interstitially as a replacement of feldspars and arfvedsonite, as pore fillings and as crystal aggregates in secondary quartz and quartz veins. By contrast, in the pegmatite sheets, they form dispersed crystal aggregates in late veins or are concentrated in strongly altered HREE layers (Fig. 4E). In the latter, the gadolinite-group minerals display a colloform growth texture that is characteristic of low temperature hydrothermal minerals (Fig. 10B). Significantly, the cores of the colloform domains are enriched in Gd and Dy, whereas the rims are enriched in the heavier Yb and Y, indicating that LREE and HREE partitioned differently between the hydrothermal fluid and the precipitating minerals.

The hydrothermal zirconosilicates are either zircon, gittinsite, or in few cases armstrongite. Several types of zircon crystals were observed in the pegmatites and granites. Gysi and Williams-Jones (2013) recognized two generations of euhedral zircon crystals in the pegmatites. Zircon I occurs as a pseudomorphic replacement of elpidite and zircon II occurs as hydrothermal crystal clusters intergrown with quartz and/or fluorite. Zircon II displays strong chemical zoning. In the granite, a third zircon type was

1
2
3
4 421 recognized. Zircon III forms spherules of radial aggregates intergrown with fluorite and
5
6 422 minor proportions of quartz. This type of zircon accompanied Ca-F-metasomatism, filled
7
8
9 423 pores and replaced primary silicate minerals in the granite. In a few samples, anhedral
10
11 424 zircons seemingly replaced vlasovite in the granite, and are interpreted to have formed by
12
13
14 425 a process similar to that of zircon I, which occurs in pseudomorphs in the pegmatites.
15
16 426 This interpretation is also consistent with the observed mineral chemistry (see below).
17
18
19 427 Early gittinsite and quartz occur as pseudomorphs after elpidite in the pegmatites,
20
21 428 whereas interstitial elongated feathery gittinsite crystals formed in pores with quartz or
22
23
24 429 replaced primary silicate minerals (in both the granite and pegmatites). Zircon **also** has
25
26 430 been observed in veinlet networks within a fluorite vein in a pegmatite sheet (Fig. 11).
27
28
29 431 Element maps show that one of the zircon veinlets cuts an assemblage of aegirine +
30
31 432 quartz in a pseudomorph after arfvedsonite, indicating that Zr was mobilized after
32
33
34 433 aegirinization (Fig. 11).

35
36 434 Hydrothermal titanite forms small euhedral crystals intergrown with quartz,
37
38 435 gadolinite-group minerals and/or ferriallanite-(Ce) in the granite and pegmatite sheets (it
39
40
41 436 also occurs as pseudomorphs after narsarsukite as discussed above). This type of titanite
42
43 437 filled pores and replaced primary silicate minerals. Late titanite occurs as euhedral
44
45
46 438 crystals in quartz veins together with either gadolinite-(Y) and/or ferriallanite-(Ce) (**Fig.**
47
48 439 **9E**).

440 441 *Interpretation of alteration events*

442 A mineral paragenesis tied to the different alteration types **and textural changes is**
443 **presented** in Figure 12. The **magmatic** crystallization of subsolvus granite and pegmatite

1
2
3
4 444 sheets (stage I) led to the concentration of the REE in REE-F-(CO₂)-minerals (Figs. 8B
5
6 445 and E), Zr in Na-zirconosilicates (Figs. 7A, 8A and D), Ti in Na-Ti-bearing minerals
7
8 446 (Fig. 8F) and Nb in pyrochlore (it also contains significant amounts of LREE). Initially,
9
10 447 alteration was dominated by alkali metasomatism (stage II) with the replacement of K-
11
12 448 feldspar by albite in the granite (Fig. 5A) and the replacement of albite by K-feldspar in
13
14 449 the border pegmatite (Fig. 5B).

15
16 450 Once the pegmatite border developed further, exsolution of fluids from the
17
18 451 pegmatites led to acidic alteration (stage III), which was important for element
19
20 452 mobilization and the formation of hydrothermal REE- and Zr- bearing minerals. As
21
22 453 discussed earlier, the acidic alteration comprised a high temperature substage (IIIa)
23
24 454 dominated by Ca-metasomatism and a low temperature substage (IIIb) dominated by Ca-
25
26 455 F-metasomatism (IIIb).

27
28 456 Stage IIIa was characterized by the pseudomorphic replacement of magmatic
29
30 457 minerals (i.e., Ca-metasomatism of zirconosilicates and titanosilicates and the
31
32 458 aegirinization/hematization of arfvedsonite) and crystallization of Ca-bearing REE
33
34 459 minerals such as ferriallanite-(Ce) and gadolinite-group minerals. Restriction of
35
36 460 aegirinization/hematization to a halo around the pegmatite spine is interpreted to indicate
37
38 461 that the acidic fluids responsible for Ca-pseudomorphic replacement of primary zircon-
39
40 462 and titano-silicates were neutralized on coming in contact with the granite.

41
42 463 Stage IIIb involved the formation of quartz/fluorite veins in the granite, followed by
43
44 464 phyllic alteration in the border pegmatites and finally brecciation. Mobilization of the
45
46 465 REE and other HFSE (Zr, Nb and Ti) during this stage is evident in the pegmatite sheets
47
48 466 and granite where dissolution/precipitation and open-space filling textures are common
49
50
51
52
53
54
55
56
57
58
59
60
61
62
63
64
65

(Figs. 7B-D, 9A-C, 10A-B and 11). The presence of abundant fluorite accompanying zircon in veins cutting aegirine+quartz in a pseudomorph after arfvedsonite (Fig. 11) is strong evidence that Ca-F-metasomatism (substage IIIb) overprinted aegirinization/hematization (substage IIIa). Late stage hydrothermal quartz and fluorite veins containing Ca-bearing REE, Zr and Ti minerals, further indicate that Ca-F-metasomatism continued until the termination of hydrothermal activity. The alteration of amphibole and aegirine led to a continuous Fe supply for hematization until late stage brecciation. The source of F that led to Ca-F-metasomatism was undoubtedly the pegmatitic magma, whereas the source of Ca in the system is more difficult to explain as peralkaline magmas are relatively depleted in Ca (see discussion section).

477

478 Bulk rock and mineral chemistry

479 Bulk rock compositions

480 A comparison of the bulk rock compositions of the four drill cores along the NE-SW
481 profile of the B Zone shows that the highest concentrations of REE (LREO and HREO),
482 Zr and Nb occur in domains dominated by pegmatites (Fig. 13). The background
483 concentrations are close to those of the indicated mineral resource, with the granites
484 having concentrations of 0.55 wt.% LREO, 0.33 wt.% HREO, 1.87 wt.% ZrO₂ and 0.16
485 wt.% Nb₂O₅, and the pegmatites having concentrations of 0.72 wt.% LREO, 0.72 wt.%
486 HREO, 2.59 wt.% ZrO₂ and 0.34 wt.% Nb₂O₅ (<http://www.questrareminerals.com>).
487 Concentrations of ZrO₂ vary considerably in the granite but generally increase towards
488 the pegmatite-rich domains at the top of BZ10027 and BZ11176, and the center of
489 BZ10078 and BZ11109 (see also Fig. 2C). In the case of the LREO and HREO, there are

a few spikes of increased concentration in the granite, most of which can be related to the presence of hydrothermal ferriallanite-(Ce) and the gadolinite-group minerals, as discussed earlier. The overall distribution of the REE and HFSE suggests that ore metal concentrations were controlled primarily by the location of the pegmatites. However, the detailed mineralogical observations reported above, indicate that most of the REE- and Zr-bearing minerals are of hydrothermal origin. Therefore, hydrothermal mobilization and concentration processes may explain the large variations in ZrO₂ and the spikes for REE, which are observed in both the granites and the pegmatites. Furthermore, the REE profiles indicate that some pegmatites and granites may have been enriched by factors of 2-3 over distances of less than 10 m by this process.

500

501 *Compositions of allanite group minerals (LREE)*

The general mineral formula of epidote-group minerals is A₂M₃Si₃O₁₂(OH,F), with the A-site containing Ca²⁺ and the M-site Al³⁺ and Fe³⁺ in the epidote subgroup (Ca₂Al₂Fe³⁺Si₃O₁₂(OH)), and with the A-site containing Ca²⁺ and REE³⁺ and the M-site Al³⁺ and Fe²⁺ in the allanite subgroup (CaREEAl₂Fe²⁺Si₃O₁₂(OH)). The main control on the chemistry of these subgroups is a heterovalent coupled substitution of the type [REE³⁺+Fe²⁺]=[Ca²⁺+Fe³⁺]₋₁. There is also a homovalent substitution of the type [Fe³⁺]=[Al³⁺]₋₁ between ferriallanite-allanite and ferriepidote-epidote. As shown in Figure 14A adopted from Petrák et al., (1995) and Poitrasson (2002), these coupled substitutions can be depicted on an Al vs. REE diagram and Fe³⁺/Fe²⁺ ratios can be estimated using the equation:

$$512 \quad \text{Fe}^{3+}/(\text{Fe}^{3+}+\text{Fe}^{2+})=(\text{REE}^{3+}/\text{Al}^{3+})+1 \quad (5)$$

513 Structural formulae were calculated based on 3 Si due to possible vacancies on the
 514 A-site and a charge deficit from our EMP data (Armbruster et al., 2006). The A-site
 515 generally has >0.5 apfu REE, and the M-site >0.5 apfu Fe³⁺, classifying the mineral in the
 516 allanite-subgroup, with the “ferri” in ferriallanite-(Ce) indicating that the Fe³⁺-rich
 517 variety is dominant. Compositional data for hydrothermal ferriallanite-(Ce) are listed in
 518 Table 2 for granites, pegmatites and quartz/fluorite veins, and have been further
 519 subdivided, based on textural relationships, into phases occurring as mineral
 520 replacements, as pore fillings (Fig. 9A), in micro-fractures (Fig. 9B), and as veins (Figs.
 521 9D and F). The ferriallanite-(Ce) in hydrothermal veins and micro-fractured rocks
 522 generally has higher Al³⁺, REE³⁺ and lower Fe³⁺ contents than ferriallanite-(Ce) from the
 523 mineral replacement and pore space filling stage (Fig. 14A). The overall result is a mixed
 524 ferriallanite-ferriepidote-epidote composition, in which the REE concentration increases
 525 with decreasing Ca concentration (Fig. 14B). We therefore consider that the ferriallanite-
 526 (Ce) composition can be used to relate stages of Ca-metasomatism to the redox condition
 527 (Fe³⁺/Fe²⁺), and the Al and REE concentrations of the hydrothermal fluid. As shown in
 528 Figure 14C, the data plot on a linear trend of Ca vs. Fe³⁺/(Fe³⁺+Fe²⁺), with ferriallanite-
 529 (Ce) from micro-fractures and late stage veins departing from the general trend towards
 530 lower Fe³⁺/Fe³⁺+Fe²⁺ ratios with decreasing Ca concentration. For comparison, we have
 531 added data for epidote-group minerals from the Corupá pluton in Brazil (Vlach, 2012) to
 532 Figure 14. These are for hydrothermal ferriallanite-(Ce) and epidote from a peralkaline
 533 granitic pluton similar to Strange Lake. Our data for Strange Lake plot within the trends
 534 observed for the Corupá pluton, with deviations related to ferriallanite-(Ce) in fractures
 535 and veins. On a Ca vs. total REE diagram (not shown here), both datasets yield the same

linear trend representing a substitution range of up to 1 apfu REE for Ca, indicating a near perfect substitution of the REE for Ca without other elements being involved, except Fe for the coupled substitution with Al.

539

540 *Compositions of gadolinite-group minerals (HREE)*

541 The general formula for the gadolinite-group minerals is $A_2Z_2XS_i_2O_8(O,OH,F)_2$, with the
542 A-site being filled with Y [e.g., gadolinite-(Y) and hingganite-(Y)] or Ce [e.g.,
543 gadolinite-(Ce) and hingganite-(Ce)] and other lanthanides, Z being filled with Be, and X
544 filled with Fe^{2+} (gadolinite end member), Ca^{2+} (minasgeraisite end member) or being
545 vacant (hingganite end member) (DeMartin et al., 2001). Gerenite-(Y) was first described
546 from Strange Lake as a new gadolinite-group mineral, containing significant proportions
547 of Ca and Na with the general formula $(Ca,Na)_2(Y,REE)_3Si_6O_{18} \cdot 2H_2O$ (Jambor et al.,
548 1998). Chemical analyses of the gadolinite-group minerals are given in Table 3. A
549 ternary plot showing the different end members and analyzed gadolinite-group minerals
550 occurring in the granite and pegmatites of the B Zone, indicates that these minerals have
551 compositions ranging among gadolinite, hingganite, gerenite and a not yet IMA approved
552 mineral, “calciogadolinite” ($CaYBe_2FeSi_2O_8O_2$) (Fig. 15A). The data indicate a possible
553 solid solution with a general trend of Ca-REE substitution (Fig. 15C) similar to that
554 observed for ferriallanite-(Ce). This suggests strongly that a major change in fluid
555 chemistry occurred during the hydrothermal evolution of the system, particularly as
556 epidote group minerals display evidence of a similar substitution mechanism. The
557 chondrite-normalized REE profiles observed for gadolinite-group minerals in the granite
558 and pegmatites can be subdivided into LREE-, MREE- and HREE-enriched varieties

(Fig. 16). The gadolinite-group minerals in the pegmatite are more enriched in LREE, MREE and HREE compared to those in the granite; the HREE-enriched variety is restricted to the pegmatites. We interpret the observed variations in REE chemistry of gadolinite-group minerals to partly reflect the sources of HREE, MREE and LREE during alteration (i.e., pegmatite enriched in HREE and granite with variable distributions of HREE, MREE and LREE). In part, the variations also reflect the evolution of the chemical composition of the hydrothermal fluids during cooling and the timing of mineral saturation. The latter is evident in the growth textures of colloform and zoned gadolinite-group minerals (i.e., rims enriched in HREE and cores enriched in MREE; Fig. 10B). Comparison of our REE profiles with those for gadolinite-group minerals observed in pegmatites from other localities (Fig. 16C) allows us to classify our LREE-enriched variety as being between hingganite-(Ce) and gadolinite-(Ce), the MREE-rich variety as being between gadolinite-(Y)/hingganite-Y) and the HREE-rich variety as gerenite-(Y). This indicates several possible complex solid solutions of the gadolinite-group minerals at Strange Lake.

Compositions of Zr-bearing minerals

The average compositions of the zirconosilicate minerals (gittinsite, armstrongite, vlasovite and zircon) are reported in Tables 4 and 5 and illustrated in Figure 17. The composition of the Na-zirconosilicates in the granite plots close to that of the vlasovite endmember (Fig. 17A). Gittinsite has a Ca concentration that correlates negatively with those of the REE (not shown here), as is the case for ferriallanite-(Ce) and the gadolinite-group minerals. In contrast, zircon shows a systematic increase in HREE concentration

1
2
3
4 582 with F concentration in the pegmatites, but in the granites the HREE concentration varies
5
6 583 independently of F concentration (Fig. 17C). The opposite is observed for Ca
7
8 584 concentration, which correlates positively with HREE concentration in the granites but
9
10 585 not in the pegmatites (Fig. 17D). This separation of Ca and F trends suggests that the
11
12 586 source of Ca in the granites during growth of the hydrothermal zircon spherules was
13
14 587 different from that of F during growth of the zircon crystals in the pegmatites.
15
16
17
18

19 588 Zircon displays two distinctly different types of chondrite-normalized REE profile,
20
21 589 one that is strongly enriched in the HREE and depleted in the LREE (especially in zircon
22
23 590 I), and another that is relatively flat (Fig. 18). This is true for both the zircon spherules in
24
25 591 the granite and the zircon euhedra in the pegmatites. Profiles with intermediate slopes
26
27 592 (i.e., HREE-depleted profiles in the pegmatites and LREE-enriched profiles in the
28
29 593 granite) are also observed. In principle, the HREE should be preferentially incorporated
30
31 594 in the zircon crystal structure because their ionic radii are closer to that of Zr^{4+} than those
32
33 595 of the LREE. The flat and intermediate REE profiles are therefore very unusual. The
34
35 596 steep HREE-enriched profiles in euhedral zircon crystals, correspond to pseudomorphs
36
37 597 after elpidite in the pegmatites and to zircon relicts (after vlasovite) in the granite. Both of
38
39 598 these zircon generations therefore formed early in the overall hydrothermal evolution of
40
41 599 the system (zircon I). In contrast, zircon spherules in the granite (zircon III) usually show
42
43 600 a flat REE profile, with the zircon rims enriched in LREE compared to their cores. In the
44
45 601 pegmatites, some euhedral zircon crystals occurring as clusters in hydrothermal quartz
46
47 602 and fluorite (zircon II), display a flat REE profile similar to that of the zircon spherules
48
49 603 (zircon III), but the core and rim compositions have no distinguishable LREE zoning.
50
51 604 These unusual REE variations may be interpreted to reflect the alteration of zircon during
52
53
54
55
56
57
58
59
60
61
62
63
64
65

fluid-mineral interaction and the crystallization of hydrothermal zircon from a fluid with variable LREE/HREE ratios. To distinguish and understand the origin for each of these variations, the zircon chemistry needs to be considered in the context of the associated alteration stage and the behavior of the REE in hydrothermal fluids as a function of temperature and fluid composition (see discussion section).

610

Compositions of Nb- and Ti-bearing minerals

The average chemical compositions of titanite and pyrochlore are reported in Tables 6 and 7. Titanite shows clear trends of increasing Ti concentration with decreasing concentrations of Fe and F; titanite in the hydrothermal veins is enriched in Ti (and depleted in Fe and F) compared to titanite in the pegmatites (Fig. 19A and B). Pyrochlore shows a negative correlation of Ca concentration with REE concentration and a positive correlation between Na and F (Fig. 19C and D). The same correlation of Ca with REE is observed with ferriallanite-(Ce) and the gadolinite-group minerals, possibly indicating the occurrence of pyrochlore with a hydrothermal signature; the highest REE concentrations are in pyrochlore from the granite. The chondrite-normalized REE profiles (not shown) are LREE-enriched for pyrochlore, as is the case for the other LREE-silicates in the deposit. This mineral may also represent an important source for the LREE during alteration.

624

Lithogeochemical vectors of hydrothermal alteration

Introduction

The first step in identifying lithogeochemical vectors is to relate geochemical changes at

the mineral, rock and deposit scale to changes in specific processes leading to element mobilization/mineralization. In the case of hydrothermal-magmatic systems, for which the alteration types and their relations to mineralization are not well known, this requires: a) separation of magmatic from hydrothermal processes based on reaction textures; b) classification of alteration types and delineation of temporal relationships; c) documentation of the mineral chemistry and changes in this chemistry with alteration stages and mineralization in the deposit; d) thermodynamic modeling of fluid-rock interaction to determine element mobility as a function of physico-chemical parameters of the fluids (e.g. pH, temperature, ligand activity); e) identifying key alteration reactions by linking mineral textures, mineral chemistry and thermodynamic modeling of fluid-mineral equilibria; f) recognizing bulk rock element ratios based on e) and separating these data by trends; g) relating the trends in f) to alteration stage and element mobilization; h) establishing the spatial geochemical manifestation of alteration at the deposit scale based on f) and g).

High and low temperature acidic alteration vectors

Using the bulk rock chemical data, we have identified several lithogeochemical vectors that permit us to distinguish among the different alteration types. These vectors are predicted by the chemical reactions that explain the mineralogical textures produced by the different types of hydrothermal alteration (Table 8). Changes in the $\text{Fe}_2\text{O}_3/\text{Na}_2\text{O}$ ratio are due to aegirinization/hematization, whereas changes in the $\text{CaO}/\text{Na}_2\text{O}$ ratio reflect the pseudomorphic replacement of zirconosilicates (Ca-metasomatism) during high temperature acidic alteration (IIIa). The $\text{CaO}/\text{Na}_2\text{O}$ ratio also reflects the formation of

1
2
3
4 651 zircon, fluorite and quartz after aegirine in the granite during low temperature acidic
5
6 652 alteration (IIIb, Ca-F metasomatism). An independent signature of Ca-F metasomatism,
7
8
9 653 is provided by changes in the $\text{CaO}/\text{K}_2\text{O}$ and $\text{CaO}/\text{Al}_2\text{O}_3$ ratios, due to the formation of
10
11 654 gittinsite and quartz after K-feldspar. The formation of zircon+fluorite+quartz
12
13
14 655 (replacement of aegirine) and quartz+gittinsite (replacement of K-feldspar) was common
15
16 656 in the granite (Fig. 7B), and is satisfactorily explained by replacement reactions related to
17
18
19 657 Ca-F-metasomatism (Table 8). If Al is available for complexation with F in the fluid
20
21 658 (alteration of K-feldspar), fluorite will not form but gittinsite and quartz will be stable,
22
23
24 659 whereas if Al is not available (alteration of aegirine), fluorite will form and zircon will be
25
26 660 stable instead of gittinsite. We emphasize this finding here, as it indicates the importance
27
28
29 661 of the availability of Al for the mobilization of Zr in F-rich crustal fluids.
30

31 662 In order to distinguish the different alteration types based on bulk rock chemistry, it
32
33 663 was essential to first filter out the magmatic signature. To do so, we compared the data
34
35
36 664 for the least altered granite in the B Zone with the data for the altered granites and
37
38 665 pegmatites (Fig. 20). Outliers were eliminated and the data points for pegmatites and
39
40
41 666 strongly altered granite were subdivided based on the distribution of $\text{Fe}_2\text{O}_3/\text{Na}_2\text{O}$ and
42
43 667 $\text{CaO}/\text{Al}_2\text{O}_3$ values. Classification of the data based on these parameters is also supported
44
45
46 668 by other lithogeochemical parameters such as $\text{CaO}/\text{Na}_2\text{O}$. The data indicate that, with
47
48 669 increasing intensity of alteration, the $\text{Fe}_2\text{O}_3/\text{Na}_2\text{O}$ ratio increases systematically for
49
50
51 670 aegirized/hematized samples, which are mainly from border pegmatites, whereas the
52
53 671 $\text{CaO}/\text{Al}_2\text{O}_3$ ratio increases systematically for samples of core pegmatites and granites
54
55 672 subjected to Ca-F-metasomatism. From a plot of $\text{Fe}_2\text{O}_3/\text{Na}_2\text{O}$ vs. $\text{CaO}/\text{Na}_2\text{O}$ (Fig. 20B), it
56
57
58 673 is evident that the aegirized/hematized samples follow a trend that may be related to
59
60
61
62
63
64
65

1
2
3
4 674 either Ca-metasomatism (IIIa, high temperature pseudomorphs) or late stage Ca-F-
5
6 675 metasomatism (IIIb, low temperature alteration of aegirine to zircon+fluorite+quartz).
7
8
9 676 This ambiguity can be resolved, however, with a plot of $\text{CaO}/\text{Al}_2\text{O}_3$ vs. $\text{CaO}/\text{Na}_2\text{O}$ (Fig.
10
11 677 20C), from which it can be seen that aegirized/hematized samples follow the high
12
13 678 temperature acidic alteration trend related to Ca-metasomatism. This is consistent with
14
15
16 679 the observation that late stage fluorite and zircon veinlets crosscut aegirized
17
18
19 680 arfvedsonite (Fig. 11), and that Ca-F-metasomatism occurred later.

20
21 681 Density plots for LREO, HREO and ZrO_2 using $\text{CaO}/\text{Al}_2\text{O}_3$ as a vector for
22
23 682 separating the high temperature acidic alteration (IIIa) from the low temperature acidic
24
25 683 alteration (IIIb) show that, overall, the LREO concentrations were relatively constant
26
27
28 684 during acidic alteration (i.e., both high and low temperature acidic alteration) with some
29
30
31 685 samples depleted and others enriched. In contrast, HREO and ZrO_2 display clear trends of
32
33 686 enrichment with increased Ca-F-metasomatism. Samples subjected to high temperature
34
35 687 acidic alteration (IIIa) also display a significant enrichment in ZrO_2 , which is similar to
36
37 688 that for samples subjected to strong Ca-F-metasomatism (high $\text{CaO}/\text{Al}_2\text{O}_3$ ratio). The
38
39
40 689 observed trends can be explained by the fact that the pegmatite sheets are zoned into a
41
42 690 border enriched in a granitic component (K-feldspar +quartz +arfvedsonite \pm aegirine
43
44 691 \pm zirconosilicates \pm Ti-bearing minerals) and a core enriched in hydrothermal quartz,
45
46
47 692 fluorite and LREE minerals such as REE fluorocarbonates (Gysi and Williams-Jones,
48
49 693 2013). Owing to this zonation, border pegmatites are enriched in Zr, HREE, Al, Fe, K
50
51
52 694 and Si, and core pegmatites are enriched in LREE and F. Aegirized/hematized samples
53
54 695 of the border zone therefore should record the mobility of Zr and HREE. The Ca-F-
55
56
57 696 metasomatic samples should likewise record the remobilization of Ca, F and LREE in

core pegmatite. The reason for the more homogeneous distribution of LREE may be the higher mobility of LREE during the early higher temperature alteration stages (Gysi and Williams-Jones, 2013), whereas the mobility of Zr and HREE was “activated” only during the later stages of alteration. The distinct enrichment of ZrO_2 and a less distinct enrichment of HREO of samples subject to high T alteration (IIIa) suggest that, whereas Zr was enriched during alteration of the border pegmatite, the HREE were more mobile and thus more dispersed. In addition, the observation that Ca-F-metasomatism was able to enrich the rocks considerably, in both Zr and HREE, may indicate a high mobility of Zr and HREE at low temperature. In order to understand the factors controlling this element partitioning, it is necessary to determine the behavior of the LREE, HREE and Zr in the hydrothermal fluids. This was done using available thermodynamic models of fluid-mineral equilibria.

709

710 Discussion

711 *Mechanisms of hydrothermal REE and Zr mobilization*

712 The controlling factors for the mobilization of the LREE relative to the HREE and Zr are
713 temperature and fluid composition. This is best illustrated using available mineral
714 stability data. Previous numerical modeling of hydrothermal processes in the pegmatites
715 (Gysi and Williams-Jones, 2013), showed that the key to the observed REE mobilization
716 was the formation of chloride complexes (REECl^{2+} , REECl_2^+), whereas the mobility of
717 Zr depended on the formation of hydroxyfluoride complexes such as $\text{ZrF}(\text{OH})_3^0$ and
718 $\text{ZrF}_2(\text{OH})_2^0$; for further information on the speciation of these metals refer to Migdisov et
719 al. (2009, 2011). This modeling emphasized the role of pH, which depends on the initial

1
2
3
4 720 acid supply (i.e., the concentrations of HCl and HF), temperature (decreasing temperature
5
6 721 increases the dissociation of acids and thus the supply of H⁺) and the degree of fluid-rock
7
8
9 722 interaction. Changing temperature also affects metal mobility by promoting dissolution of
10
11 723 minerals. For many minerals, including REE minerals like bastnäsite-(Ce), solubility
12
13
14 724 increases with increasing temperature (prograde solubility), whereas some minerals, e.g.,
15
16 725 zircon, undergo retrograde solubility, i.e., their solubility increases with decreasing
17
18
19 726 temperature (Migdisov et al., 2011; Gysi and Williams-Jones, 2015). In addition,
20
21 727 temperature affects the relative mobility of the LREE and HREE, with the former being
22
23
24 728 more mobile at high temperature and the latter at low temperature (Gysi and Williams-
25
26 729 Jones, 2013). This is due to the increased stability of LREE chloride complexes with
27
28
29 730 increasing temperature (Migdisov et al., 2009).

30
31 731 In principle, it should be possible to transport the REE as fluoride complexes in
32
33 732 hydrothermal solutions with elevated fluorine concentration because of the very high
34
35
36 733 stability of REE-fluoride species (Migdisov et al., 2009). Recent numerical simulations
37
38 734 (Migdisov and Williams-Jones, 2014; Williams-Jones et al., 2012), however, have shown
39
40
41 735 that the REE are unlikely to be transported as REE fluoride complexes (e.g., REEF²⁺) due
42
43 736 to the association of H⁺ and F⁻ to form HF at mildly acidic conditions. Furthermore, the
44
45
46 737 low solubility of REE fluoride minerals (i.e., REEF₃ - fluocerite) at the mildly acidic to
47
48 738 neutral pH values, for which F⁻ would be available for complexation, inhibits the
49
50
51 739 formation of REE fluoride complexes. Hydrothermal fluids with elevated fluorine
52
53 740 concentrations, by contrast, should be capable of transporting significant Zr as
54
55 741 hydroxyfluoride complexes provided either that pH is high enough to release F⁻ ions
56
57
58 742 bound in HF, or the concentration of F is high enough that at low pH, sufficient numbers

1
2
3
4 743 of F⁻ ions not bound to HF are available for complexation. The availability of F⁻ ions also
5
6 744 can be limited by the release of cations, such as Al³⁺, during alteration of minerals like
7
8
9 745 feldspar, which may lead to the formation of complexes like AlF₂⁺. On the other hand, as
10
11 746 shown by Gysi and Williams-Jones (2013), AlF₂⁺ will breakdown in the presence of very
12
13
14 747 acidic fluids, releasing F⁻ in concentrations sufficient to promote Zr solubility as
15
16 748 hydroxyfluoride complexes at very low pH.

17
18
19 749 The paucity of thermodynamic data for REE minerals and to a lesser extent REE
20
21 750 aqueous species is an important limitation on our ability to reliably evaluate the mobility
22
23
24 751 of the REE and associated metals. Recent experiments designed to determine the
25
26 752 thermodynamic properties of the REE fluorocarbonates and HREE phosphates (Gysi and
27
28 753 Williams-Jones, 2015; Gysi et al., 2015) represent important steps to alleviate this
29
30
31 754 problem. Unfortunately, however, as discussed earlier, LREE mobility at Strange Lake
32
33 755 was largely controlled by the stability of ferriallanite-(Ce), for which there are no
34
35
36 756 thermodynamic data. The same problem applies in evaluating HREE mobility, which, as
37
38 757 also discussed earlier, was controlled by gadolinite-group minerals, for which there are
39
40
41 758 no thermodynamic data, and zircon for which partitioning of the HREE into
42
43 759 hydrothermal fluids is very poorly constrained.

44
45 760 Considering the thermodynamic models and the observed lithogeochemical vectors
46
47
48 761 described above, the more homogeneous distribution of the LREO during alteration may
49
50
51 762 be due to the higher mobility of the LREE compared to Zr and HREE in hydrothermal
52
53 763 fluids; LREE complexes would have been more stable than HREE complexes in the early
54
55 764 chloride-rich fluids known to have circulated in the Strange-Lake pluton (see
56
57
58 765 introduction). The HREE mobility (and that of Zr) was controlled by the solubility of

zircon, which is promoted by low temperature and pH, and high F concentration, conditions that likely prevailed during the Ca-F-metasomatic alteration stage. The precipitation of gadolinite-group minerals also must have occurred at low temperature, as displayed by their colloform textures (Fig. 10B), and therefore controlled the mobility of HREE in pegmatites, granites and veins. The same applies to zircon veinlets, zircon spherules and gittinsite, which display low temperature alteration textures (Figs. 9 and 11) and controlled the precipitation of Zr after aegirinization. Once this hydrothermal fluid reacted with feldspar, the release of Al^{3+} led to destabilization of Zr hydroxyfluoride species due to the formation of Al fluoride species, which may have enhanced precipitation of the hydrothermal zircon spherules in the granite. The fluid must have had either a very low pH, as indicated by the absence of phyllosilicates related to the alteration of feldspar in the granite (Figs. 9A and B), or was strongly undersaturated with respect to Al (due to complexation of Al with F). The LREE mobility was controlled by the solubility of bastnäsite-(Ce) and fluocerite-(Ce) and the precipitation of ferriallanite-(Ce), with the latter occurring in the granites, pegmatites and hydrothermal veins. This is consistent with the pervasive LREE mobilization on the deposit scale and the observed relatively constant LREE concentrations during Ca-F-metasomatism (Fig. 20D). Previous thermodynamic modeling of the B Zone, suggests that REE chloride complexes played an important role in the mobilization of the REE, and that this mobilization must have commenced at relatively higher temperature (Gysi and Williams-Jones, 2013).

The Links between zircon REE chemistry and fluid evolution during acidic alteration

The different chondrite-normalized REE profiles for zircon correspond to the different

acidic alteration stages (Fig. 21). During high temperature acidic alteration (Fig. 21a),
euhedral zircon formed as pseudomorphs after elpidite (Ca-metasomatism) in the
pegmatite borders and replaced vlasovite in the granite (zircon I). This early zircon is
characterized by steep HREE enriched profiles, and evolved in a nearly closed system
without much disturbance by the hydrothermal fluid, except for an internal Na-Ca
exchange in the pegmatites, for which the source of Ca was likely the fluorite in the core
pegmatites. Continued cooling and exsolution of fluids from the pegmatite cores led to
the formation of zones of increased fluid-rock reaction (Fig. 21b). Acidic hydrothermal
activity initiated in these zones and mobilized LREE during alteration of LREE-bearing
minerals (i.e., pyrochlore, bastnäsite-(Ce) and fluocerite-(Ce)). This stage is marked by
euhedral zircon crystals (zircon II) with REE profiles that are either similar to those
observed for zircon in the pseudomorphs (i.e., steep, HREE enriched) or LREE enriched
and HREE depleted (i.e., flat REE profiles). The latter profiles, likely reflect the
beginning of open-system behavior and interaction with a fluid having a high
LREE/HREE ratio at high temperature. During the low temperature acidic alteration (Fig.
21c), the pegmatite system opened with the formation of veins and more intense acidic
alteration by a much cooler fluid. This low temperature stage was favorable for the
transport of Zr and HREE. This led to leaching of Zr, HREE and LREE in the pegmatites,
interaction of the acidic F-bearing metal-enriched fluid with the surrounding granite,
mixing with a Ca-bearing fluid (see further below), and precipitation of zircon spherules
(zircon III) with flat chondrite-normalized REE profiles. The zircon III spherules and
their flat REE profiles is one of the signatures of the Ca-F-metasomatic event.

811

1
2
3
4 812 *The source of Ca and its role in Zr/REE mobility*
5

6 813 In many peralkaline and alkaline igneous systems, there is evidence that interaction of
7
8 814 fluids from the parent pluton with the surrounding rock units (e.g., carbonates) or mixing
9
10 815 of these fluids with externally derived meteoric waters added Ca to the system and led to
11
12 816 a corresponding decrease of metal mobility. For example, in the Tamazeght complex,
13
14 817 Morocco, pegmatites are interpreted to have contained H₂O-HF-rich fluids, which
15
16 818 transported Zr and interacted with the surrounding limestones, leading to deposition of
17
18 819 HFSE (Salvi et al., 2000). In the case of Anjanabonoina, Madagascar, it was proposed
19
20 820 that fluids released from the pegmatites circulated through the country rock, interacted
21
22 821 with plagioclase to release Ca and cycled back through the pegmatite body (Martin and
23
24 822 De Vito, 2014). For Strange Lake, it was initially proposed, based on studies of fluid
25
26 823 inclusions, that high salinity NaCl-rich (~20-25 wt.% NaCl) orthomagmatic fluids
27
28 824 exsolved from pegmatites and mixed with low temperature (<200 °C), lower salinity,
29
30 825 Ca-rich fluids to produce the observed Ca-metasomatism and Ca-bearing REE/HFSE
31
32 826 phases (Salvi and Williams-Jones, 1990, 1992, 1996, 1997). Recently, however,
33
34 827 Vasyukova and Williams-Jones (2014; 2016) provided melt inclusion evidence for the
35
36 828 presence of immiscible Ca-F-bearing melts, and proposed that these melts may have
37
38 829 accumulated in the pegmatites and been later dissolved by magmatic hydrothermal fluids.
39
40 830 This proposal is supported by observation of hydrothermal fluorite vugs and fluorite-
41
42 831 fluocerite solid solutions in the pegmatites (Gysi and Williams-Jones, 2013). Indeed,
43
44 832 there is considerable evidence for two separate sources of Ca, one that was responsible
45
46 833 for the Ca-metasomatism at high temperature (represented by early Ca-zirconosilicate
47
48 834 pseudomorphs in the pegmatites) when the pegmatite system was closed, and one
49
50
51
52
53
54
55
56
57
58
59
60
61
62
63
64
65

1
2
3
4 835 responsible for the low temperature Ca-F-metasomatic event (represented by late zircon,
5
6 836 gittinsite and fluorite in the granite), when the pegmatite system was open. Furthermore,
7
8
9 837 the presence of a large fluorite breccia surrounding the pluton in the northwest, south and
10
11 838 northeast (Fig. 1A), suggest strongly that most of the F and Ca did not originate from the
12
13 839 same source and were not transported together on any significant scale. It thus seems
14
15 840 likely that the fluids exsolved from the pegmatites were enriched in F but not Ca during
16
17 841 the low temperature acidic hydrothermal event, thereby enabling them to transport Zr and
18
19 842 REE as described previously. A possible explanation for this is that during the high
20
21 843 temperature acidic hydrothermal event, fluorite in the core pegmatites was more soluble,
22
23 844 as predicted by experiments (e.g. Tropper and Manning, 2007), which permitted a closed
24
25 845 system Ca-Na exchange during the formation of pseudomorphs in the border pegmatites.
26
27 846 This explanation is also supported by the reaction path model of Gysi and Williams-Jones
28
29 847 (2013), which predicts that during acidic alteration, fluorite from the core zone
30
31 848 pegmatites may have dissolved at very low pH. This Ca-Na exchange would have led to a
32
33 849 selective enrichment of the pegmatitic fluid in HF, whereas Ca was lost during the
34
35 850 formation of the pseudomorphs. The availability of F to complex with Zr on cooling
36
37 851 would explain the mobilization of Zr from the border pegmatites to the granites, as
38
39 852 indicated by the occurrence of hydrothermal zircon spherules in the latter (the presence of
40
41 853 Ca would have inhibited mobilization of Zr by destabilizing Zr hydroxyfluoride species
42
43 854 and crystallizing fluorite+zircon or gittinsite, Table 8). Support for this interpretation is
44
45 855 provided by the observation that the HREE content of zircon in the pegmatites correlates
46
47 856 positively with its F content and is independent of its Ca content (which is very low),
48
49 857 whereas the opposite is true for zircon in the granite, i.e., Ca and F were decoupled from
50
51
52
53
54
55
56
57
58
59
60
61
62
63
64
65

the HREE (Fig. 17 C-D). The high content of Ca in zircon in the granite but not in the pegmatite suggests that the Ca was supplied by external fluids, whereas the high content of F in zircon in the pegmatites and not in zircon in the granite suggests that F was supplied by fluids exsolving from the pegmatites.

862

863 *Genetic model for the deposit*

Based on field observations, the mineral paragenesis, and mineral and bulk rock chemistry, we conclude with a genetic model for the formation of the Strange Lake REE-Zr-Nb deposit (Figure 22). After intrusion of the hypersolvus granite, fractionation of feldspar in the parental magma chamber led to the saturation of H₂O and an increase in the concentration of volatiles and incompatible elements in the melt. This was followed by intrusion of the subsolvus granite along zones of structural weakness between the gneisses and monzonite that had previously been exploited by the hypersolvus granite magma (Fig. 22A). This magmatic stage (stage I) was accompanied by a continuous release of volatiles from the magma chamber and their accumulation along the walls (manifested by a large fluorite/hematite breccia) and roof of the intrusion, leading to conditions favorable for the formation of pegmatites. This fluid accumulation caused repetitive fracturing, and may also explain the occurrence of pegmatites in the B Zone and Main Zone (west and central parts of the pluton) and the overall horizontal sheet like distribution of the pegmatites at the roof of the intrusion. Crystallization of border pegmatites led to the formation of zones enriched in Zr and HREE due to the crystallization of zirconosilicates, whereas in the pegmatite cores, the addition of immiscible Ca-F-rich melts (Vasyukova and Williams-Jones, 2014), and/or the

881 exsolution of a fluid enriched in F and LREE may have led to the separation and
 882 **crystallization** of REE-F-CO₂-rich minerals [i.e., bastnäsite-(Ce) and fluocerite-(Ce)].
 883 The hydrothermal activity can be subdivided based on the fluid sources and evolution
 884 stages into: (II) alkali metasomatism; (IIIa) high temperature acidic alteration; and (IIIb)
 885 **low temperature acidic alteration** (Fig. 22B-D). During alkali metasomatism, **which was**
 886 **unrelated to the rare metal mineralization**, a high temperature orthomagmatic fluid, most
 887 likely derived from either the parental magma chamber or from the crystallizing melt of
 888 the subsolvus granite, replaced K-feldspar rims with albite **pervasively** in the granite via a
 889 Na-K exchange reaction. **This was followed by K-metasomatism, which was restricted to**
 890 **the border pegmatite**. The composition of this orthomagmatic fluid is constrained by fluid
 891 inclusion studies showing that it was a brine (**NaCl-KCl**) (Salvi and Williams-Jones,
 892 1992, 1997, 2006). Once the pegmatite border had crystallized, but prior to **complete**
 893 crystallization of the core, the magma exsolved an aqueous-carbonic fluid. This coincided
 894 with the onset of **high temperature** acidic alteration and the development of a closed
 895 system with a fluid-buffered **acidic** pH in the pegmatites cores (**Fig. 22C**). Alteration of
 896 the REE-F-CO₂-rich minerals **and fluorite** in the core pegmatite ensued, and there was
 897 local pseudomorphic replacement of zirconosilicates in the border pegmatite due to the
 898 availability of Ca from the core pegmatite **leading to Ca-Na exchange** (Ca-
 899 metasomatism). **The latter process led to an increase of F over Ca in the hydrothermal**
 900 **fluid**. Interaction of this fluid with the border pegmatite **and the adjacent granite**, which
 901 had a rock-buffered pH, also caused aegirization/**hematization** of arfvedsonite **forming**
 902 **an alteration halo restricted to the pegmatite spine**. Upon cooling, the pegmatitic fluids
 903 became more acidic **(due to dissociation of the acids) leading to the formation of the HF-**

1
2
3
4 904 HCl-rich fluid 1. The formation of quartz/fluorite veins (both barren and mineralized),
5
6 905 extending into the granite (Fig. 22 D), indicates an opening of the fluid-pegmatite system
7
8
9 906 and the release of the acidic HF-HCl-bearing fluids, which was accompanied by porosity
10
11 907 creation through mineral dissolution. During this process, low temperature, low pH and
12
13
14 908 availability of F⁻ to complex with Zr, led to destabilization of zirconosilicates in the
15
16 909 pegmatites (Gysi and Williams-Jones, 2013). This highly acidic fluid mobilized HREE
17
18
19 910 and Zr from the zirconosilicates and LREE from the REE-F-CO₂-rich minerals of the
20
21 911 pegmatite into the granite. Once the fluid mixed with the low temperature Ca-bearing
22
23
24 912 external meteoric fluid (fluid 2) on a large scale, gittinsite, zircon spherules, fluorite,
25
26 913 gadolinite-(Y) and ferriallanite-(Ce) precipitated and the hydrothermal breccia formed
27
28
29 914 along a zone of structural weakness. The essential ingredient for REE and Zr
30
31 915 mobilization was the formation of a pegmatite-rich zone in the roof of the intrusion where
32
33
34 916 fluids accumulated and pH was buffered to low values as temperature decreased.
35
36
37

38 918 **Conclusions**

39
40
41 919 The B Zone in the Strange Lake peralkaline granitic pluton underwent intense
42
43 920 hydrothermal alteration during complex post-magmatic hydrothermal processes.
44
45 921 Although primary REE and Zr enrichment was due to the fractionation of the subsolvus
46
47 922 granitic melt in a deep magma chamber and to the formation of pegmatites at the roof of
48
49
50 923 the intrusion, most of the primary mineralogy was not preserved. The remobilization of
51
52
53 924 REE and Zr resulted from the presence of HF- and HCl-bearing fluids capable of forming
54
55 925 aqueous complexes with Zr and REE, respectively. This led to their transport on a scale
56
57
58 926 of tens to hundreds of meters until termination of hydrothermal activity at low
59
60
61
62
63
64
65

1
2
3
4 927 temperature. Detailed mineralogical observations, in combination with the bulk rock
5
6 928 chemistry, made it possible to retrieve useful lithogeochemical vectors for the different
7
8
9 929 stages of fluid-rock interaction in the system, and showed how the corresponding
10
11 930 parameters affected the mobility of the REE and Zr. Thus, mobilization of HREE and Zr
12
13
14 931 was related to a **change in the CaO/Al₂O₃ ratio**, which yielded a vector for the **low**
15
16 932 **temperature** Ca-F-metasomatism; **the higher temperature** aegirinization and hematization
17
18
19 933 were traceable using the **Fe₂O₃/Na₂O ratio**. This study emphasizes the importance of
20
21 934 **relating** field studies **to** thermodynamic models of fluid-rock reaction, and shows how
22
23
24 935 such linkage can lead to practical lithogeochemical tools that can guide the exploration of
25
26 936 critical metals in peralkaline and alkaline igneous settings.
27
28
29 937

30 31 938 **Acknowledgements**

32
33 939 This project was funded by a fellowship from the Swiss National Science Foundation to
34
35
36 940 AG (SNSF grant PBSKP2_134329) and by NSERC Discovery and Industry
37
38 941 Collaborative grants and a grant from Quest Rare Minerals Ltd to AEW-J. Essential
39
40
41 942 logistical support was provided by P. Cashin and P. Guay and help in EMP analysis by L.
42
43 943 Shi. The manuscript benefited greatly from numerous discussions with N.C. Hurtig, R.
44
45 944 Martin, A. Migdisov, V. Moeller, K. Siegel and O. Vasyukova. We also appreciate the
46
47
48 945 support from P. Cashin and P. Guay and collaboration with Quest Rare Minerals Ltd.
49
50
51 946

52 53 947 **REFERENCES**

54
55 948 Armbruster, T., Bonazzi, P., Akasaka, M., Bermanec, V., Chopin, C., Gieré, R., Heuss-
56 949 Assbichler, S., Liebscher, A., Menchetti, S., Pan, Y., Pasero, M., 2006.
57 950 Recommended nomenclature of epidote-group minerals. European Journal of
58 951 Mineralogy 18, 551–567.
59
60
61
62
63
64
65

- 952 Bartels, A., Behrens, H., Holtz, F., Schmidt, B.C., Fechtelkord, M., Knipping, J., Crede,
953 L., Baasner, A., Pukallus, N., 2013. The effect of fluorine, boron and phosphorus on
954 the viscosity of pegmatite forming melts. *Chemical Geology* 346, 184–198.
- 955 Birkett, T.C., Trzcinski, W.E.Jr., Stirling, J.A.R., 1996. Occurrence and compositions of
956 some Ti-bearing minerals in the Strange Lake intrusive complex, Quebec-Labrador
957 boundary. *The Canadian Mineralogist* 34, 779–801.
- 958 Boily, M., Williams-Jones, A.E., 1994. The role of magmatic and hydrothermal processes
959 in the chemical evolution of the Strange Lake plutonic complex, Québec-Labrador.
960 *Contributions to Mineralogy and Petrology* 118, 33–47.
- 961 Chakrabarty, A., Mitchell, R.H., Ren, M., Sen, A.K., Pruseth, K.L., 2013. Rinkite,
962 cerianite-(Ce), and hingganite-(Ce) in syenite gneisses from the Sushina Hill
963 Complex, India: occurrence, compositional data and petrogenetic significance.
964 *Mineralogical Magazine* 77, 3137–3153.
- 965 DeMartin, F., Minaglia, A., Gramaccioli, C.M., 2001. Characterization of gadolinite-
966 group minerals using crystallographic data only: the case of hingganite-(Y) from
967 Cuasso Al Monte, Italy. *Canadian Mineralogist* 39, 1105–1114.
- 968 Gysi, A.P., Williams-Jones, A.E., 2013. Hydrothermal mobilization of pegmatite-hosted
969 REE and Zr at Strange Lake, Canada: A reaction path model. *Geochimica et*
970 *Cosmochimica Acta* 122, 324–352.
- 971 Gysi, A.P., Williams-Jones, A.E., 2015. The thermodynamic properties of bastnäsite-(Ce)
972 and parisite-(Ce). *Chemical Geology* 392, 87–101.
- 973 Gysi, A.P., Williams-Jones, A.E., Harlov, D., 2015. The solubility of xenotime-(Y) and
974 other HREE phosphates (DyPO₄, ErPO₄ and YbPO₄) in aqueous solutions from
975 100 to 250 °C and p_{sat}. *Chemical Geology* 401, 83–95.
- 976 Jambor, J.L., Roberts, A.C., Grice, J.D., Birkett, T.C., Groat, L.A., Zajac, S., 1998.
977 GERENITE-(Y), (Ca,Na)₂(Y,REE)₃Si₆O₁₈ · 2H₂O, a new mineral species, and an
978 associated Y-bearing Gadolinite-group mineral, from the Strange Lake peralkaline
979 complex, Quebec-Labrador. *Canadian Mineralogist* 36, 793–800.
- 980 Linnen, R., Keppler, H., 2002. Melt composition control of Zr/Hf fractionation in
981 magmatic processes. *Geochimica et Cosmochimica Acta* 66, 3293–3301.
- 982 Manning, D.A.C., 1981. The effect of fluorine on liquidus phase relationships in the
983 system Qz-Ab-Or with excess water at 1 kb. *Contributions to Mineralogy and*
984 *Petrology* 76, 206–215.

- 985 Martin, R., De Vito, C., 2014. The late-stage miniflood of Ca in granitic pegmatites: an
986 open-system acid-reflux model involving plagioclase in the exocontact. *Canadian*
987 *Mineralogist* 52, 165–181.
- 988 McDonough, W., 1995. The composition of the Earth. *Chemical Geology* 120, 223–253.
- 989 Migdisov, A. A., Williams-Jones, A. E., 2014. Hydrothermal transport and deposition of
990 the rare earth elements by fluorine-bearing aqueous liquids. *Mineral Deposita* 49,
991 987–997.
- 992 Migdisov, A.A., Williams-Jones, A.E., Wagner, T., 2009. An experimental study of the
993 solubility and speciation of the Rare Earth Elements (III) in fluoride- and chloride-
994 bearing aqueous solutions at temperatures up to 300°C. *Geochimica et*
995 *Cosmochimica Acta* 73, 7087-7109.
- 996 Migdisov, A.A., Williams-Jones, A.E., Van Hinsberg, V., Salvi, S., 2011. An
997 experimental study of the solubility of baddeleyite (ZrO₂) in fluoride-bearing
998 solutions at elevated temperature. *Geochimica et Cosmochimica Acta* 75, 7426–
999 7434.
- 1000 Miller, R., Heaman, L.M., Birkett, T.C., 1997. U-Pb zircon age of the Strange Lake
1001 peralkaline complex: implications for Mesoproterozoic peralkaline magmatism in
1002 north-central Labrador. *Precambrian Research* 81, 67–82.
- 1003 Miller, R., 1986. Geology of the Strange Lake alkalic complex and the associated Zr-Y-
1004 Nb-Be-REE mineralization. Current Research Newfoundland Department of Mines
1005 Energy Report 86-1, 11-19.
- 1006 Miller, R., 1990. The Strange Lake pegmatite-aplite-hosted rare-metal deposit, Labrador.
1007 Current Research Newfoundland Department of Mines Energy Report 90-1, 171-
1008 182.
- 1009 Miyawaki, R., Matsubara, S., Yokoyama, K., Okamoto, A., 2007. Hingganite-(Ce) and
1010 hingganite-(Y) from Tahara, Hirukawa-mura, Gifu Prefecture, Japan: The
1011 description on a new mineral species of the Ce-analogue of hingganite-(Y) with a
1012 refinement of the crystal structure of hingganite-(Y). *Journal of Mineralogical And*
1013 *Petrological Sciences* 102, 1–7.
- 1014 Nassif, G.J., 1993. The Strange Lake Peralkaline Complex, Québec– Labrador: the
1015 hypersolvus–subsolvus granite transition and feldspar mineralogy. Unpublished
1016 M.Sc. thesis, McGill Univ. 104.
- 1017 Petrík, I., Broska, I., Lipka, J., Šíman, P., 1995. Granitoid allanite-(Ce): substitution
1018 relations, redox conditions and REE distributions (on an example of I-type
1019 granitoids, Western Carpathians, Slovakia). *Geologica Carpathica* 46, 79–94.

- 1020 Pezzotta, F., Diella, V., Guastoni, A., 1999. Chemical and paragenetic data on gadolinite-
1021 group minerals from Baveno and Cuasso al Monte, southern Alps, Italy. *American*
1022 *Mineralogist* 84, 782–789.
- 1023 Pillet, D., Bonhomme, M.G., Duthou, J.L., Chenevoy, M., 1989. Chronologie Rb/Sr et
1024 K/Ar du granite peralcalin du lac Brisson, Labrador central, Nouveau-Québec.
1025 *Canadian Journal of Earth Sciences* 26, 328–332.
- 1026 Poitrasson, F., 2002. In situ investigations of allanite hydrothermal alteration: examples
1027 from calc-alkaline and anorogenic granites of Corsica (southeast France).
1028 *Contributions to Mineralogy and Petrology* 142, 485–500.
- 1029 Salvi, S., Williams-Jones, A.E., 1990. The role of hydrothermal processes in the granite-
1030 hosted Zr, Y, REE deposit at Strange Lake, Quebec/Labrador: evidence from fluid
1031 inclusions. *Geochimica et Cosmochimica Acta* 54, 2403–2418
- 1032 Salvi, S., Williams-Jones, A.E., 1992. Reduced orthomagmatic C-O-H-N-NaCl fluids in
1033 the Strange Lake rare-metal granitic complex, Quebec/Labrador, Canada. *European*
1034 *Journal of Mineralogy* 4, 1155–1174.
- 1035 Salvi, S., Williams-Jones, A.E., 1995. Zirconosilicate phase relations in the Strange Lake
1036 (Lac Brisson) pluton, Quebec-Labrador, Canada. *American Mineralogist* 80, 1031–
1037 1040.
- 1038 Salvi, S., Williams-Jones, A.E., 1996. The role of hydrothermal processes in
1039 concentrating high-field strength elements in the Strange Lake peralkaline complex,
1040 northeastern Canada. *Geochimica et Cosmochimica Acta* 60, 1917–1932.
- 1041 Salvi, S., Williams-Jones, A.E., 1997. Fischer-Tropsch synthesis of hydrocarbons during
1042 sub-solidus alteration of the Strange Lake peralkaline granite, Quebec/Labrador,
1043 Canada. *Geochimica et Cosmochimica Acta* 61, 83–99.
- 1044 Salvi, S., Williams-Jones, A.E., 2006. Alteration, HFSE mineralisation and hydrocarbon
1045 formation in peralkaline igneous systems: Insights from the Strange Lake Pluton,
1046 Canada. *Lithos* 91, 19–34.
- 1047 Salvi, S., Fontan, F., Monchoux, P., Williams-Jones, A.E., Moine, B., 2000.
1048 Hydrothermal Mobilization of High Field Strength Elements in Alkaline Igneous
1049 Systems: Evidence from the Tamazeght Complex (Morocco). *Economic Geology*
1050 95, 559–576.
- 1051 Segalstad, T.V., Larsen, A.O., 1978. Gadolinite-(Ce) from Skien, southwestern Oslo
1052 region, Norway. *American Mineralogist* 63, 188–195.

- 1053 Siegel, K., Williams-Jones, A.E., 2015. The amphiboles of the REE-enriched Strange
1054 Lake peralkaline granitic pluton - fingerprints of magma evolution. *Goldschmidt*
1055 Abstract 2892.
- 1056 Sheard, E., Williams-Jones, A., Heiligmann, M., 2012. Controls on the Concentration of
1057 Zirconium, Niobium, and the Rare Earth Elements in the Thor Lake Rare Metal
1058 Deposit, Northwest Territories, Canada. *Economic Geology* 107, 81–104.
- 1059 Thomas, R., Davidson, P., Beurlen, H., 2012. The competing models for the origin and
1060 internal evolution of granitic pegmatites in the light of melt and fluid inclusion
1061 research. *Mineralogy and Petrology* 106, 55–73.
- 1062 Tropper, P., Manning, C., 2007. The solubility of fluorite in H₂O and H₂O-NaCl at high
1063 pressure and temperature. *Geochimica et Cosmochimica Acta* 242, 299-306.
- 1064 Vasyukova, O., Williams-Jones, A.E., 2014. Fluoride–silicate melt immiscibility and its
1065 role in REE ore formation: Evidence from the Strange Lake rare metal deposit,
1066 Québec-Labrador, Canada. *Geochimica et Cosmochimica Acta* 139, 110–130.
- 1067 Vasyukova, O., Williams-Jones, A.E., 2016. The evolution of immiscible silicate and
1068 fluoride melts: Implications for REE ore-genesis. *Geochimica et Cosmochimica*
1069 *Acta* 172, 205-224.
- 1070 Vigneresse, J.L., 2007. The role of discontinuous magma inputs in felsic magma and ore
1071 generation. *Ore Geology Reviews* 30, 181–216.
- 1072 Vlach, S., 2012. Structural and compositional variations of hydrothermal epidote-group
1073 minerals from a peralkaline granite, Corupá Pluton, Graciosa Province, South Brazil.
1074 *Anais da Academia Brasileira de Ciencias* 84, 407–425.
- 1075 Williams-Jones, A. E., Migdisov, A. A., Samson, I.M., 2012. Hydrothermal Mobilisation
1076 of the Rare Earth Elements - a Tale of “Ceria” and “Yttria.” *Elements* 8, 355–360.

1077

1078 **FIGURE CAPTIONS**

1079 FIG. 1. A) Geological map of the Strange Lake peralkaline granitic pluton, showing the
1080 location of the two pegmatite-rich ore zones (the B Zone and Main Zone). B) A
1081 geological map of the B Zone, showing the distribution of the pegmatite spine, the
1082 fluorite breccia and the location of drill cores (BZ11176, BZ10027, BZ10078 and
1083 BZ11109) and the A-A' section investigated in this study. C) NE-SW section showing
1084 the lithological distribution with depth.

1085

FIG. 2. Geochemical model based on bulk rock data, showing the relative concentrations of LREO, HREO and ZrO₂ with depth along a NE-SW profile (section A-A' in Fig. 1B). Outlines show the location of the pegmatite sheets and squares indicate different domains of metal enrichment (zones 1 to 5). Zone 1: pegmatite spine enriched in LREO, HREO and ZrO₂; zone 2: granite enriched in ZrO₂ with subordinate LREO and HREO; zone 3: granite enriched in ZrO₂, LREO and HREO; zone 4: granite enriched in ZrO₂ and HREO with subordinate LREO; zone 5: granite only enriched in LREO.

FIG. 3. Drill core samples showing the different alteration types that affected the B Zone granites. A) Unaltered subsolvus granite with arfvedsonite phenocrysts and vlasovite (Na-zirconosilicate). B) Relict phenocrysts of hematized arfvedsonite and interstitial ferriallanite-(Ce) and zircon. C) Aegirized and partly hematized granite with interstitial zircon and fluorite. D) Granite subjected to pervasive Ca-F-metasomatism with a few relict arfvedsonite phenocrysts and interstitial hydrothermal ferriallanite-(Ce), gittinsite (Ca-zirconosilicate) and zircon mineralization. E) Drill core with a highly altered zone representative of a fluid conduit (top) and hematized arfvedsonite phenocrysts with a preserved igneous texture (bottom). Arf: arfvedsonite; Aeg: aegirine; Hem: hematite; Fl: fluorite; Zrn: zircon; Aln-(Ce): ferriallanite-(Ce); Gad-(Y): gadolinite-group minerals.

FIG. 4. Drill core samples illustrating the alteration/mineralization that affected the B Zone pegmatites. A) Border pegmatite with arfvedsonite and K-feldspar phenocrysts. B) Border pegmatite with pseudomorphs after narsarsukite forming a cumulate texture with zirconosilicates, quartz and K-feldspar. C) Border pegmatite with pseudomorphs after elpidite (Na-zirconosilicate), aegirized/hematized arfvedsonite relicts and K-feldspar. D) Core pegmatite with hydrothermal quartz, fluorite, zircon and bastnäsite-(Ce). E) Strongly mineralized layer in pegmatite with hydrothermal quartz, fluorite and gadolinite-group minerals. Qtz: quartz, Kfs: K-feldspar; Elp: pseudomorphs after elpidite; Bast-(Ce): bastnäsite-(Ce). Other mineral abbreviations are the same as in Fig. 1.

FIG. 5. Backscattered electron images of textures showing evidence of alkali metasomatism, and WDS element X-ray maps. A) Partially albitized K-feldspar phenocryst in granite. B) Replacement of albite lamellae by K-feldspar in a K-feldspar phenocryst of a pegmatite. C-D) Element X-ray maps showing the distribution of K as patches in the phenocryst and Na in albite lamellae relicts. Ab: albite; Kfs: K-feldspar; Qtz: quartz.

FIG. 6. Drill core samples showing textures related to veining and brecciation. A) Barren quartz vein crosscutting a hematized granite. B) Quartz/fluorite vein containing ferriallanite-(Ce), titanite and gadolinite-group minerals crosscutting an aegirized granite. C) Fluorite vein and veinlets showing colloform zoning. D) Contact of a border pegmatite and granite and micro-breccia filled with hydrothermal fluorite. E) Fluorite/hematite breccia with fragments of gneiss showing evidence of repetitive brecciation.

FIG. 7. Thin section photomicrographs in plain and polarized light showing REE- and Zr-bearing minerals in the granite (A-B) and pegmatite (C-D). A) Primary interstitial

vlasovite (Na-zirconosilicate) with dark patches of REE-bearing minerals. B) Gittinsite (Ca-zirconosilicate) and quartz at the contact with hydrothermal zircon spherules and fluorite. C) Interstitial ferriallanite-(Ce). D) Spherules of hydrothermal gadolinite-group minerals, fluorite and quartz. Qtz: quartz, Kfs: K-feldspar; Ab: albite; Fl: fluorite; Zrn: zircon; Git: gittinsite; Aln-(Ce): ferriallanite-(Ce); Gad-(Y): gadolinite-group minerals.

FIG. 8. Backscattered electron images showing relicts of primary REE- and Zr-bearing minerals in the granite (A-C) and pegmatite (D-E). D) and F) are pseudomorphs after elpidite and narsarsukite, respectively. Qtz: quartz; Git: gittinsite; Gag-(Y): gagarinite-(Y); Ttn: titanite; Bast-(Ce): bastnäsite-(Ce); Gad-(Y): gadolinite-group minerals.

FIG. 9. Backscattered electron images showing hydrothermal textures involving REE-, Zr- and Ti-bearing minerals in the granite (A-B), pegmatite (C) and in quartz/fluorite veins (D-F). A) Interstitial secondary zircon spherules, gittinsite, ferriallanite-(Ce) and quartz replacing primary K-feldspar. B) Fractures filled with quartz, ferriallanite-(Ce) and gadolinite-group minerals. C) Fractured quartz and an intergrowth of gittinsite and quartz. D) Ferriallanite-(Ce) forming a fibrous intergrowth in a quartz/fluorite vein. E) Quartz and fluorite vein with euhedral titanite crystals that grew on the fluorite. F) Veinlets filled with gadolinite-group minerals and patches of ferriallanite-(Ce) and titanite in hydrothermal quartz.

FIG. 10. Backscattered electron images and WDS element X-ray maps of A) interstitial ferriallanite-(Ce) and a gittinsite intergrowth in granite displaying patches enriched in La and Y, and B) colloform growth of gadolinite-group minerals displaying zoning with cores enriched in the lighter REE (i.e., Dy and Gd) and rims enriched in the heavier REE (i.e., Y and Yb).

FIG. 11. Backscattered electron images and WDS element X-ray maps showing zircon veinlets and a fluorite vein crosscutting an arfvedsonite crystal that has been replaced by aegirine and quartz during aegirinization. This texture provides evidence of low temperature hydrothermal Zr transport during Ca-F-metasomatism (low temperature acidic alteration, IIIb), which occurred after aegirinization/hematization (high temperature acidic alteration, IIIa).

FIG. 12. Mineral paragenesis summarizing the magmatic mineralogy, alteration types, textures and secondary mineralogy interpreted from field relations (Figs. 3-11). See text for details on the different alteration types.

FIG. 13. Bulk rock composition (in wt. %) of HREO, LREO, Nb₂O₅ and ZrO₂ in drill core samples with depth along the NE-SW section (Fig. 1B).

FIG. 14. Mineral chemistry of hydrothermal ferriallanite-(Ce). Symbol shapes are categorized by lithology. Symbol colors correspond to: (f): microfractures; (v) veining;

(rp/p) mineral replacement and pore space fillings. A) Diagram showing the element substitution mechanisms in epidote-group minerals and the method for estimating $\text{Fe}^{3+}/(\text{Fe}^{3+}+\text{Fe}^{2+})$ of Petrák et al. (1995). B) and C) Diagrams showing element substitution mechanisms involving REE, Ca, Al and Fe. Note that samples of ferriallanite-(Ce) occurring in (f) and (v) have the lowest $\text{Fe}^{3+}/(\text{Fe}^{3+}+\text{Fe}^{2+})$ ratios.

Fig. 15. Mineral chemistry of hydrothermal gadolinite-group minerals. A) Ternary Ca-Si- REE_{tot} diagram in mol % cations for samples in A) granites and B) pegmatites. C) Ca vs. total REE showing a negative correlation of REE with Ca in both pegmatites and granites.

FIG. 16. Chondrite-normalized (McDonough, 1995) REE profiles of gadolinite-group minerals from A) granites and B) pegmatites. C) Gadolinite-group minerals from a variety of localities: Gadolinite-(Y)/Hingganite-(Y) from miarolitic cavities in granophyre from Baveno and Cuasso al Monte, Southern Alps, Italy (Pezzotta et al., 1999); Gadolinite-(Ce) from a syenite pegmatite near Skien, Norway (Segalstad and Larsen, 1978); Hingganite-(Y) from pegmatite at Hirukawa-mura, Japan (Miyawaki et al., 2007); Hingganite-(Ce) and Gerenite-(Y) from pegmatites at Strange Lake (Jambor et al., 1998).

FIG. 17. Ternary Na-Ca-Zr/(Zr+Si) diagram in mol % cations for zirconosilicates in A) granites and B) pegmatites, showing the compositions corresponding to vlasovite, gittinsite, armstrongite and zircon. Shaded areas correspond to data for Strange Lake from Salvi and Williams-Jones (1995). C) and D) Binary plots of HREE vs F and Ca, respectively, in hydrothermal zircon from pegmatites and granites. Note the difference in the correlations for zircon compared to ferriallanite-(Ce) (Fig. 14B) and gadolinite-group minerals (Fig. 15C).

FIG. 18. Chondrite-normalized (McDonough, 1995) REE profiles of hydrothermal zircons from A) granites and B) pegmatites showing LREE enriched patterns in some zircon crystals.

FIG. 19. Compositions of pyrochlore and hydrothermal titanite. A) and B) Fe and F vs. Ti in titanite showing a negative correlation with Ti; the compositions of vein-hosted titanite are closer to that of titanite in the granite than in the pegmatite. C) Total REE vs. Ca showing a negative correlation for pyrochlore, similar to that for hydrothermal ferriallanite-(Ce) and gadolinite-group minerals. D) F vs. Na showing a positive correlation for pyrochlore, indicating that Ca and F may have been decoupled in the pegmatites.

FIG. 20. Lithogeochemical variation diagrams showing trends in bulk rock composition (in wt. %) for different alteration types based on the reactions listed in Table 8. A) $\text{Fe}_2\text{O}_3^*/\text{Na}_2\text{O}$ vs. $\text{CaO}/\text{Al}_2\text{O}_3$ showing aegiritized/hematized vs. Ca-F-metasomatized rocks. B) $\text{Fe}_2\text{O}_3^*/\text{Na}_2\text{O}$ vs. $\text{CaO}/\text{Na}_2\text{O}$ indicating that aegirization/hematization was overprinted by Ca-F-metasomatism. C) $\text{CaO}/\text{Na}_2\text{O}$ vs. $\text{CaO}/\text{Al}_2\text{O}_3$ showing trends for Ca-metasomatism (pseudomorphs Na-/Ca-zirconosilicates) and Ca-F-metasomatism

(hydrothermal zircon spherules, gittinsite, quartz, fluorite and ferriallanite-(Ce)). D-F) Density plots showing an increase of HREO and ZrO_2 with Ca-F-metasomatism ($\text{CaO}/\text{Al}_2\text{O}_3$); LREO concentration is relatively constant. Fe_2O_3^* corresponds to total Fe. Data have been separated (red for **high temperature acidic alteration**; turquoise for **low temperature acidic alteration**) based on $\text{Fe}_2\text{O}_3^*/\text{Na}_2\text{O}$ vs. $\text{CaO}/\text{Al}_2\text{O}_3$ ratios.

FIG. 21. Schematic model of subsolidus pegmatite evolution illustrating the different stages of **acidic alteration (Ca-metasomatism, aegirinization/hematization and Ca-F-metasomatism)**, the associated REE and Zr mobilization, and the chemical evolution of the three different zircon types. **A)** the formation of zircon I (LREE-depleted and HREE-enriched REE profiles; red) during Ca-metasomatism and pseudomorphic mineral replacement in a closed system. **B)** Mobilization of the LREE during **high temperature acidic alteration** and the formation of zircon II (LREE-enriched REE profiles; blue). **C)** involved open system Ca-F-metasomatism, mobilization of REE and Zr and the formation of zircon spherules (zircon III) in the granite (LREE-enriched REE profiles; blue). Intermediate zircon compositions (green) indicate complex processes of HREE depletion and LREE enrichment of zircon I.

FIG. 22. A schematic model for the emplacement of the Strange Lake peralkaline granitic pluton and the stages of fluid-rock interaction responsible for the observed alteration types. **A)** **Magmatic stage with the emplacement** of the pluton and accumulation of volatiles originating from a deep magma chamber and rising along structural weaknesses (contacts with gneiss and monzonite) towards the roof of the intrusion. Three hydrothermal stages are distinguished in the **B Zone**: **B)** **alkali metasomatism**, **C)** **high temperature acidic alteration** and **D)** **low temperature acidic alteration**. **B)** **Alkali metasomatic stage with pervasive Na-metasomatism in the granite and K-metasomatism restricted to the pegmatite border**. **C)** **Closed system high temperature acidic alteration with a fluid exsolved from the pegmatite core, leading to dissolution of fluorite and bastnäsité-(Ce), enrichment in Ca and F (and LREE), and pseudomorphic mineral replacement reactions (Ca-metasomatism) in the border pegmatite**. This stage also involved the formation of an alteration halo around the pegmatite spine, where the fluids had a rock buffered pH. **D)** **Open system low temperature acidic alteration by a HF-HCl-rich fluid (Fluid 1, Ca-depleted by Ca-metasomatism) capable of transporting REE and Zr**. This fluid led to the formation of Zr-REE mineralized quartz/fluorite veins due to mixing with a meteoric Ca-bearing fluid (fluid 2). Also shown is the late fluorite breccia indicating a late stage mixing of fluid 1 and fluid 2.

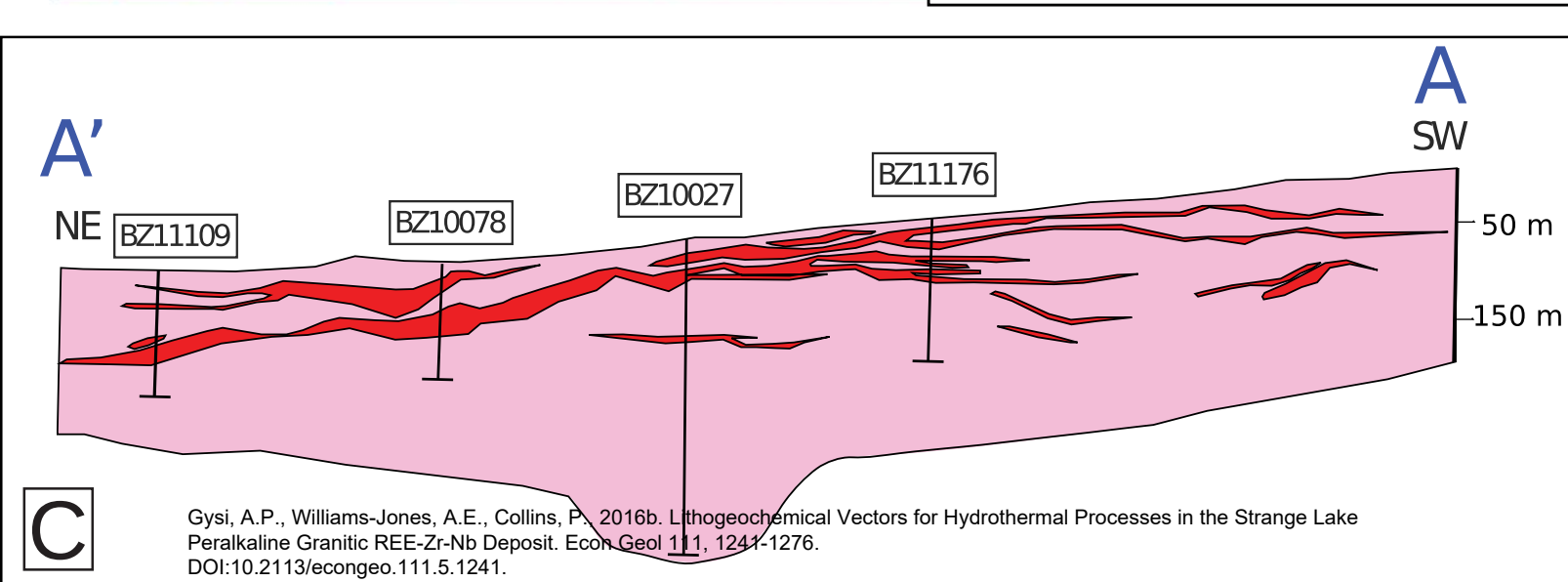
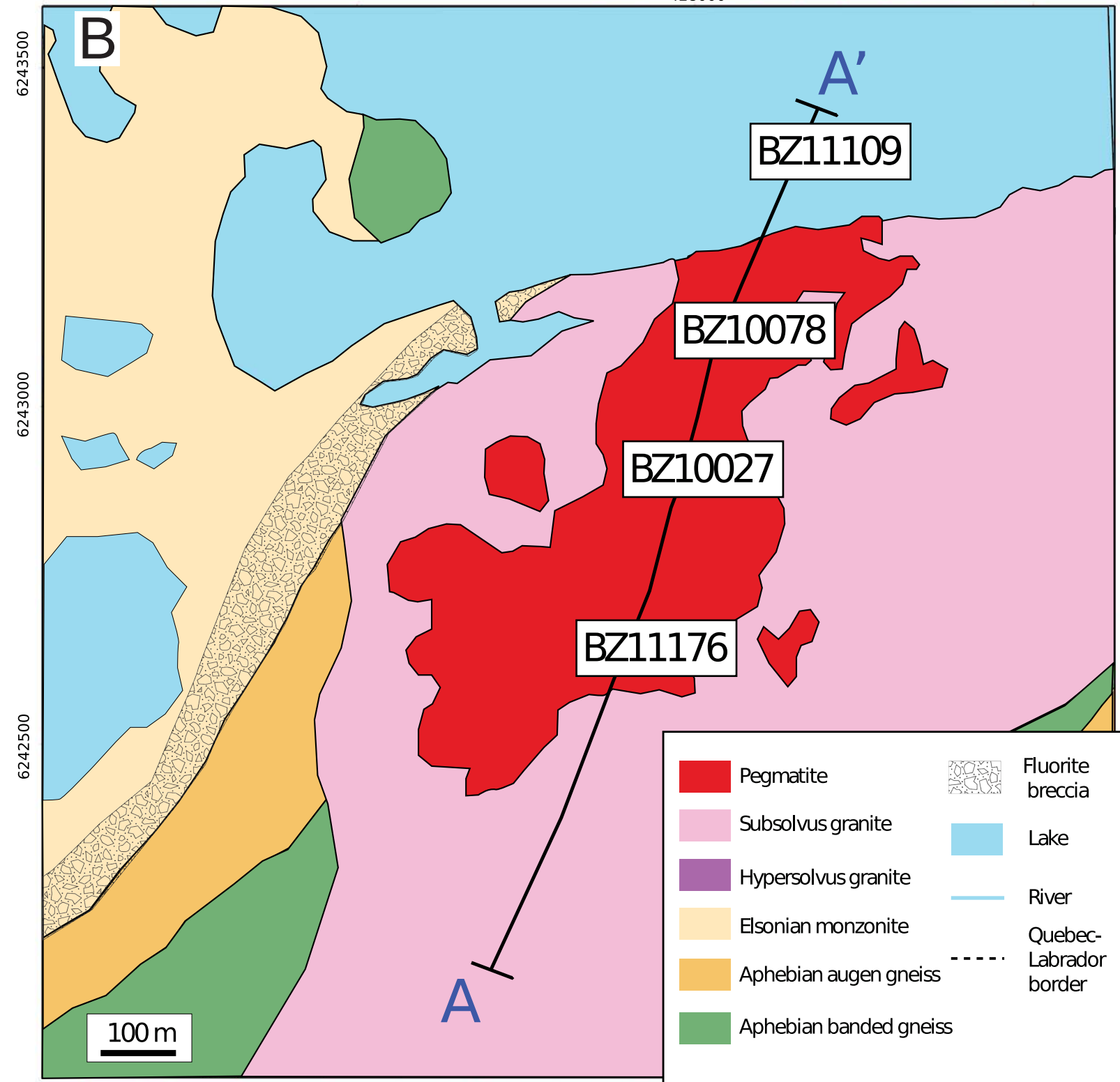
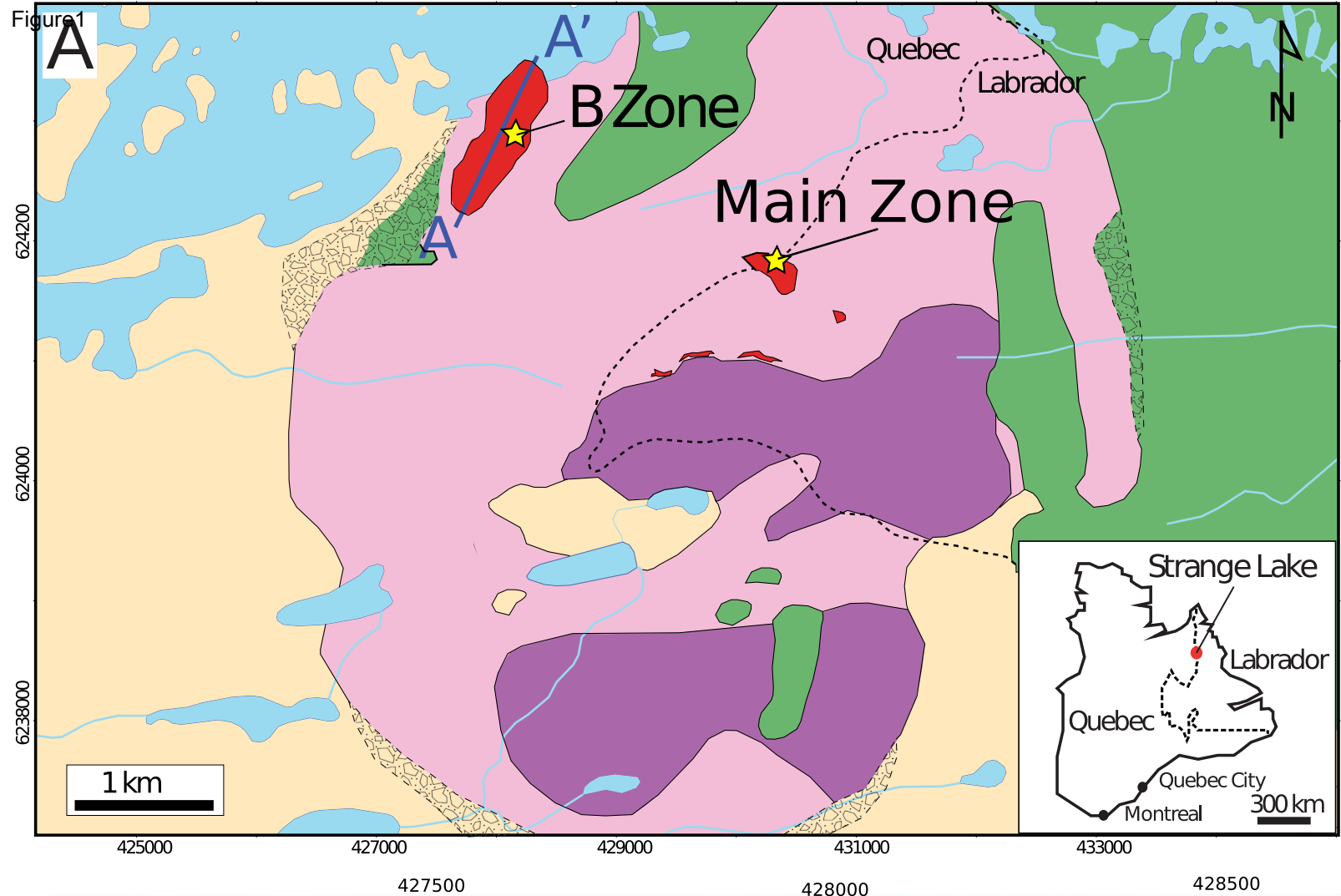
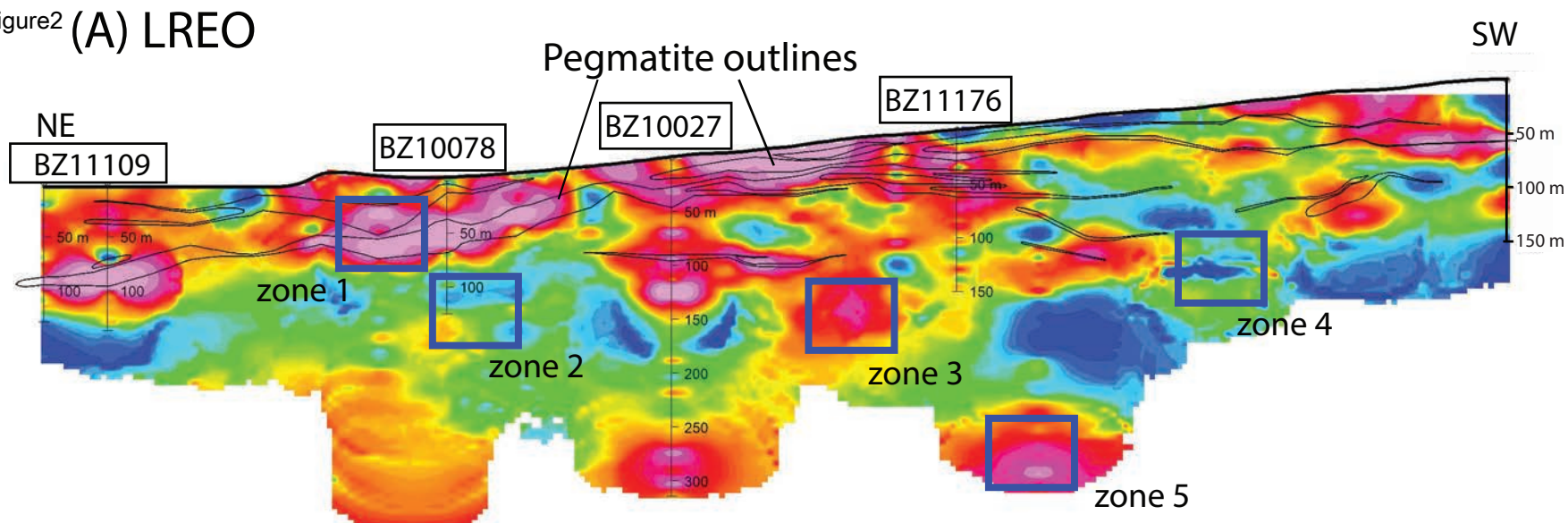
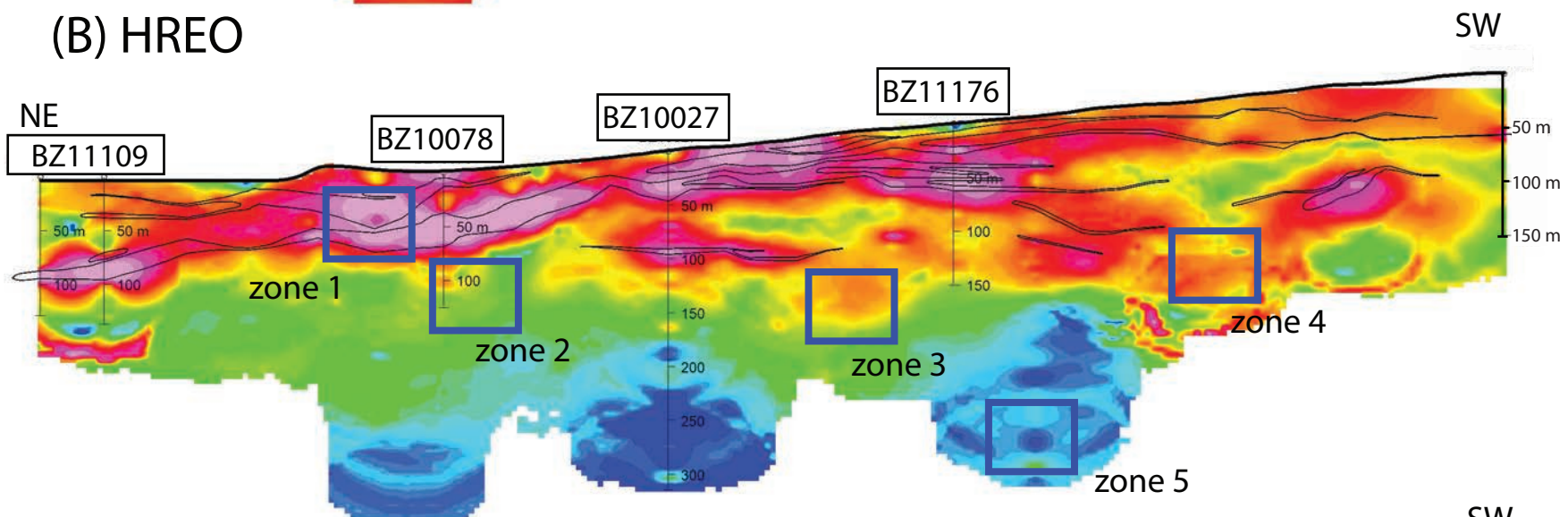


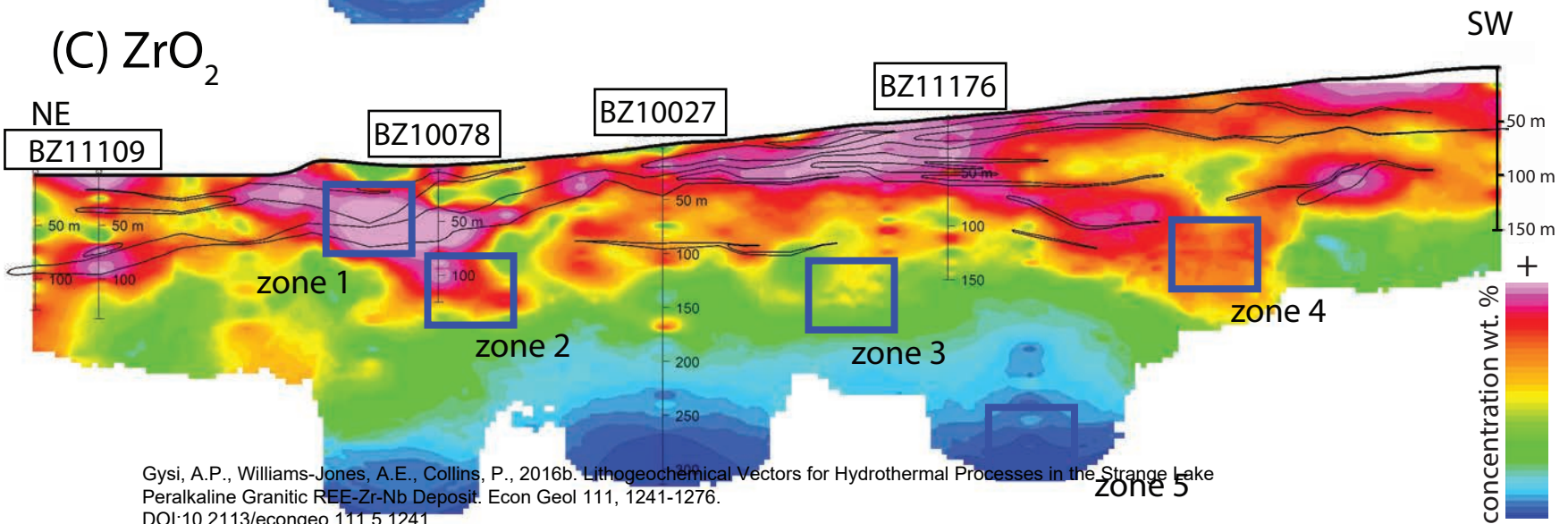
Figure 2 (A) LREO

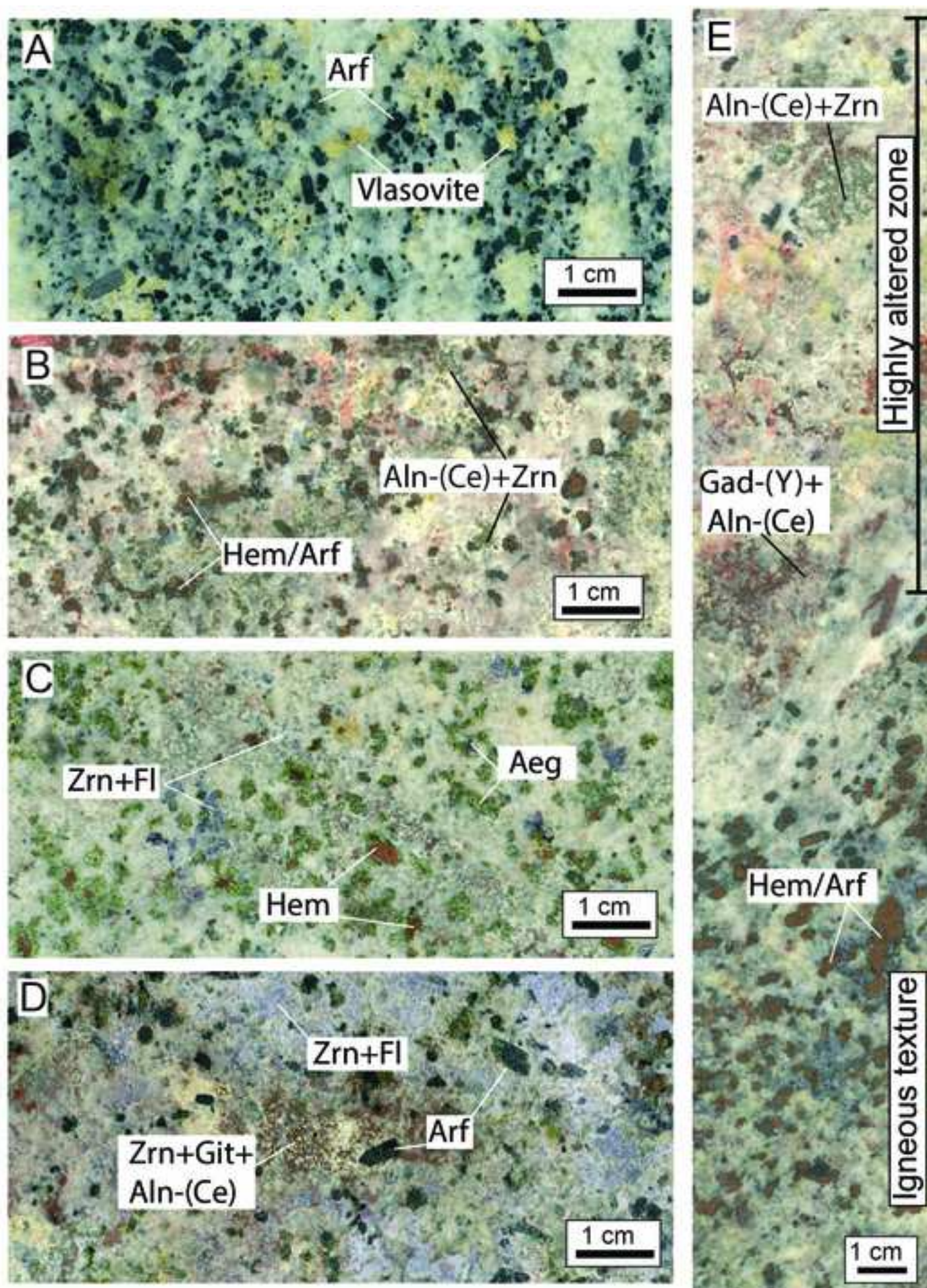


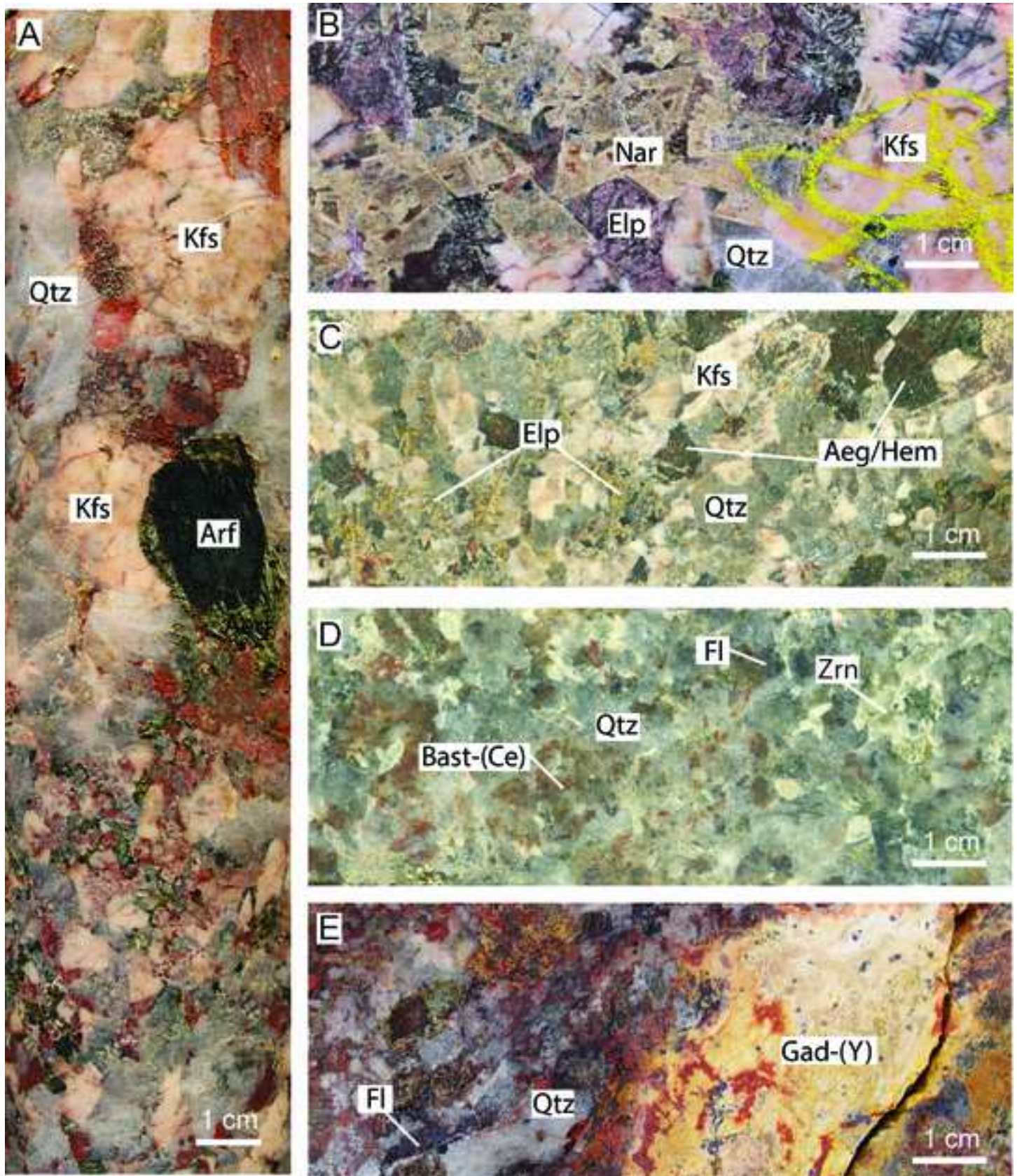
(B) HREO

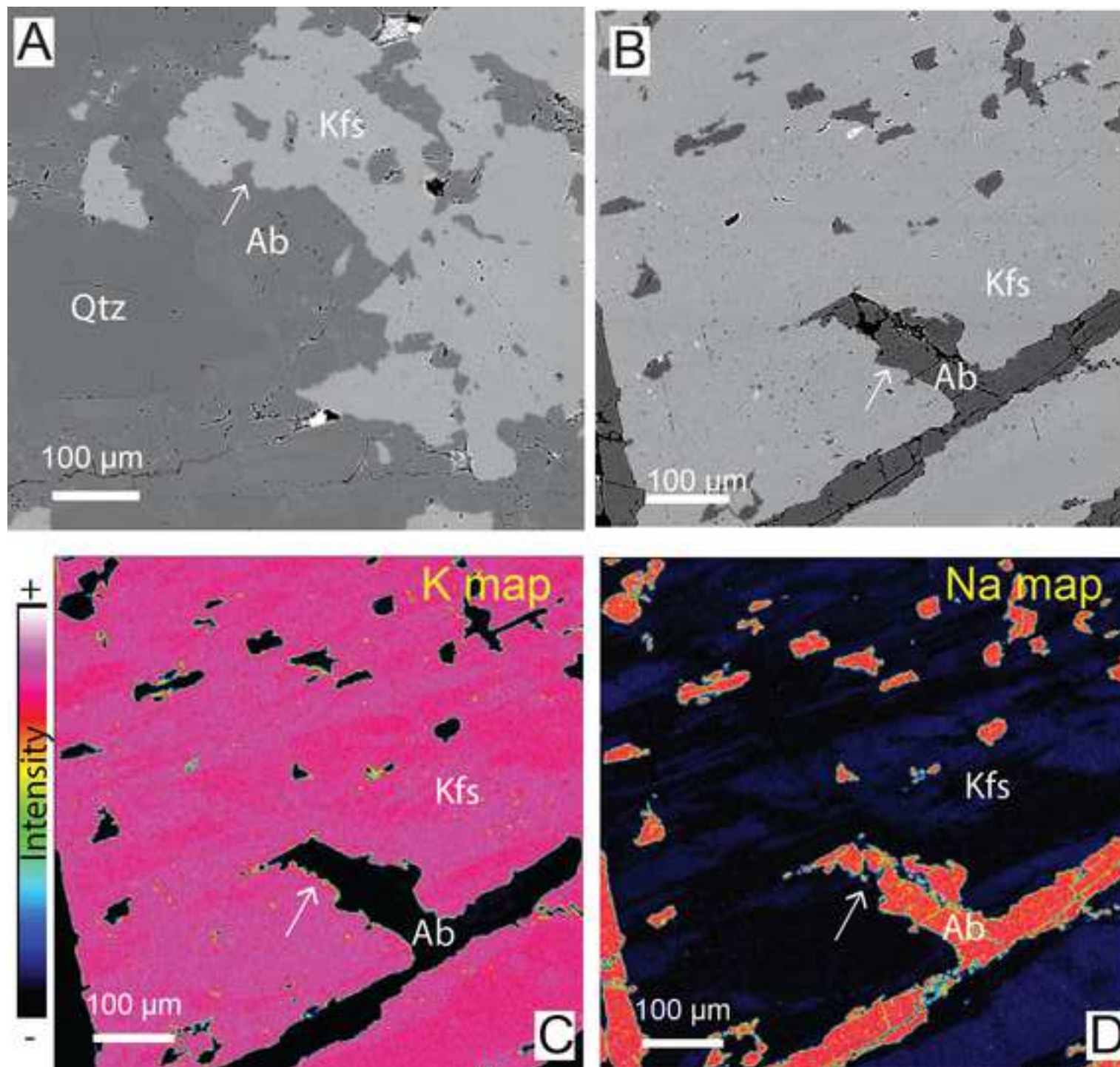


(C) ZrO_2

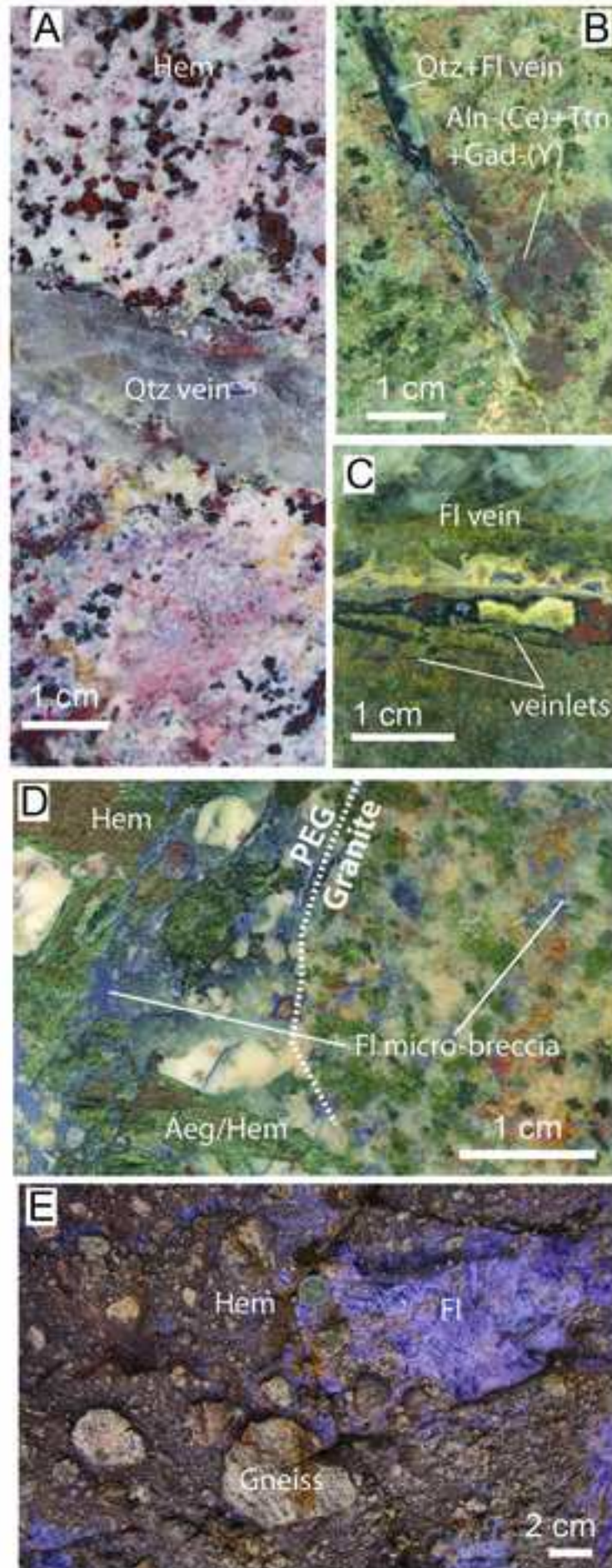


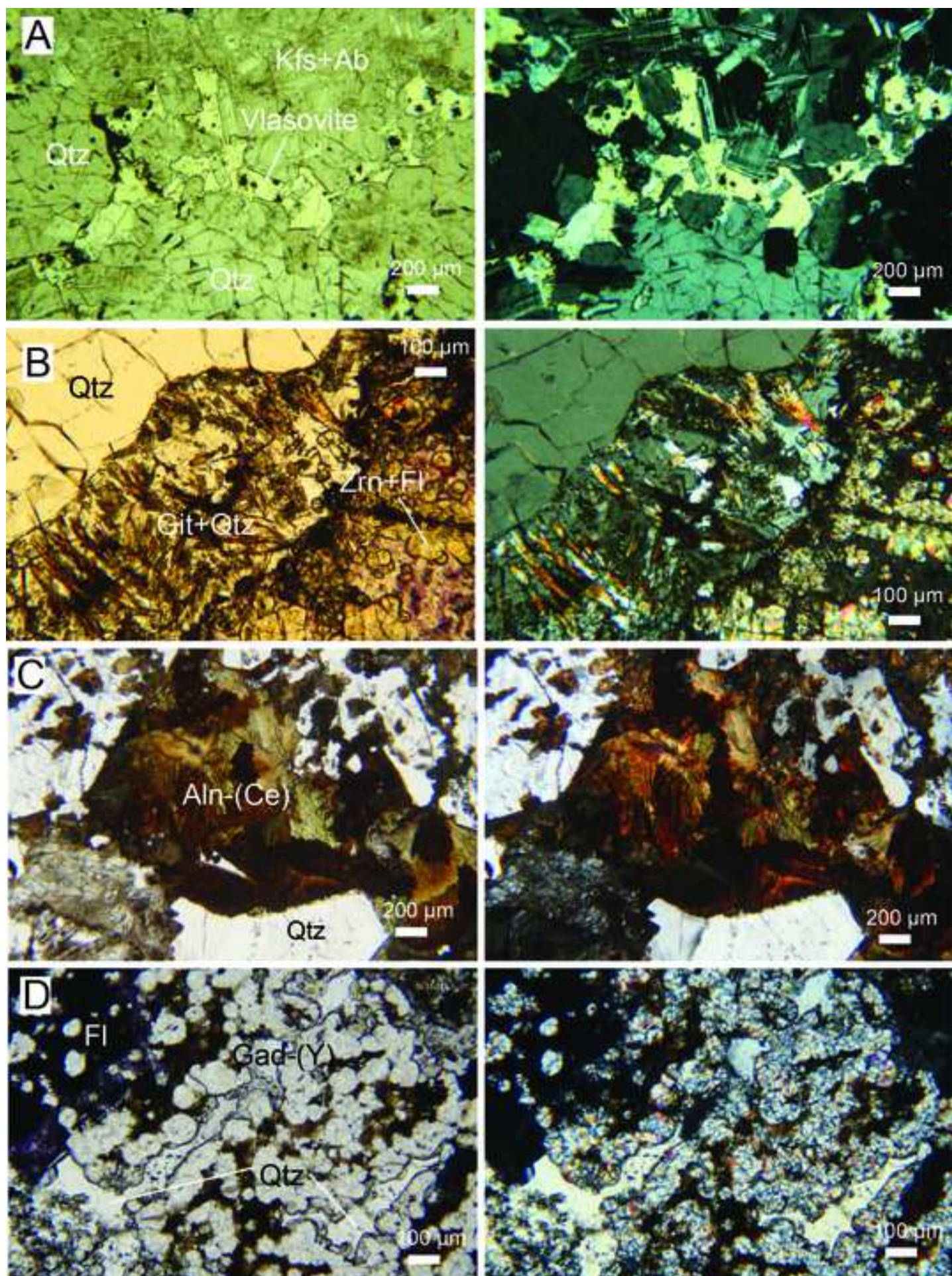




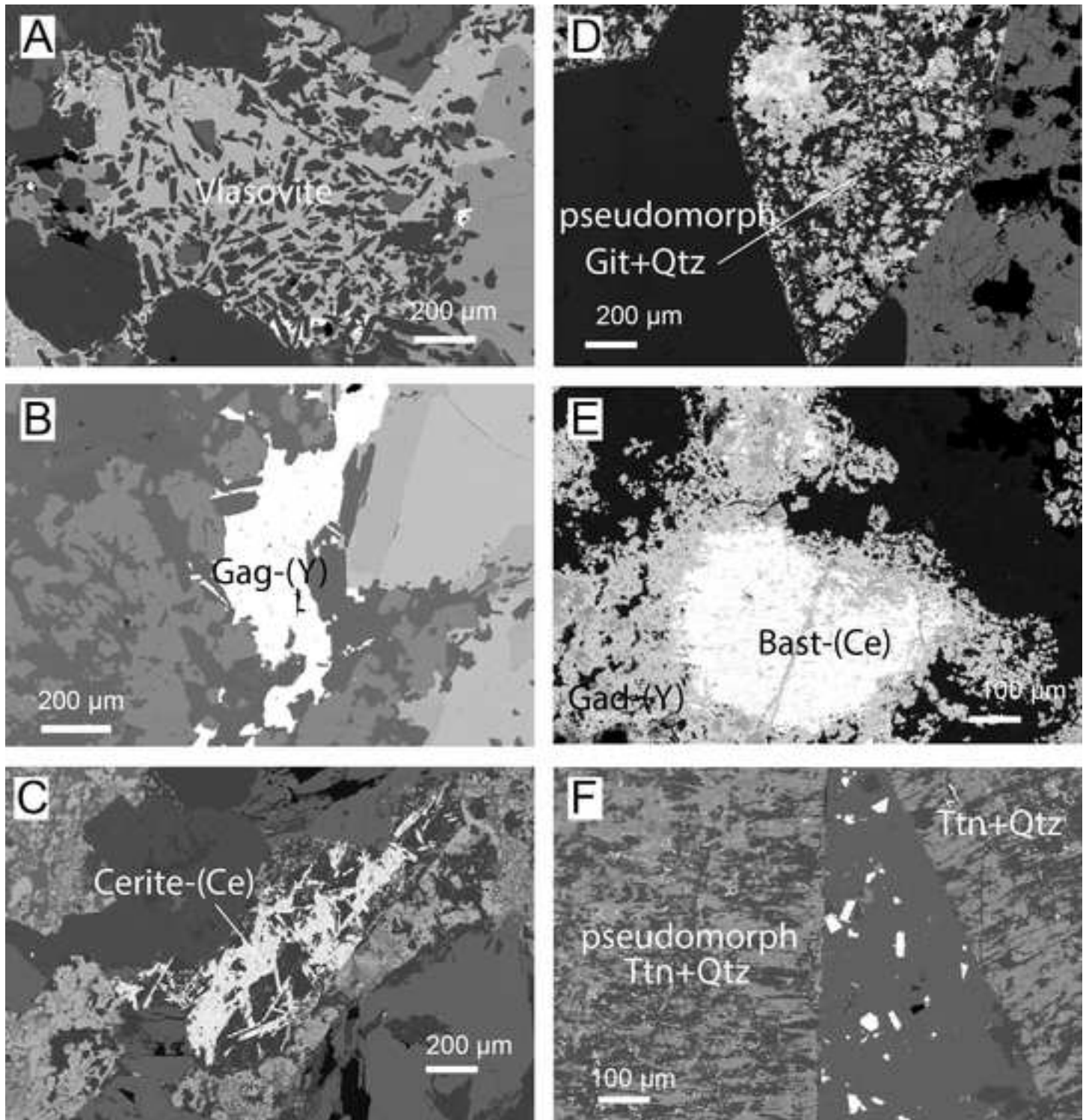


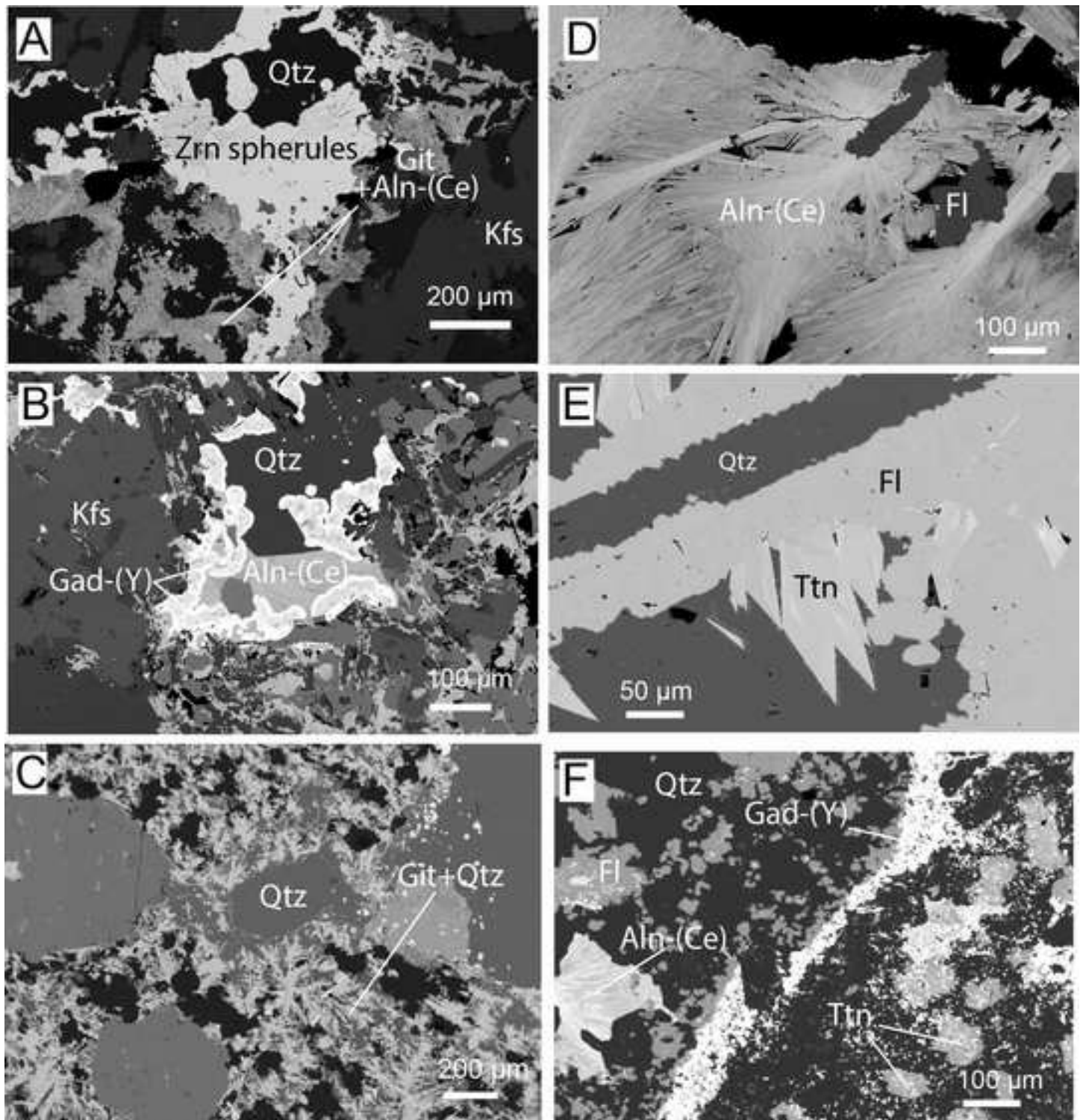
Gysi, A.P., Williams-Jones, A.E., Collins, P., 2016b. Lithogeochemical Vectors for Hydrothermal Processes in the Strange Lake Peralkaline Granitic REE-Zr-Nb Deposit. *Econ Geol* 111, 1241-1276.
DOI:10.2113/econgeo.111.5.1241.

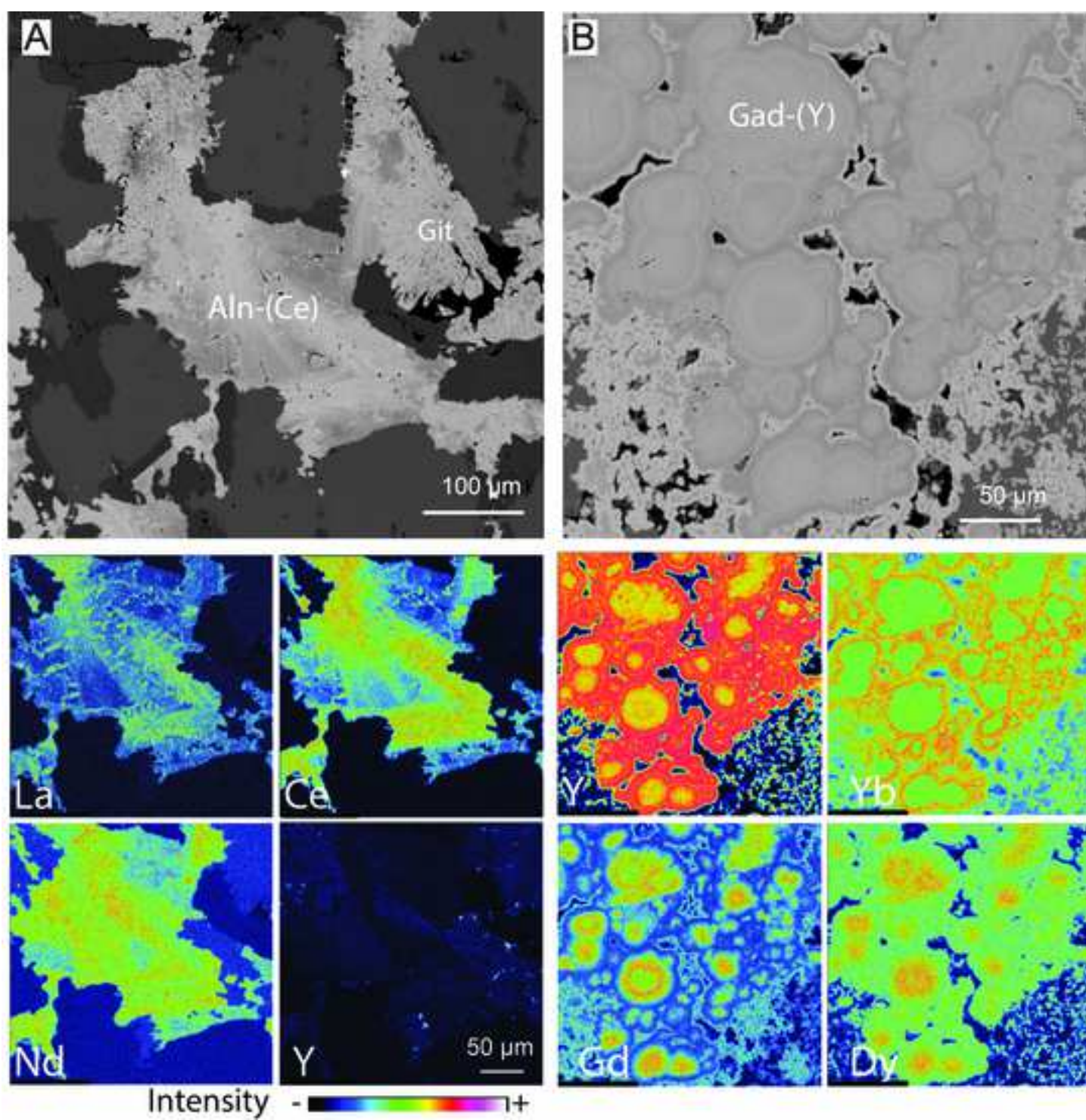




Gysi, A.P., Williams-Jones, A.E., Collins, P., 2016b. Lithogeochemical Vectors for Hydrothermal Processes in the Strange Lake Peralkaline Granitic REE-Zr-Nb Deposit. *Econ Geol* 111, 1241-1276.
DOI:10.2113/econgeo.111.5.1241.







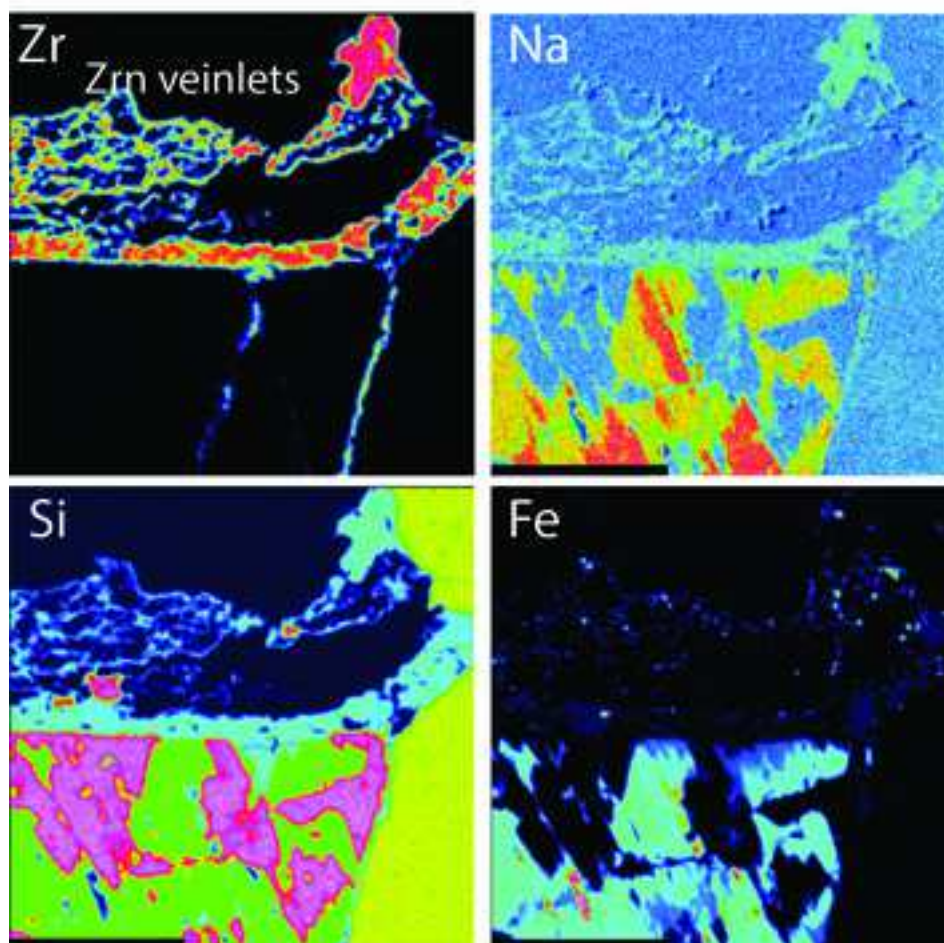
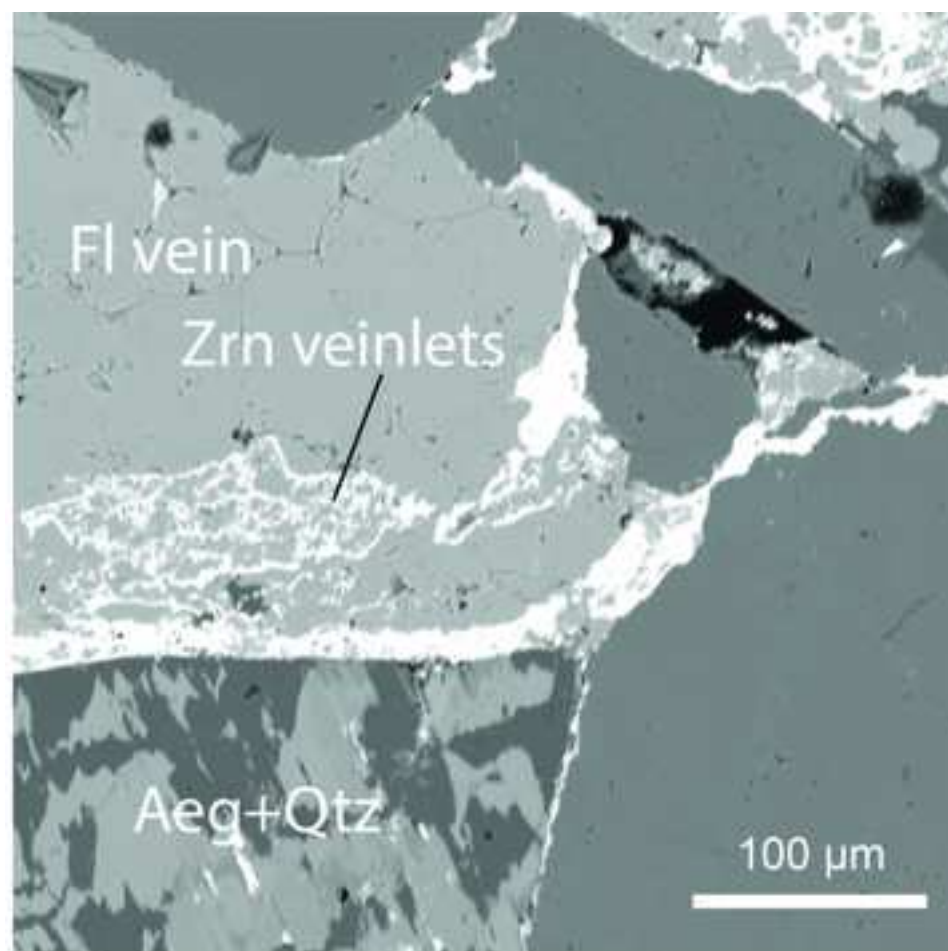


Figure 12

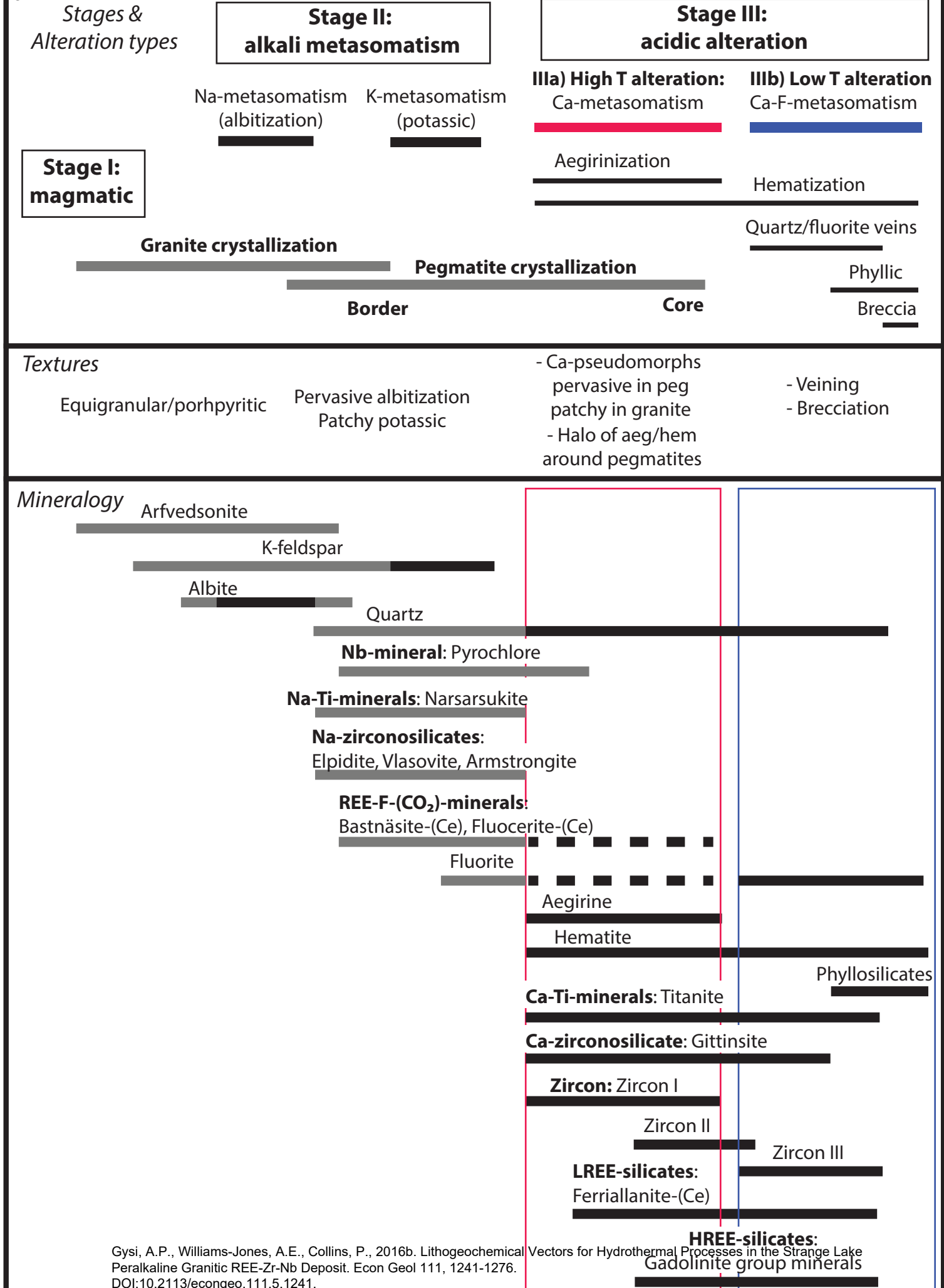


Figure 43

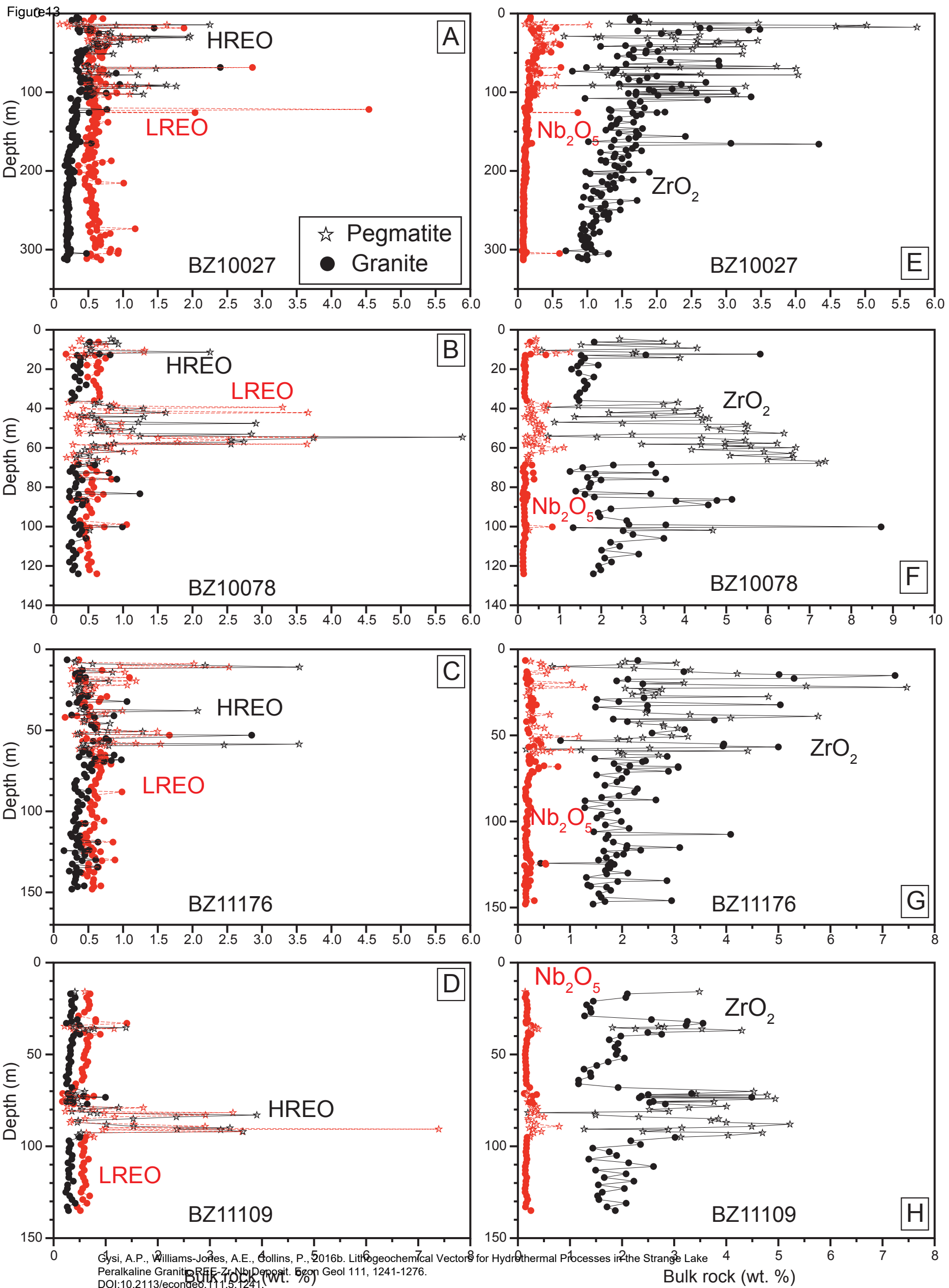


Figure 14

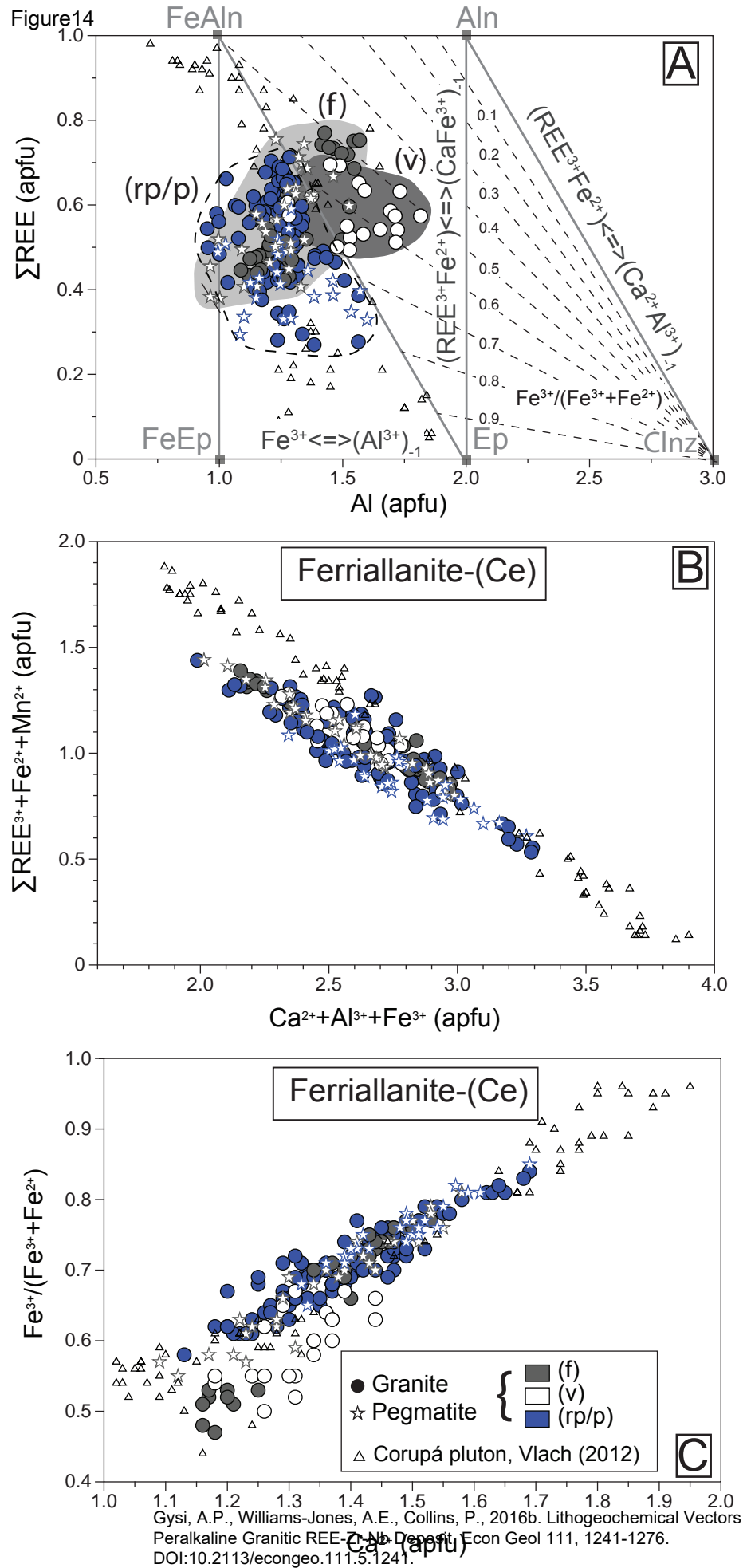
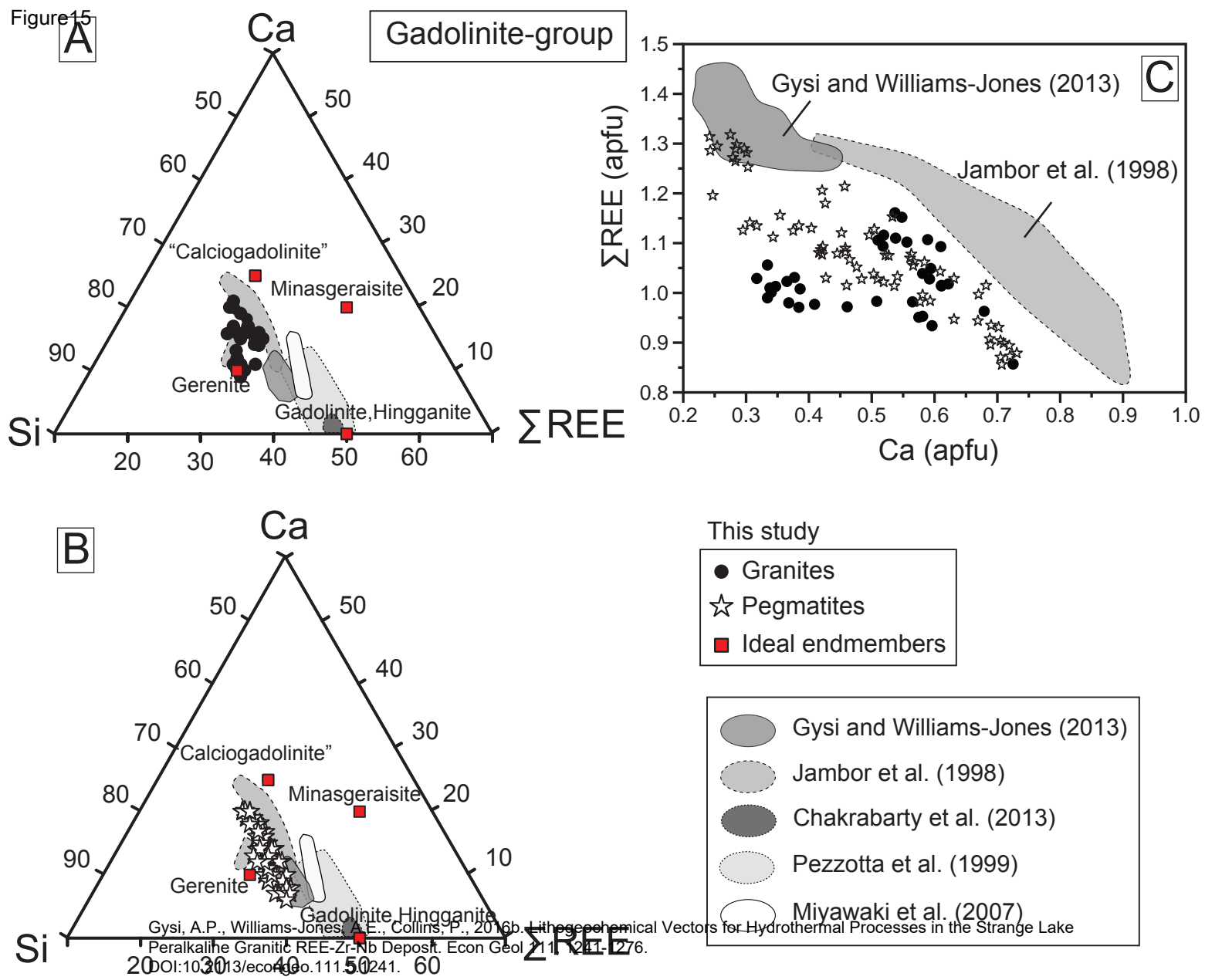


Figure 15



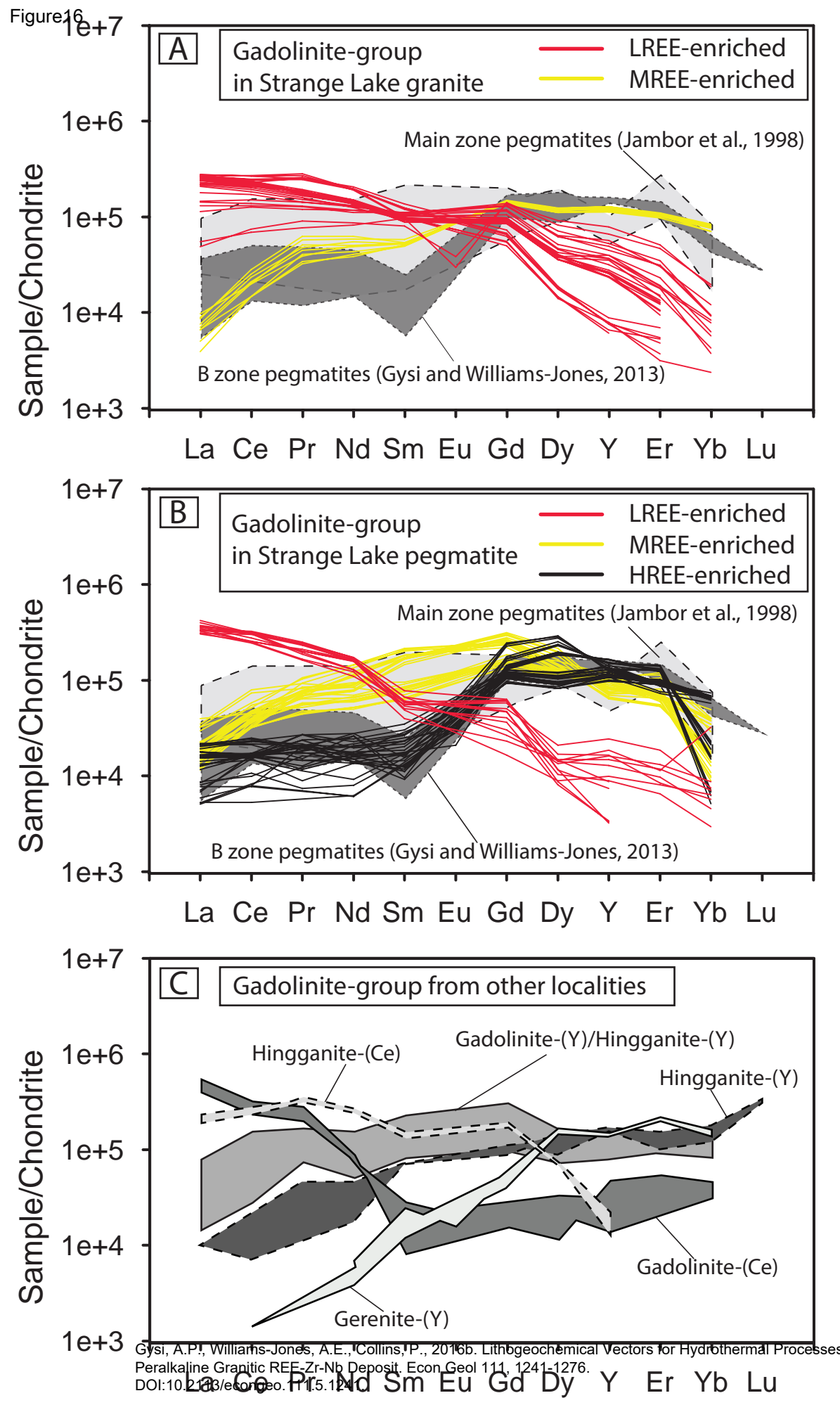


Figure17

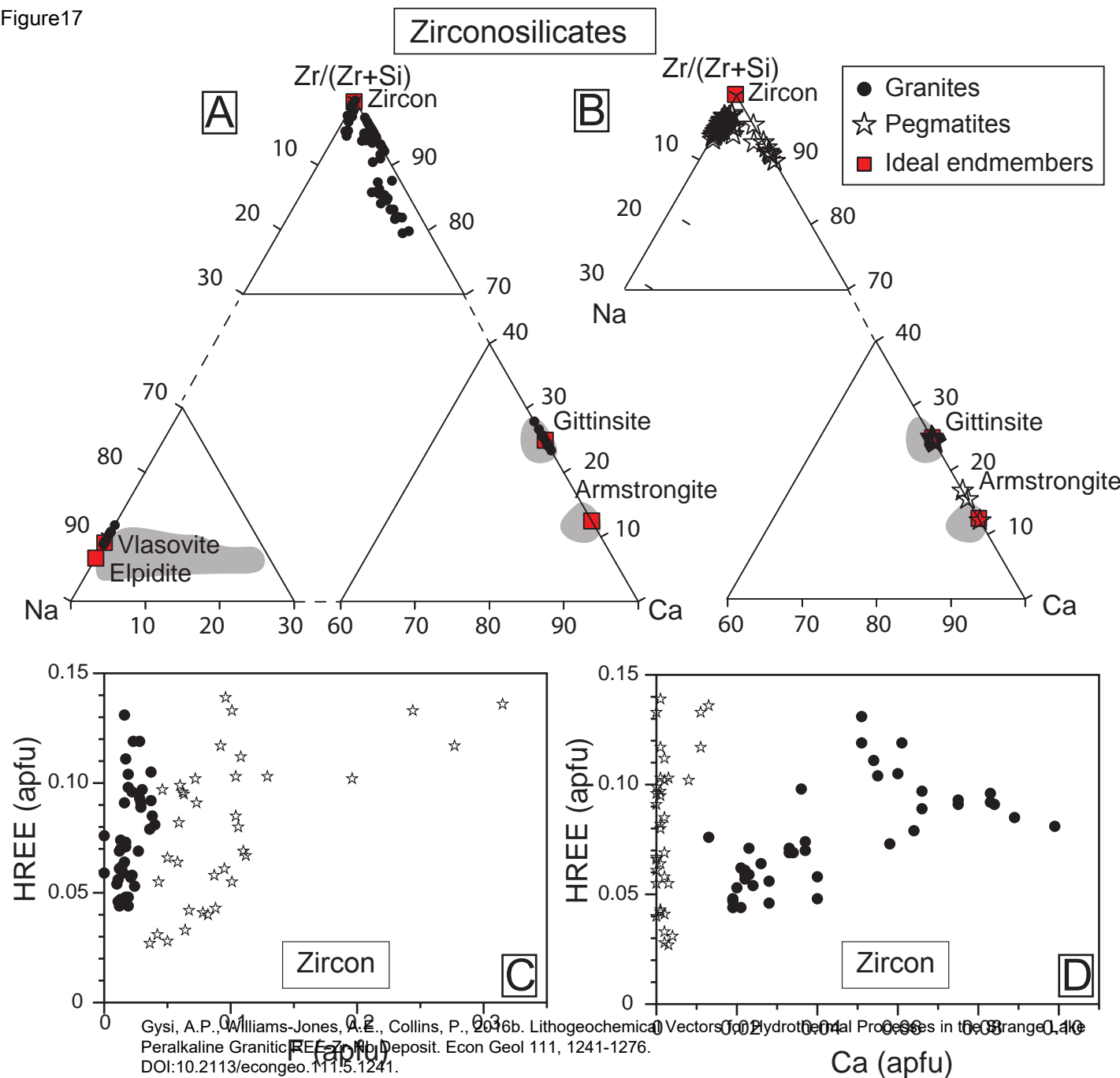
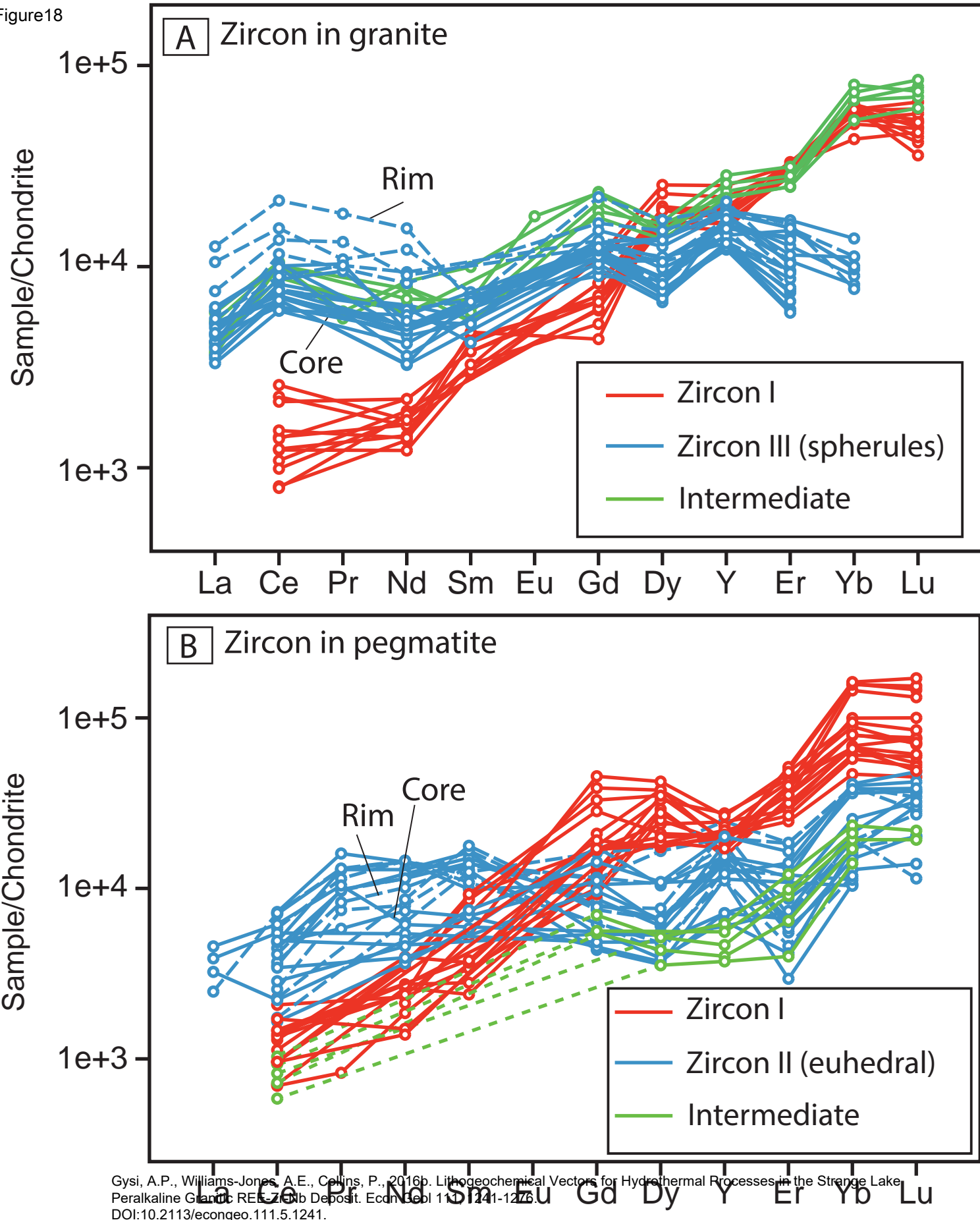


Figure 18



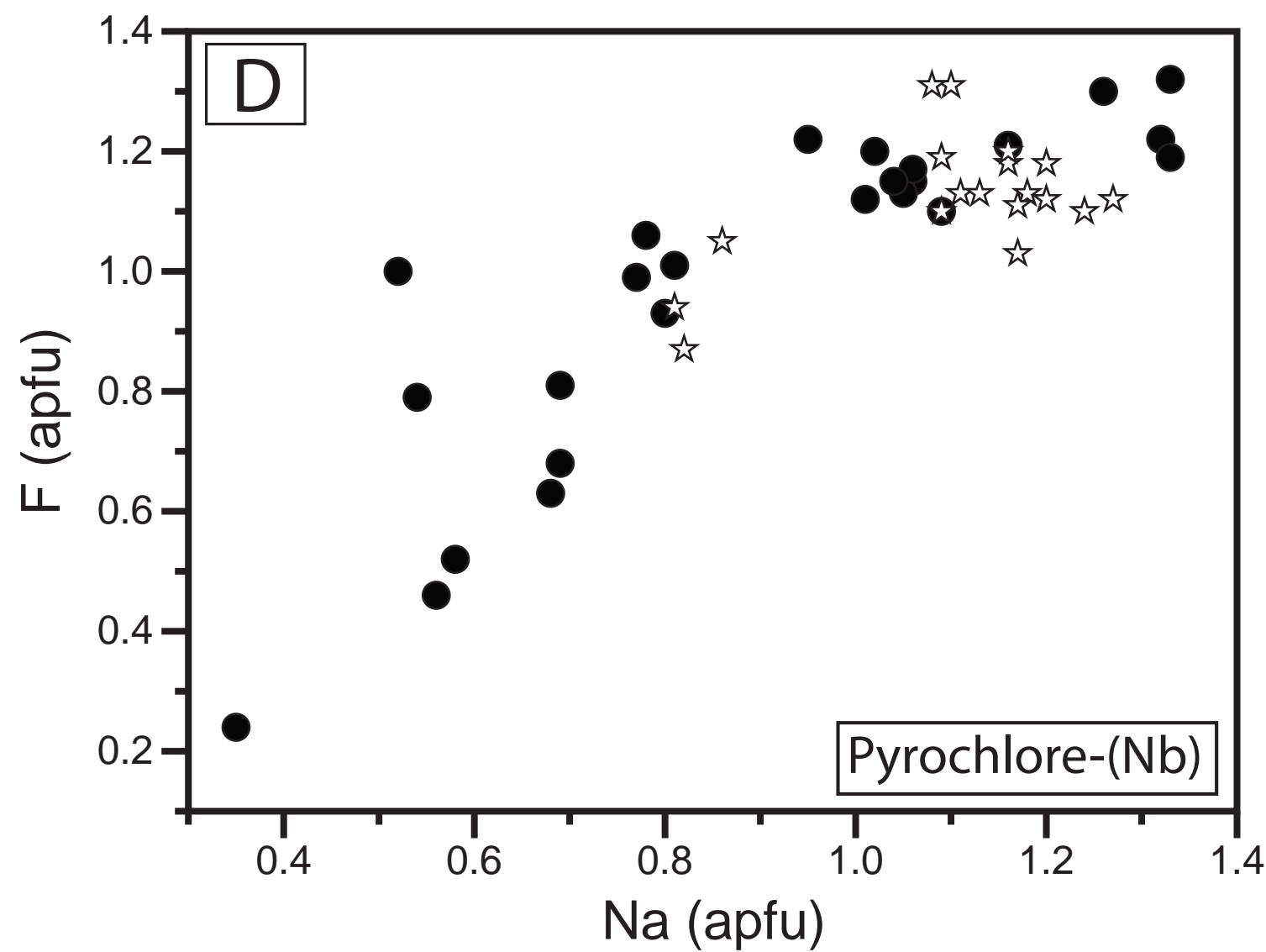
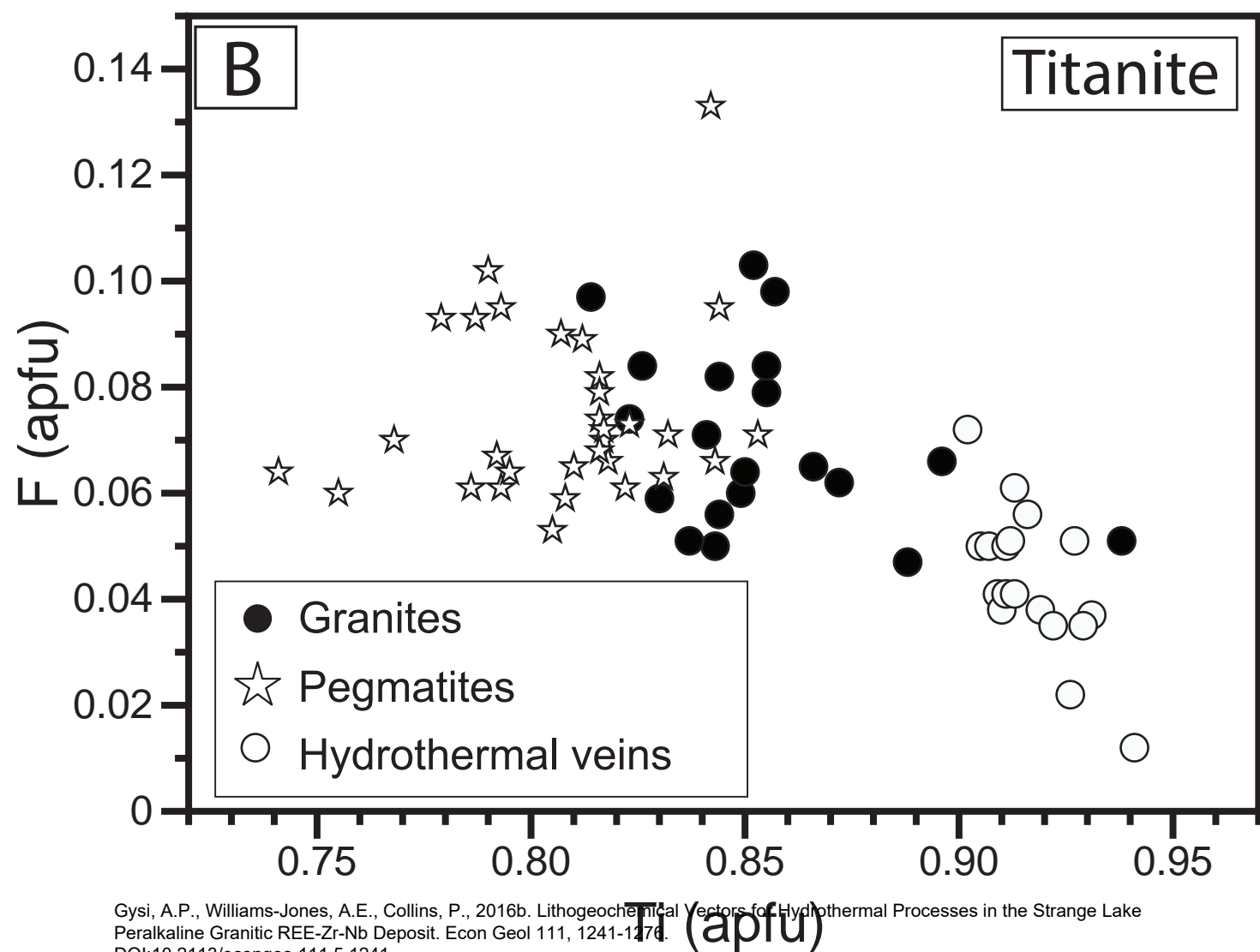
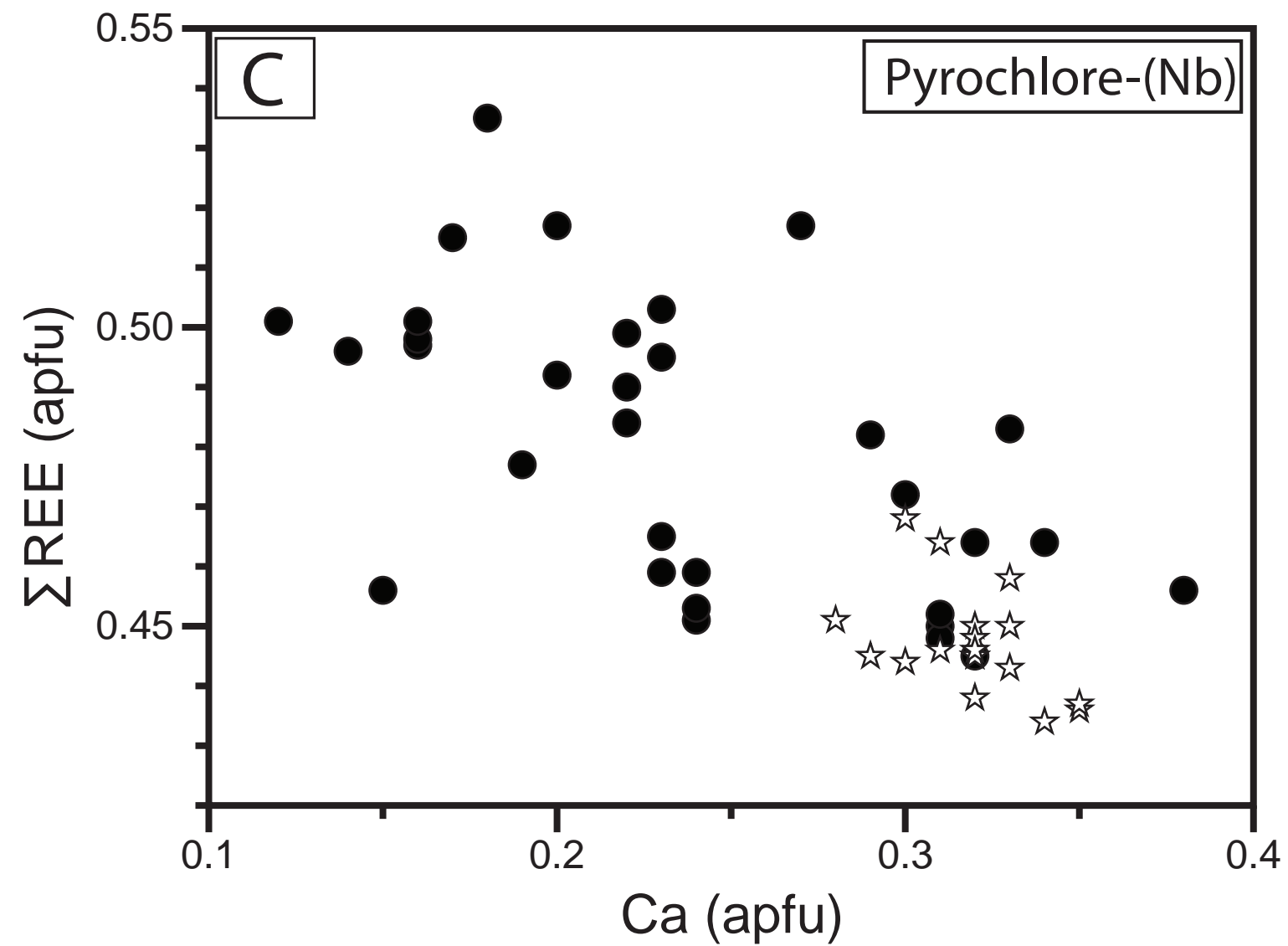
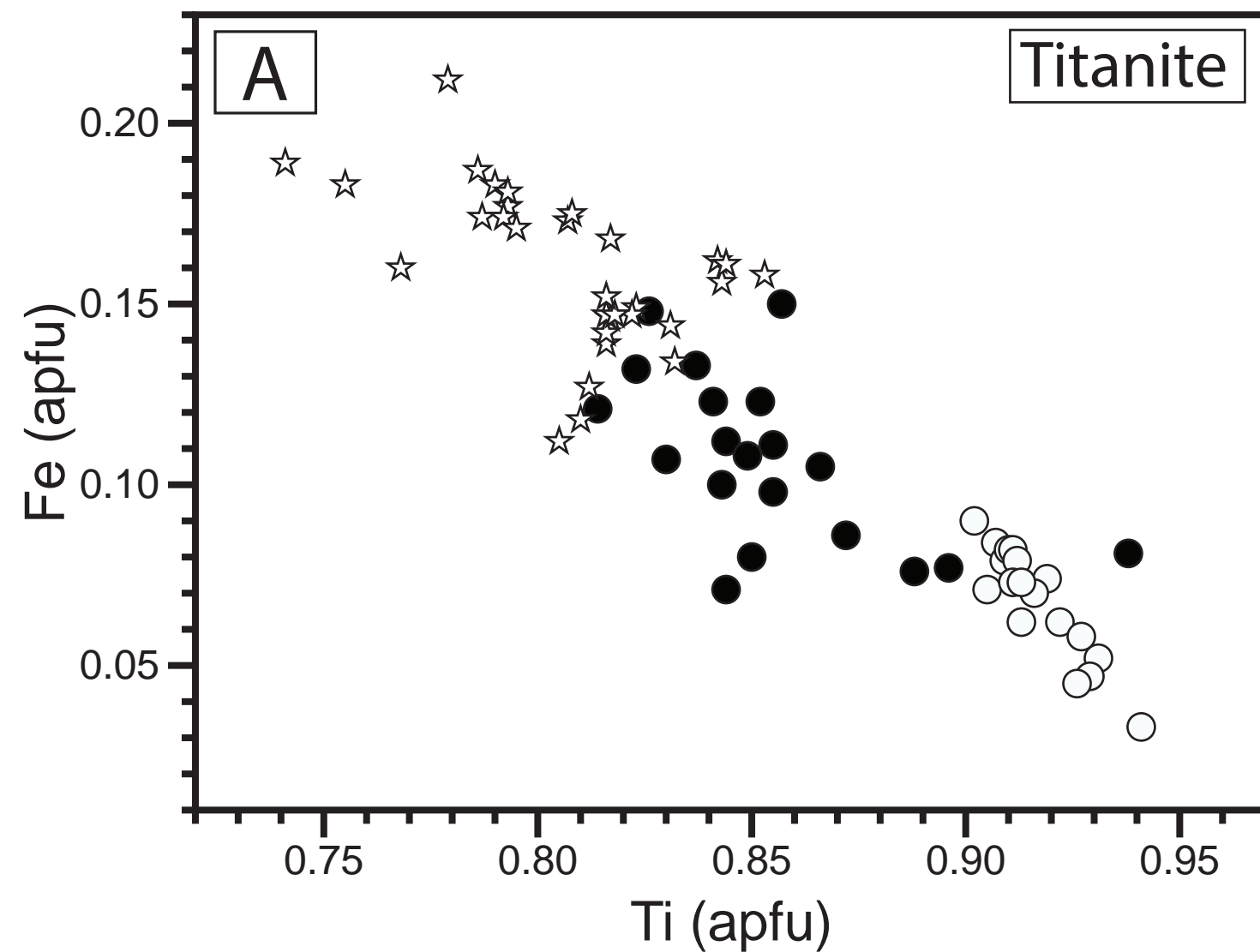
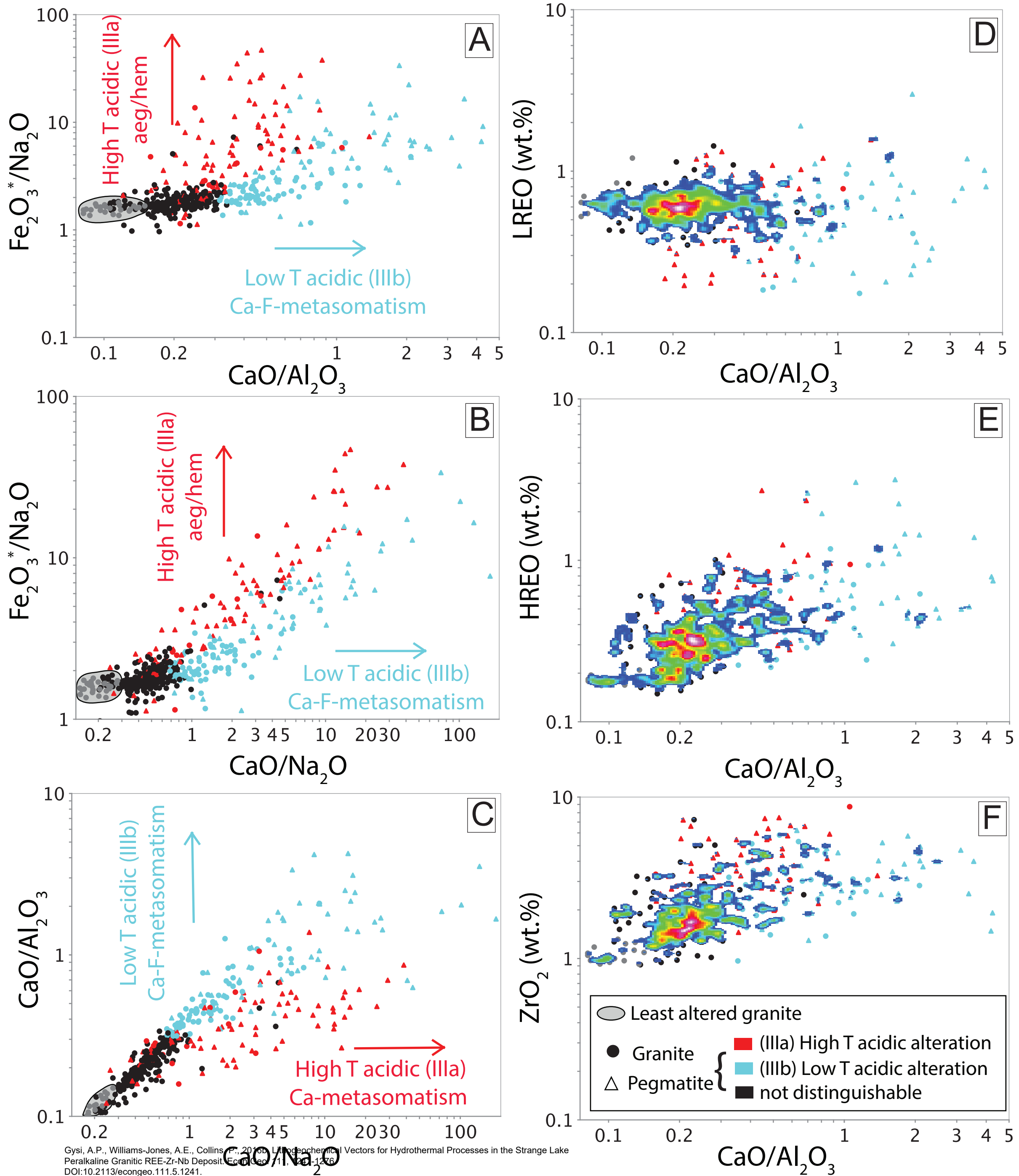


Figure 20



Acidic alteration

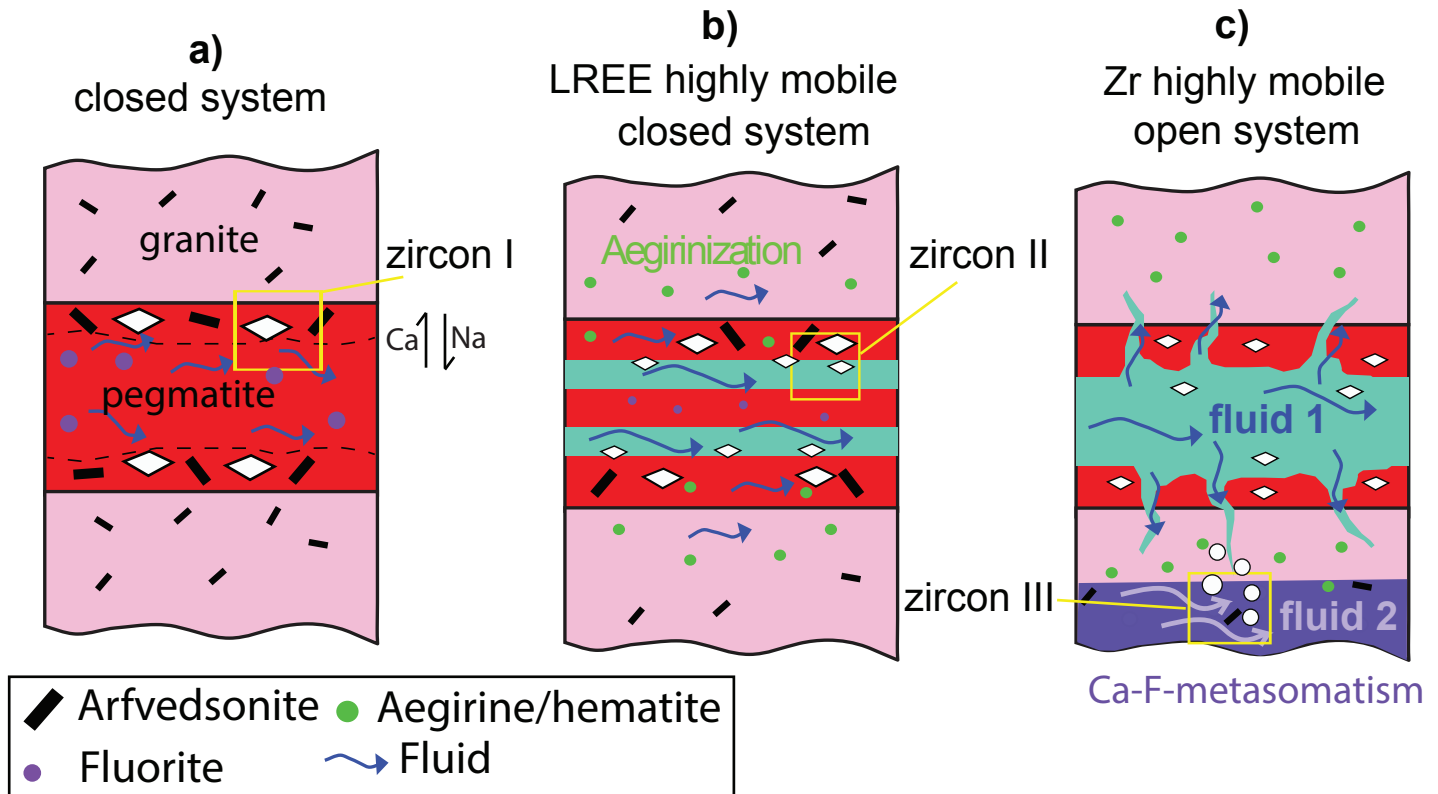
High T alteration (IIIa)

Low T alteration (IIIb)

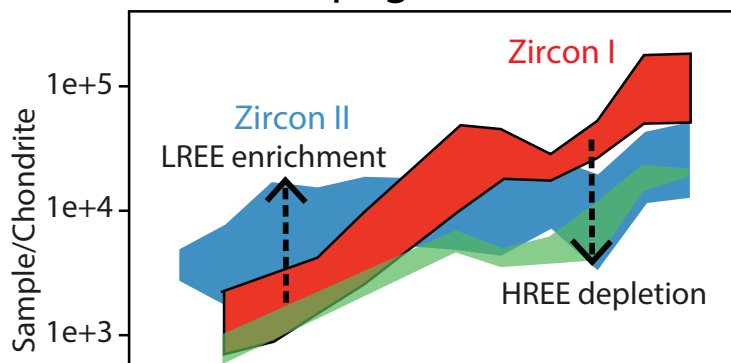
Ca-metasomatism (pseudomorphs)

Ca-F-metasomatism (qtz/fl veins)

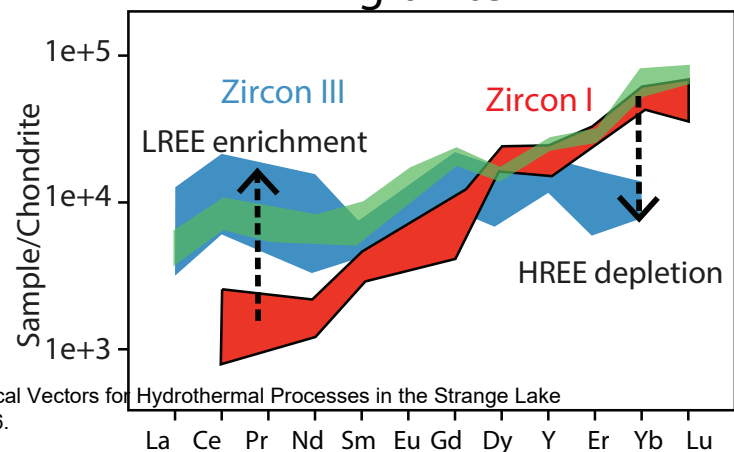
Aegirinization/Hematization



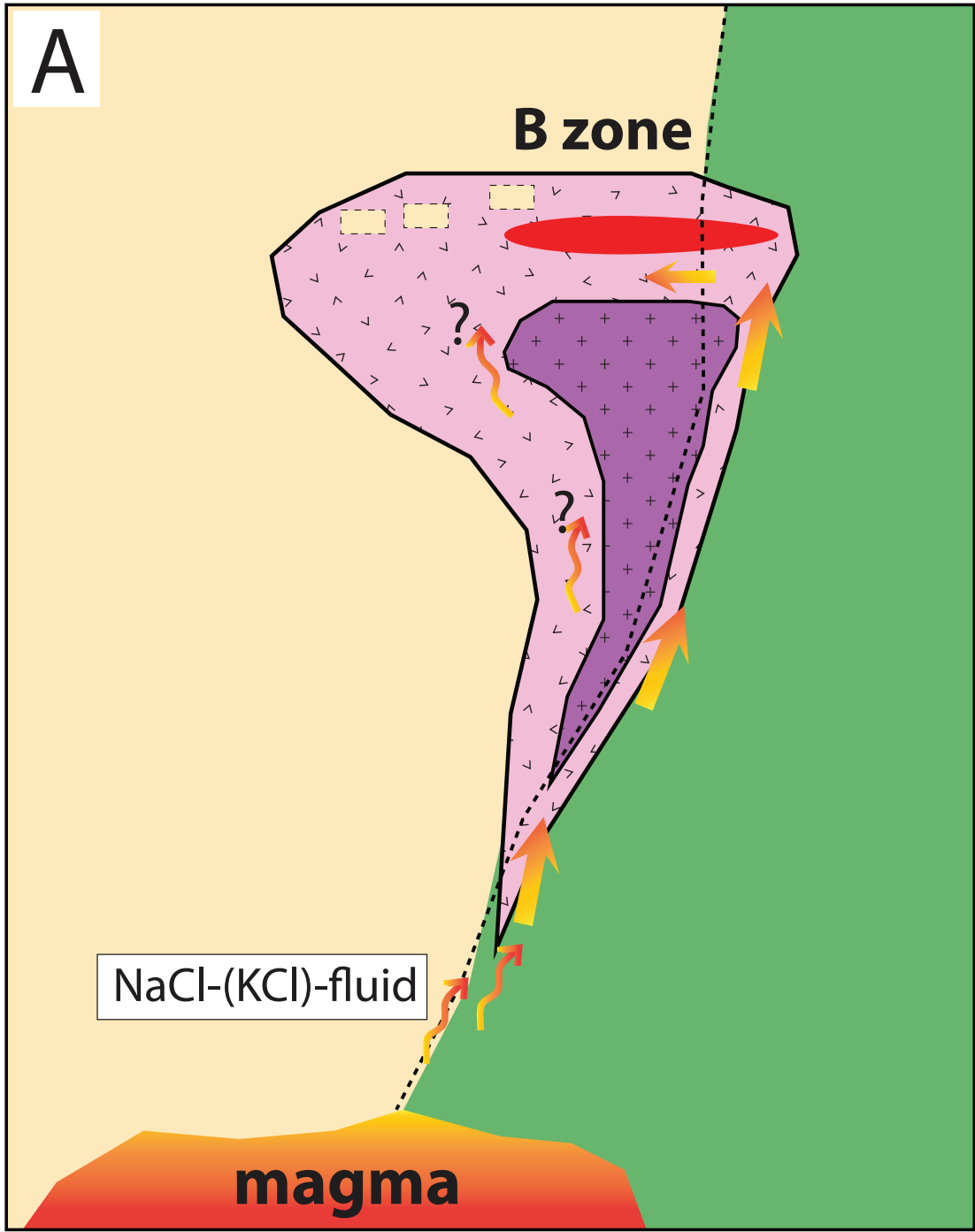
pegmatite



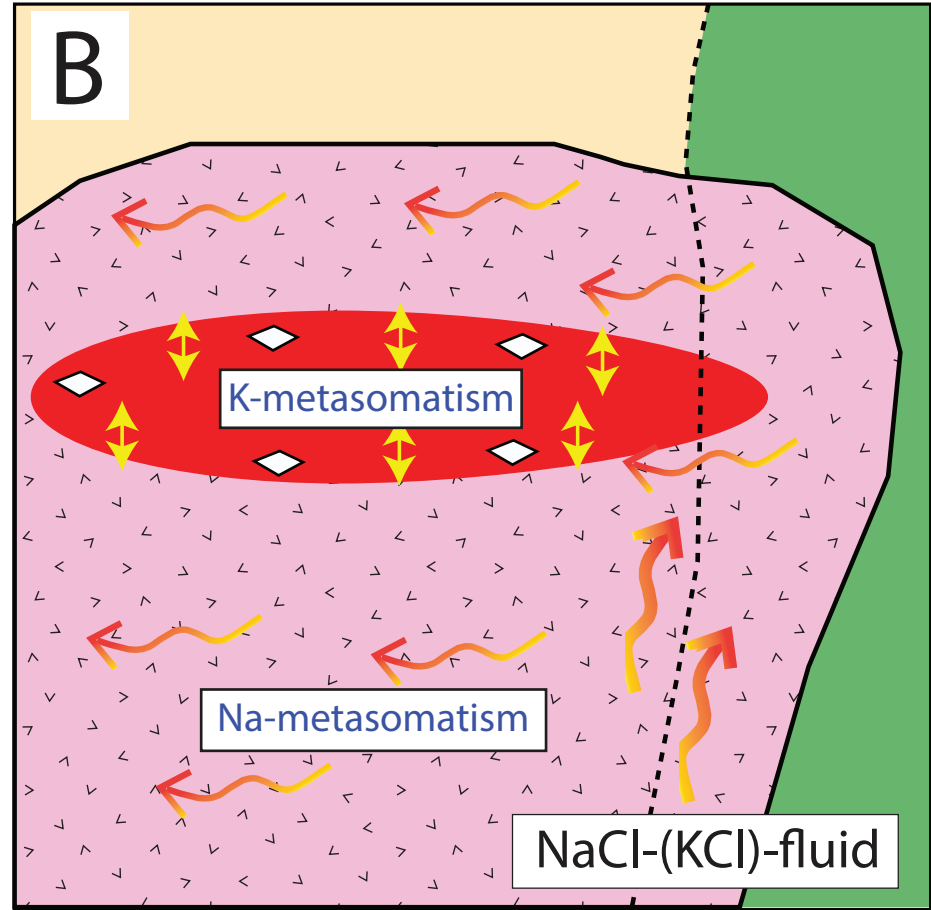
granite



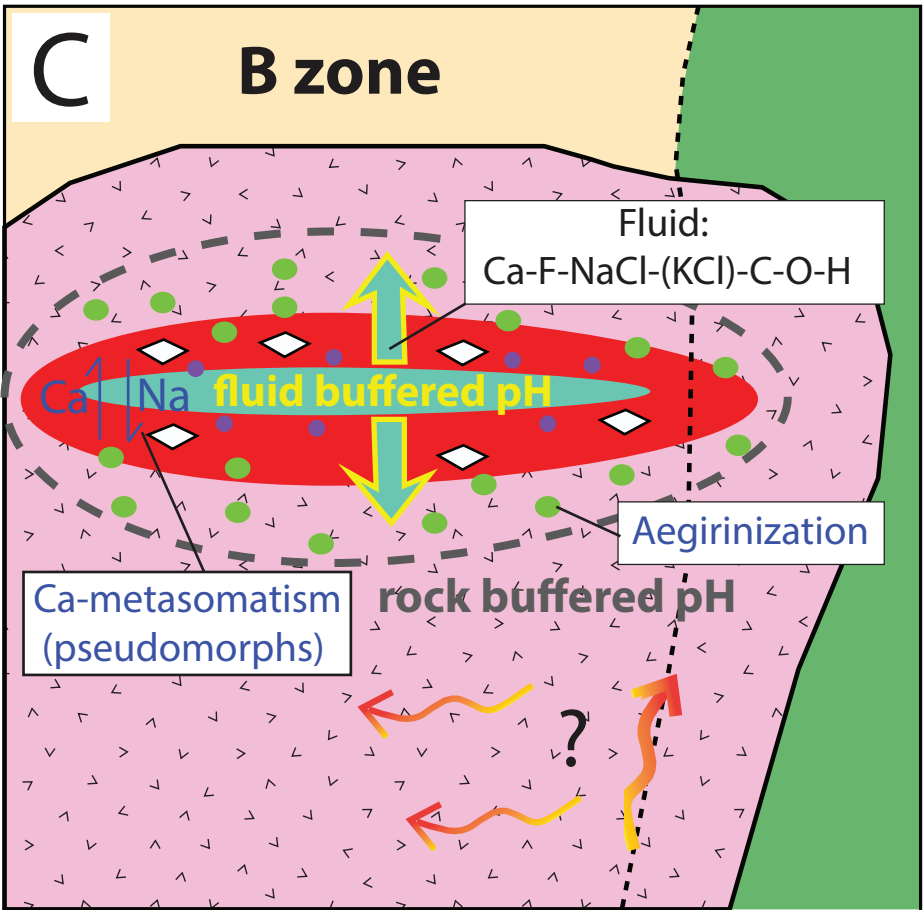
(I) Magmatic stage



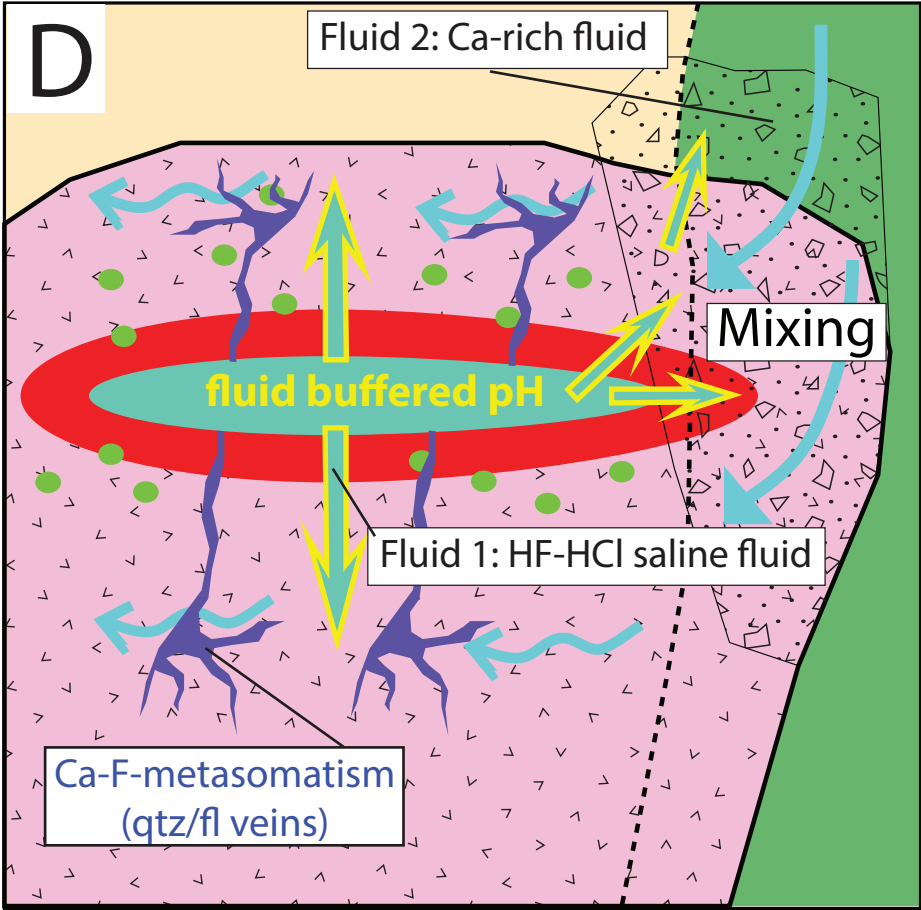
(II) Alkali metasomatism



(IIIa) Acidic alteration high T



(IIIb) Acidic alteration low T



TABLES

TABLE 1. List of REE/HFSE minerals observed at Strange Lake.

	Ideal formulae	Occurrences
REE-bearing minerals		
<i>REE silicates</i>		
Ferrillanite-(Ce)	$\text{Ca}(\text{La,Ce,Nd})\text{AlFe}^{2+}\text{Fe}^{3+}(\text{Si}_2\text{O}_7)(\text{SiO}_4)\text{O}(\text{OH})$	Vein, Gr, Peg
Gadolinite-(Y)	$(\text{Ce,Y})_2\text{Fe}^{2+}\text{Be}_2\text{Si}_2\text{O}_{10}$	Vein, Gr, Peg
Gerenite-(Y)	$(\text{Ca,Na})_2\text{Y}_3\text{Si}_6\text{O}_{18} \cdot 2\text{H}_2\text{O}$	Vein, Peg
Kainosite-(Y)	$\text{Ca}_2\text{Y}_2(\text{SiO}_3)_4(\text{CO}_3) \cdot \text{H}_2\text{O}$	Peg
Cerite-(Ce)	$\text{Ce}_9\text{Fe}(\text{SiO}_4)_6(\text{SiO}_3)(\text{OH})_4$	Gr
<i>REE-F-(CO₂)-minerals</i>		
Fluocerite-(Ce)	$(\text{La,Ce,Nd})\text{F}_3$	Peg
Bastnäsite-(Ce)	$(\text{La,Ce,Nd})\text{CO}_3\text{F}$	Peg
Gagarinite-(Y)	$\text{NaCa}(\text{Y,Ce})\text{F}_6$	Gr
Zr-bearing minerals		
Zircon	ZrSiO_4	Vein, Gr, Peg
Gittinsite	$\text{CaZrSi}_2\text{O}_7$	Vein, Gr, Peg
Elpidite	$\text{Na}_2\text{ZrSi}_6\text{O}_{15} \cdot 3\text{H}_2\text{O}$	Peg
Vlasovite	$\text{Na}_2\text{ZrSi}_4\text{O}_{11}$	Gr
Nb-bearing minerals		
Pyrochlore-(Nb)	$(\text{Ca,Na})_2(\text{Nb,Ta})_2\text{O}_6(\text{OH,F})$	Gr, Peg
Ti-bearing minerals		
Titanite	CaTiSiO_5	Vein, Gr, Peg
Narsarsukite	$\text{Na}_2(\text{Ti,Fe}^{3+})\text{Si}_4\text{O}_{10}(\text{O,F})$	Peg, Gr

Gr: granite; Peg: pegmatite.

TABLE 2. Average EMP analyses (in wt. %) of hydrothermal ferriallanite-(Ce) from Strange Lake granites, pegmatites (Peg) and quartz/fluorite veins. Type corresponds to micro-fractures (f), pore space fillings (p), mineral replacement reactions (rp) and veining (v).

Sample	SL11- 59	2σ	SL11- 62	2σ	SL11- 55	2σ	SL11- 60	2σ	SL11- 155	2σ	SL11- 148	2σ	SL11- 154	2σ	SL11- 158	2σ
Rock	Granite		Granite		Granite		Granite		Granite		Granite		Granite		Granite	
Type	(p)		(p)		(rp)		(p)		(p)		(f)		(rp)		(rp)	
Nr.	3		5		10		10		15		10		22		26	
SiO ₂	31.7	0.7	33.9	0.8	33.0	0.6	32.8	0.7	33.4	1.0	32.6	0.6	33.1	1.9	34.5	1.1
Al ₂ O ₃	11.2	0.6	12.9	2.7	11.5	1.2	11.7	1.6	11.2	2.7	13.8	1.2	11.6	2.5	12.5	1.7
TiO ₂	d.l.		0.11	0.12	0.20	0.19	0.23	0.33	0.33	0.54	0.53	0.30	0.37	0.63	0.25	0.21
FeO	20.7	0.4	18.1	3.1	19.6	2.6	20.9	1.8	21.4	3.5	13.7	1.2	19.7	3.2	16.8	4.1
MnO	0.29	0.08	0.52	0.31	0.59	0.40	0.27	0.22	0.37	0.24	0.91	0.34	0.44	0.45	2.20	1.67
CaO	13.4	0.3	15.0	2.0	13.6	1.7	14.3	1.9	15.0	1.6	12.2	1.3	14.7	4.2	14.5	3.0
Na ₂ O	d.l.		d.l.		d.l.		d.l.		d.l.		d.l.		d.l.		0.60	0.50
F	d.l.		d.l.		d.l.		0.55		0.10	0.04	0.21	0.07	0.13	0.04	0.14	0.08
Y ₂ O ₃	d.l.		d.l.		d.l.		0.32		0.23	0.14			0.24	0.22	0.13	0.16
La ₂ O ₃	6.69	1.45	7.43	2.48	7.92	4.25	5.17	1.31	3.95	1.15	7.34	4.38	4.21	2.95	4.36	2.22
Ce ₂ O ₃	8.66	1.01	6.57	1.50	8.28	1.51	8.21	2.03	8.25	1.89	11.6	1.9	8.27	5.45	8.57	3.22
Pr ₂ O ₃	0.57	0.22	0.24	0.16	0.45	0.24	0.68	0.26	0.60	0.13	0.90	0.60	0.62	0.31	0.84	0.25
Nd ₂ O ₃	1.96	0.68	0.41	0.22	1.01	1.12	1.76	0.92	1.74	0.40	1.54	1.38	2.01	0.76	1.81	0.40
Sm ₂ O ₃	d.l.		d.l.		d.l.		d.l.		0.12	0.03	d.l.		0.19	0.16	0.12	0.03
Eu ₂ O ₃	0.27	0.03	d.l.		0.44	0.06	d.l.		d.l.		d.l.		d.l.		0.13	0.11
Gd ₂ O ₃	d.l.		d.l.		d.l.		d.l.		0.10	0.03	d.l.		0.16	0.09	d.l.	
Total	95.4		95.3		96.2		96.1		96.5		95.3		95.8		96.6	
¹ Fe ³⁺ /Fe ³⁺ +Fe ²⁺	0.64		0.71		0.67		0.69		0.73		0.52		0.70		0.71	
² REE ³⁺ +Fe ²⁺ +Mn ²⁺	1.240		0.899		1.130		1.038		0.948		1.296		0.996		1.014	
² Ca ²⁺ +Fe ³⁺ +Al ³⁺	2.657		2.724		2.543		2.772		2.800		2.248		2.712		2.509	
² sumREE	0.628		0.476		0.589		0.531		0.488		0.721		0.524		0.501	
² Al ³⁺	1.250		1.347		1.230		1.261		1.184		1.495		1.235		1.283	

The uncertainties (2σ) represent the standard deviation of average mineral analyses with Nr. representing the number of analyzed mineral spots per thin section; (d.l.) below detection limit. The concentrations of K, Dy, Er, and Yb not reported here were all below detection limit.

¹Fe³⁺ and Fe²⁺ calculated based on the method by Petrik et al. (1995). ² apfu calculated from mineral formulae based on 3 Si.

TABLE 2. (Continued)

Sample	SL11- 58	2σ	SL12- 47	2σ	SL12- 49	2σ	SL11- 65	2σ	SL11- 111	2σ	SL11- 97	2σ	SL11- 100	2σ	SL11- 106	2σ
Rock	Granite		Qtz/Fl vein		Qtz/Fl vein		Granite		Peg		Peg		Peg		Peg	
Type	(f)		(v)		(v)		(p)		(p)		(f)		(f)		(rp)	
Nr.	18		12		7		5		3		5		9		3	
SiO ₂	33.7	0.7	33.8	1.0	33.3	0.8	33.2	0.4	32.4	0.0	33.0	0.4	33.4	0.7	33.5	1.8
Al ₂ O ₃	11.6	1.7	15.7	2.5	13.5	2.4	9.8	1.3	9.2	0.3	11.5	1.6	10.0	1.6	12.1	2.4
TiO ₂	0.13	0.12	0.20	0.44	0.33	0.56	0.42	0.38	0.06	0.04	0.07	0.04	0.30	0.26	0.24	0.58
FeO	21.7	2.1	15.6	2.3	17.1	1.6	21.9	3.2	22.0	0.6	19.9	1.1	21.5	2.6	20.4	3.2
MnO	0.37	0.14	0.29	0.18	0.60	0.15	0.23	0.05	0.48	0.13	1.23	0.19	1.53	0.53	0.77	0.47
CaO	15.0	1.4	13.5	1.7	14.1	1.7	13.4	2.1	15.1	0.2	14.8	2.3	15.5	1.7	15.3	3.1
Na ₂ O	d.l.		d.l.		d.l.		0.17	0.08	d.l.		d.l.		d.l.		d.l.	
F	d.l.		d.l.		d.l.		d.l.		d.l.		d.l.		0.11		d.l.	
Y ₂ O ₃	0.27	0.17	0.13	0.07	0.16	0.12	0.37	0.22	d.l.		d.l.		0.73	0.07	0.12	0.02
La ₂ O ₃	4.79	1.96	7.44	3.48	10.5	3.8	3.42	1.40	2.23	0.26	9.33	2.57	3.60	1.36	4.91	3.66
Ce ₂ O ₃	6.74	1.07	8.98	0.86	5.43	1.09	8.71	1.78	9.21	0.33	4.58	1.78	7.66	1.89	7.37	2.40
Pr ₂ O ₃	0.62	0.20	0.56	0.22	0.23	0.10	0.95	0.21	1.01	0.05	0.16	0.05	0.52	0.08	0.52	0.12
Nd ₂ O ₃	1.88	0.62	1.09	0.69	0.32	0.27	3.00	0.50	2.28	0.06	0.63	0.15	1.48	0.17	1.28	0.45
Sm ₂ O ₃	0.17	0.12	d.l.		d.l.		0.37	0.17	d.l.		d.l.		d.l.		d.l.	
Eu ₂ O ₃	0.12	0.04	0.14	0.04	0.15	0.06	d.l.		d.l.		d.l.		0.11	0.05	d.l.	
Gd ₂ O ₃	0.15	0.09	d.l.		d.l.		0.28	0.11	d.l.		d.l.		0.17	0.02	d.l.	
Total	97.2		97.5		95.5		96.1		94.0		95.0		95.8		96.5	
¹ Fe ³⁺ /Fe ³⁺ +Fe ²⁺	0.73		0.57		0.65		0.71		0.75		0.72		0.77		0.73	
² REE ³⁺ +Fe ²⁺ +Mn ²⁺	0.944		1.096		1.056		1.063		0.960		1.003		0.936		0.938	
² Ca ²⁺ +Fe ³⁺ +Al ³⁺	2.830		2.612		2.622		2.514		2.782		2.759		2.803		2.856	
² sumREE	0.481		0.578		0.554		0.568		0.497		0.491		0.448		0.467	
² Al ³⁺	1.215		1.649		1.434		1.040		1.006		1.228		1.057		1.279	

TABLE 2. (Continued)

Sample	SL11-104	2σ	SL11-170b	2σ	SL11-146	2σ
Rock	Peg		Peg		Peg	
Type	(rp)		(rp)		(p)	
Nr.	5		15		18	
SiO ₂	34.4	0.9	34.7	1.1	33.9	0.9
Al ₂ O ₃	12.9	3.6	12.7	3.2	12.7	1.5
TiO ₂	0.15	0.31	0.04	0.01	0.12	0.19
FeO	20.6	5.1	17.5	4.1	17.1	2.6
MnO	0.74	0.55	1.73	0.79	1.41	0.80
CaO	16.9	1.6	15.5	1.7	13.4	2.4
Na ₂ O	d.l.		d.l.		d.l.	
F	d.l.		0.13	0.05	0.15	0.10
Y ₂ O ₃	0.13		0.17	0.20	d.l.	
La ₂ O ₃	2.82	1.31	4.06	1.39	6.66	4.17
Ce ₂ O ₃	5.57	1.08	7.82	2.13	9.38	2.16
Pr ₂ O ₃	0.49	0.14	0.62	0.18	0.97	0.21
Nd ₂ O ₃	1.60	0.57	1.26	0.31	2.13	1.34
Sm ₂ O ₃	0.15	0.15	0.08	0.03	0.13	0.09
Eu ₂ O ₃	d.l.		0.08	0.02	d.l.	
Gd ₂ O ₃	d.l.		0.10	0.03	d.l.	
Total	96.3		96.1		97.9	
¹ Fe ³⁺ /Fe ³⁺ +Fe ²⁺	0.79		0.74		0.63	
² REE ³⁺ +Fe ²⁺ +Mn ²⁺	0.696		0.893		1.194	
² Ca ²⁺ +Fe ³⁺ +Al ³⁺	3.108		2.666		2.393	
² sumREE	0.338		0.442		0.622	
² Al ³⁺	1.325		1.290		1.326	

TABLE 3. Average EMP analyses (in wt. %) of hydrothermal gadolinite-group minerals from Strange Lake granites and pegmatites (Peg). Group corresponds to REE profiles in Fig. 16.

	SL11-151	2σ	SL11-158	2σ	SL11-58a	2σ	SL11-58b	2σ	SL11-111a	2σ	SL11-111b	2σ	SL-11-105	2σ
Rock	Granite		Granite		Granite		Granite		Peg		Peg		Peg	
Group	LREE		MREE		MREE		MREE		LREE		HREE		LREE	
Nr.	6		9		13		7		9		11		4	
SiO ₂	31.3	0.4	32.2	1.5	32.3	1.1	32.2	1.0	30.6	1.6	32.7	1.3	30.3	0.6
TiO ₂	d.l.		0.04	0.01	0.34	0.09	0.32	0.09	d.l.		0.06	0.03	0.08	0.01
Al ₂ O ₃	0.13	0.22	0.62	0.95	0.19	0.34	0.12	0.09	0.29	0.19	0.06	0.03	0.30	0.66
FeO	0.92	0.19	0.64	0.28	1.36	0.21	2.19	0.55	1.25	4.61	0.60	0.17	2.65	1.06
MnO	0.83	0.06	0.64	0.12	0.09	0.03	0.16	0.08	1.09	0.30	0.59	0.23	0.70	0.06
CaO	8.79	0.41	8.20	0.81	5.52	1.19	9.09	2.33	5.13	2.17	4.23	0.56	7.84	1.14
Na ₂ O	0.13	0.03	0.21	0.05	1.28	0.34	0.56	0.36	0.63	0.34	0.88	0.16	0.23	0.10
F	0.41	0.13	0.26	0.11	0.41	0.12	0.30	0.08	0.61	1.09	0.28	0.11	0.39	0.06
Y ₂ O ₃	1.47	0.39	24.0	2.3	5.80	2.27	10.9	5.2	1.96	2.82	29.6	6.2	2.95	1.46
La ₂ O ₃	7.33	0.59	0.19	0.10	6.68	1.08	3.20	2.67	9.78	2.09	0.46	0.35	9.27	1.42
Ce ₂ O ₃	18.2	2.0	1.43	0.69	15.3	2.3	8.72	5.38	21.9	3.3	1.32	0.98	18.5	1.7
Pr ₂ O ₃	2.79	0.31	0.49	0.22	1.90	0.25	1.27	0.55	2.39	0.66	0.18	0.14	2.11	0.43
Nd ₂ O ₃	10.2	0.3	2.62	0.84	7.43	0.77	5.81	2.00	8.03	2.40	0.86	0.87	8.02	1.98
Sm ₂ O ₃	1.87	0.44	0.89	0.09	1.63	0.19	1.75	0.38	1.02	0.28	0.21	0.11	0.92	0.41
Eu ₂ O ₃	d.l.		d.l.		d.l.		0.22	0.08	d.l.		0.21	0.09	d.l.	
Gd ₂ O ₃	1.34	0.32	3.26	0.18	2.12	0.38	3.01	0.34	1.18	0.44	3.95	1.99	0.55	0.27
Dy ₂ O ₃	0.45	0.11	3.28	0.28	1.10	0.20	1.93	0.75	0.37	0.23	6.47	2.34	0.36	0.16
Er ₂ O ₃	0.09	0.05	1.89	0.14	0.26	0.12	0.64	0.36	0.20	0.20	2.36	0.24	0.20	0.08
Yb ₂ O ₃	0.04		1.40	0.17	0.11	0.08	0.22	0.19	0.09	0.07	0.27	0.26	0.25	0.46
Total	86.3		82.2		83.9		82.6		86.5		85.1		85.3	
¹ Si (apfu)	2.000		2.000		2.000		2.000		2.000		2.000		2.000	
¹ Σ REE	1.027		1.116		1.005		0.946		1.128		1.287		1.068	
¹ Ca	0.602		0.547		0.366		0.604		0.361		0.277		0.555	

The uncertainties (2σ) represent the standard deviation of average mineral analyses with Nr. representing the number of analyzed mineral spots per thin section; (d.l.) below detection limit. The concentrations of K and Lu not reported here were all below detection limit. ¹ apfu calculated from mineral formulae based on 2 Si.

TABLE 3. (Continued)

	SL-11- 100	2σ	SL-11- 104	2σ	SL-11- 170a	2σ	SL-11-170b	2σ	SL12- 44	2σ
Rock	Peg		Peg		Peg		Peg		Peg	
Group	MREE		HREE		HREE		MREE		HREE	
Nr.	7		3		10		8		19	
SiO ₂	32.5	0.9	31.7	0.4	31.8	2.0	31.6	1.6	33.6	3.5
TiO ₂	0.78	0.21	0.58	0.28	0.20	0.08	0.10	0.04	0.10	0.05
Al ₂ O ₃	0.09	0.12	d.l.		0.10	0.07	0.12	0.05	0.07	0.06
FeO	1.03	0.52	0.91	0.51	3.63	5.63	2.70	3.45	3.95	8.85
MnO	0.73	0.10	0.61	0.09	0.45	0.06	0.51	0.06	0.55	0.10
CaO	6.50	1.45	6.95	1.64	8.37	2.75	8.62	3.00	9.42	4.02
Na ₂ O	0.62	0.20	0.48	0.14	0.44	0.18	0.47	0.19	0.51	0.31
F	0.27	0.09	0.19	0.07	0.22	0.09	0.35	0.05	0.29	0.16
Y ₂ O ₃	17.0	2.0	20.8	3.3	20.9	4.0	14.0	1.7	23.4	5.1
La ₂ O ₃	0.61	0.37	0.99	0.20	0.48	0.21	0.46	0.19	0.35	0.25
Ce ₂ O ₃	3.05	1.44	4.73	2.62	2.91	1.11	2.94	0.65	1.08	0.42
Pr ₂ O ₃	0.92	0.34	0.83	0.42	0.60	0.19	0.81	0.14	0.20	0.11
Nd ₂ O ₃	6.72	1.63	4.37	1.41	3.17	0.68	4.51	0.64	0.96	0.43
Sm ₂ O ₃	3.29	0.56	1.41	0.42	1.31	0.32	2.83	0.34	0.33	0.24
Eu ₂ O ₃	d.l.		d.l.		d.l.		d.l.		d.l.	
Gd ₂ O ₃	5.54	0.60	3.82	0.76	3.50	0.51	6.43	0.97	2.55	0.50
Dy ₂ O ₃	3.72	0.43	3.79	1.32	3.33	0.45	4.87	1.61	2.78	0.68
Er ₂ O ₃	1.23	0.18	2.07	0.26	1.25	0.14	1.21	0.40	1.65	0.25
Yb ₂ O ₃	0.20	0.11	0.65	0.21	0.70	0.18	0.29	0.06	1.20	0.12
Total	84.8		84.9		83.4		82.7		83.0	
¹ Si (apfu)	2.000		2.000		2.000		2.000		2.000	
¹ Σ REE	1.091		1.191		1.071		0.996		0.960	
¹ Ca	0.428		0.471		0.564		0.584		0.600	

TABLE 4. Average EMP analyses (in wt. %) of Ca- and Na-zirconosilicates from Strange Lake granites and pegmatites (Peg).

	SL11- 55	2σ	SL11- 59	2σ	SL11- 62	2σ	SL11- 98	2σ	SL11- 104	2σ	SL11- 106	2σ	SL11- 195	2σ	SL11- 17	2σ	SL11- 80	2σ
Rock	Granite		Granite		Granite		Granite		Peg		Peg		Peg		Peg		Granite	
Mineral	Git		Git		Git		Git		Git		Git		Git		Arm		Vla	
Nr.	3		2		2		8		17		6		5		3		29	
SiO ₂	40.9	0.7	37.2	2.0	38.9	0.4	38.1	1.9	38.8	3.1	39.1	4.3	40.2	1.6	60.0	7.4	55.3	0.5
TiO ₂	d.l.		d.l.		d.l.		0.05	0.02	0.03	0.03	0.09	0.15	0.08	0.10	0.12	0.07	d.l.	
Al ₂ O ₃	d.l.	d.l.	d.l.	d.l.	0.16	-	0.10	0.11	0.08	0.04	0.19	0.29	0.16	0.27	0.70	0.20	d.l.	
FeO	0.12	0.21	3.99	4.05	0.80	0.16	0.26	0.60	0.20	0.15	0.24	0.23	0.49	0.52	0.16	0.03	0.03	0.06
MnO	0.16	0.09	0.30	0.05			0.87	0.20	0.78	0.15	1.04	0.19	0.35	0.29	0.06	0.01	d.l.	
CaO	19.0	0.3	17.6	1.0	18.4	0.1	16.3	1.6	17.2	1.4	17.0	1.7	18.3	0.3	7.26	1.95	d.l.	
Na ₂ O	d.l.		d.l.		d.l.		d.l.		d.l.		d.l.		d.l.		d.l.		13.6	2.1
K ₂ O	d.l.		d.l.		d.l.		d.l.		d.l.		d.l.		d.l.		d.l.		0.11	0.18
P ₂ O ₅	d.l.		d.l.		d.l.		0.04	-	d.l.		0.06	-	d.l.		0.05	-	d.l.	
F	d.l.		d.l.		d.l.		0.15	0.09	0.12	0.06	0.06	0.11	0.11	0.04	4.94	0.94	0.16	0.11
HfO ₂	1.06	0.20	0.99	0.11	1.23	0.51	1.21	0.29	0.88	0.14	0.90	0.17	1.22	0.22	0.44	0.07	0.69	0.24
ZrO ₂	39.8	0.5	37.4	0.8	38.0	1.5	37.0	0.8	36.3	3.6	35.6	4.3	37.8	1.6	19.0	2.9	27.7	1.0
Nb ₂ O ₅	0.11		0.11				0.24	0.26	0.14	0.07	0.46	1.38	0.17	0.13	0.89	0.36	d.l.	
Y ₂ O ₃	d.l.		0.13	0.01	0.13	-	0.72	1.09	0.11	0.05	0.23	0.21	0.14	-	1.42	0.70	d.l.	
La ₂ O ₃	d.l.		d.l.		d.l.		d.l.		0.07	0.02	0.06	-	d.l.		d.l.		d.l.	
Ce ₂ O ₃	d.l.		d.l.		d.l.		0.14	0.23	0.06	0.04	0.19	0.17	d.l.		0.15	0.06	d.l.	
Nd ₂ O ₃	d.l.		d.l.		d.l.		d.l.		d.l.		0.05	0.06	d.l.		0.13	0.04	d.l.	
Sm ₂ O ₃	d.l.		d.l.		d.l.		d.l.		d.l.		d.l.		d.l.		0.08	0.02	d.l.	
Eu ₂ O ₃	d.l.		d.l.		d.l.		0.06	-	0.07	0.02	0.09	0.03	d.l.		d.l.		d.l.	
Gd ₂ O ₃	d.l.		d.l.		d.l.		d.l.		d.l.		d.l.		d.l.		0.17	0.11	d.l.	
Dy ₂ O ₃	d.l.		d.l.		d.l.		0.13	0.15	d.l.		d.l.		d.l.		0.36	0.11	d.l.	
Er ₂ O ₃	d.l.		d.l.		d.l.		0.16	0.16	0.05	-	0.05	0.00	d.l.		0.22	0.09	d.l.	
Yb ₂ O ₃	d.l.		0.18	0.08	d.l.		0.31	0.27	0.19	0.03	0.20	0.06	d.l.		0.25	0.08	d.l.	
Lu ₂ O ₃	d.l.		0.07		d.l.		0.07	0.03	0.06	0.02	0.06	0.01	d.l.		d.l.		d.l.	
Total	101.2		97.9		97.6		95.9		95.1		95.7		99.1		96.4		97.5	

The uncertainties (2σ) represent the standard deviation of average mineral analyses with Nr. representing the number of analyzed mineral spots per thin section; (d.l.) below detection limit. The concentrations of Pr not reported here were all below detection limit.

TABLE 5. Average EMP analyses (in wt. %) of zircon from Strange Lake granites and pegmatites (Peg). Groups correspond to Zircon I-III and zircons with intermediate (Inter.) chondrite-normalized REE profiles.

	SL11-119	2 σ	SL11-55	2 σ	SL11-59	2 σ	SL11-62	2 σ	SL11-62	2 σ	SL11-60	2 σ	SL11-60	2 σ	SL11-30	2 σ
Rock	Granite		Granite		Granite		Granite		Granite		Granite		Granite		Granite	
Mineral	Zrn		Zrn		Zrn		Zrn-core		Zrn-rim		Zrn-core		Zrn-rim		Zrn	
Group	I		III		Inter.		III		III		III		III		I	
Nr	12		3		5		7		3		8		3		15	
SiO ₂	29.1	0.9	32.8	0.3	29.6	0.7	32.0	1.0	31.8	0.7	30.8	3.2	31.8	0.7	31.4	1.7
TiO ₂	0.05	0.04	0.13	0.01	0.07	0.01	d.l.		d.l.		d.l.		d.l.		0.09	0.02
Al ₂ O ₃	0.09	0.08	0.54	0.09	0.58	0.12	0.73	0.42	0.65	0.21	0.71	0.17	0.45	0.65	0.07	0.02
FeO	0.80	0.59	0.67	0.14	0.87	0.09	1.12	0.86	0.63	0.50	0.48	0.15	0.44	0.72	0.38	0.31
MnO	0.37	0.19	0.07	0.01	0.14	0.02	d.l.		d.l.		d.l.		d.l.		0.09	0.04
CaO	2.03	0.76	0.73	0.14	1.42	0.49	0.81	0.41	1.33	0.63	0.72	0.38	0.62	0.44	0.14	0.14
Na ₂ O	0.29	0.08	d.l.		0.30	0.13	0.13	0.08	0.09	0.05	0.10	0.03	d.l.		0.17	0.21
P ₂ O ₅	0.39	0.16	0.07	-	d.l.		d.l.		d.l.		d.l.		d.l.		d.l.	
F	0.28	0.13	0.15	0.05	0.18	0.05	0.19	0.10	0.17	0.06	0.14	0.08	0.13	0.05	0.32	0.30
HfO ₂	1.09	0.29	1.62	0.18	1.36	0.23	1.58	0.24	1.32	0.29	1.51	0.17	1.47	0.11	1.70	0.77
ZrO ₂	51.7	1.7	55.8	1.5	49.5	3.1	54.4	2.0	54.1	3.9	54.3	7.4	56.2	2.3	64.9	1.7
Nb ₂ O ₅	0.33	0.15	0.54	0.13	0.66	0.28	0.31	0.09	0.29	0.18	0.31	0.20	0.27	0.29	0.13	0.03
Y ₂ O ₃	3.74	1.08	3.41	0.31	4.87	1.08	3.41	0.70	3.43	1.39	2.72	0.79	3.57	1.15	0.22	0.15
La ₂ O ₃	d.l.		0.11		0.13	0.06	0.13	0.06	0.18	0.20	0.13	0.04	0.24	0.20	d.l.	
Ce ₂ O ₃	0.10	0.08	0.56	0.05	0.71	0.09	0.66	0.23	0.83	0.56	0.50	0.13	1.05	0.90	0.07	0.02
Pr ₂ O ₃	d.l.		d.l.		0.06	0.01	0.11		0.12		0.10		0.15	0.09	d.l.	
Nd ₂ O ₃	0.09	0.03	0.33	0.02	0.39	0.11	0.25	0.09	0.47	0.33	0.25	0.08	0.60	0.39	d.l.	
Sm ₂ O ₃	0.07	0.02	0.08	0.03	0.12	0.07	d.l.		0.12	0.02	0.10	0.03	0.12	-	d.l.	
Eu ₂ O ₃	d.l.		d.l.		0.12		d.l.		d.l.		d.l.		d.l.		d.l.	
Gd ₂ O ₃	0.17	0.09	0.24	0.07	0.48	0.12	0.30	0.08	0.38	0.25	0.28	0.07	0.29	0.03	d.l.	
Dy ₂ O ₃	0.54	0.16	0.23	0.07	0.43	0.07	0.34	0.11	0.40	0.19	0.25	0.12	0.30	0.15	d.l.	
Er ₂ O ₃	0.56	0.05	0.21	0.04	0.50	0.10	0.29	0.06	0.25	0.14	0.14	0.06	0.17	0.05	d.l.	
Yb ₂ O ₃	1.05	0.22	0.17	0.06	1.25	0.36	0.22	0.09	0.17	0.09	d.l.		d.l.		d.l.	
Lu ₂ O ₃	0.14	0.05	d.l.		0.21	0.05	d.l.		d.l.		d.l.		d.l.		d.l.	
Total	92.9		98.5		93.9		97.0		96.8		93.6		97.9		99.7	

The uncertainties (2 σ) represent the standard deviation of average mineral analyses with Nr. representing the number of analyzed mineral spots per thin section; (d.l.) below detection limit. The concentrations of K not reported here were all below detection limit.

TABLE 5. (Continued)

	SL11-42	2 σ	SL11-42	2 σ	SL11-42	2 σ	SL11-9	2 σ	SL11-9	2 σ	SL11-7	2 σ	SL11-7	2 σ	SL11-4	2 σ	SL11-6	2 σ
Rock	Peg		Peg		Peg		Peg		Peg		Peg		Peg		Peg		Peg	
Mineral	Zrn		Zrn		Zrn		Zrn		Zrn		Zrn		Zrn		Zrn		Zrn	
Group	I		II		II		I		II		II		I		Inter.		I	
Nr	7		5		7		4		4		3		2		5		3	
SiO ₂	28.7	3.1	31.2	0.7	31.4	2.3	29.9	1.2	31.0	0.3	30.8	0.1	30.0	0.5	32.9	0.6	31.8	0.2
TiO ₂	0.06	0.04	0.07	0.01	0.07	0.02	0.10	0.07	0.24	0.04	0.18	0.06	0.07	0.01	0.16	0.03	0.09	0.00
Al ₂ O ₃	0.30	0.28	0.59	0.11	0.55	0.19	0.53	0.26	0.82	0.18	0.27	0.15	0.10	0.02	0.60	0.12	0.12	0.04
FeO	0.13	0.06	0.25	0.09	0.23	0.11	0.34	0.33	0.55	0.32	0.87	0.86	1.42	2.34	0.51	0.08	0.25	0.14
MnO	0.06	0.07	0.13	0.06	0.11	0.07	0.10	0.09	0.27	0.11	0.11	0.02	0.09	0.05	0.51	0.27	0.10	0.06
CaO	0.21	0.22	0.06	0.03	0.03	0.02	0.04	0.02	0.08	0.04	0.03	-	d.l.		0.10	0.08	0.04	0.01
Na ₂ O	0.24	0.10	0.44	0.07	0.42	0.14	0.39	0.08	0.28	0.16	0.32	0.12	0.32	0.08	0.32	0.33	0.31	0.04
P ₂ O ₅	0.67	0.80	0.13	0.11	0.15	0.13	d.l.		d.l.		d.l.		d.l.		0.09	0.05	0.56	0.12
F	1.74	1.37	0.91	0.27	0.95	0.27	0.78	0.21	0.47	0.24	0.49	0.15	0.58	0.04	0.49	0.15	0.57	0.17
HfO ₂	1.40	0.46	1.50	0.08	1.42	0.25	1.23	0.21	1.37	0.56	1.57	0.58	1.29	0.22	1.58	0.12	1.40	0.46
ZrO ₂	53.7	3.6	57.7	1.3	56.4	1.3	53.5	4.1	58.0	0.6	57.7	1.6	55.9	2.3	59.7	1.9	56.8	0.6
Nb ₂ O ₅	0.40	0.24	0.58	0.15	0.51	0.16	0.46	0.21	0.53	0.26	0.13	-	0.12	0.04	0.11	0.02	0.11	0.06
Y ₂ O ₃	3.98	1.76	2.79	1.15	3.52	1.91	4.44	1.36	1.33	0.23	2.83	0.69	4.02	0.19	0.96	0.41	3.97	0.98
La ₂ O ₃	d.l.		d.l.		0.07		d.l.		0.12	0.03	0.09	-	d.l.		d.l.		d.l.	
Ce ₂ O ₃	0.10	0.09	0.39	0.24	0.28	0.28	0.08	0.03	0.38	0.09	0.17	0.13	0.09	0.05	0.06	0.03	0.10	0.06
Pr ₂ O ₃	d.l.		0.13	0.06	0.11	0.05	d.l.		0.09	0.07			d.l.		d.l.		d.l.	
Nd ₂ O ₃	0.15	0.07	0.69	0.14	0.56	0.34	0.15	0.09	0.31	0.12	0.22	0.07	0.13	-	d.l.		0.08	0.01
Sm ₂ O ₃	0.09	0.10	0.23	0.08	0.24	0.09	0.13	0.06	0.12	-	0.11	0.03	d.l.		d.l.		0.07	
Eu ₂ O ₃	d.l.		d.l.		d.l.		d.l.		d.l.		d.l.		d.l.		d.l.		d.l.	
Gd ₂ O ₃	0.33	0.20	0.15	0.09	0.23	0.17	0.84	0.34	0.12	0.02	0.29	0.19	0.41	0.07	0.14	0.04	0.36	0.09
Dy ₂ O ₃	0.85	0.29	0.15	0.07	0.27	0.31	0.96	0.52	0.13	0.04	0.22	0.13	0.50	0.02	0.13	0.04	0.54	0.05
Er ₂ O ₃	0.74	0.30	0.11	0.09	0.19	0.24	0.71	0.36	0.13	0.08	0.24	0.05	0.59	0.14	0.15	0.11	0.57	0.16
Yb ₂ O ₃	2.28	1.50	0.24	0.09	0.41	0.44	1.31	0.73	0.37	0.15	0.72	0.09	1.24	0.03	0.35	0.13	1.24	0.41
Lu ₂ O ₃	0.33	0.24	0.05	0.03	0.07	0.05	0.18	0.10	0.09	0.02	0.12	0.03	0.19	0.06	0.06	0.01	0.16	0.07
Total	96.5		98.6		98.2		96.1		96.8		97.4		97.1		98.8		99.3	

TABLE 6. Average EMP analyses (in wt. %) of titanite from Strange Lake granites and pegmatites (Peg).

	SL11-155	2 σ	SL11-151	2 σ	SL11-106	2 σ	SL11-100	2 σ	SL11-104	2 σ	SL11-131	2 σ	SL12-47	2 σ
Rock	Granite		Granite		Peg		Peg		Peg		Peg		Vein	
Mineral	Titanite		Titanite		Titanite		Titanite		Titanite		Titanite		Titanite	
Nr.	10		10		6		18		3		4		18	
SiO ₂	30.1	0.8	30.5	0.4	30.4	0.6	29.8	0.9	30.2	0.4	31.9	2.1	30.3	0.6
TiO ₂	32.7	3.1	31.5	2.6	30.4	0.8	30.4	1.7	29.6	0.1	27.9	1.1	35.2	1.2
Al ₂ O ₃	0.72	0.29	d.l.		1.12	0.30	0.91	0.37	1.05	0.17	0.19	0.11	d.l.	
FeO	3.48	1.30	3.76	1.85	4.40	0.99	5.43	1.16	6.08	0.51	5.77	0.95	2.33	1.05
MnO	0.05	0.01	0.13	0.32	0.06	0.05	0.10	0.08	0.11	0.09	0.15	0.03	d.l.	
CaO	27.21	0.9	27.5	1.8	26.6	1.3	26.1	1.0	26.5	0.8	24.4	1.0	27.2	1.0
Na ₂ O	0.21	0.15	0.16	0.12	0.31	0.33	0.17	0.08	0.14	0.14	0.44	0.17	0.29	0.19
K ₂ O	d.l.		d.l.		d.l.		0.08	0.02	d.l.		d.l.		d.l.	
F	0.60	0.26	0.66	0.34	0.64	0.23	0.71	0.33	0.56	0.05	0.56	0.07	0.40	0.25
Y ₂ O ₃	0.12	0.07	0.40	0.24	0.52	0.22	d.l.		0.62	0.01	0.38	0.08	0.19	0.14
La ₂ O ₃	d.l.		0.17	0.24	0.07		d.l.		d.l.		d.l.		d.l.	
Ce ₂ O ₃	0.19	0.14	0.27	0.28	0.19	0.09	d.l.		0.61	0.16	d.l.		0.16	-
Pr ₂ O ₃	0.07	0.01	0.15	0.19	d.l.		d.l.		0.07	0.03	d.l.		d.l.	
Nd ₂ O ₃	0.13	0.05	0.28	0.28	d.l.		d.l.		0.28	0.10	d.l.		0.10	-
Sm ₂ O ₃	d.l.		d.l.		d.l.		d.l.		0.05	-	d.l.		d.l.	
Eu ₂ O ₃	d.l.		0.17	0.22	d.l.		d.l.		d.l.		d.l.		d.l.	
Gd ₂ O ₃	d.l.		0.08	0.05	d.l.		d.l.		0.08	0.05	d.l.		0.11	-
Dy ₂ O ₃	d.l.		d.l.		d.l.		d.l.		0.06	-	d.l.		d.l.	
Er ₂ O ₃	d.l.		d.l.		d.l.		d.l.		0.07	-	0.09		d.l.	
Yb ₂ O ₃	d.l.		0.07	0.02	0.14	0.09	d.l.		0.17	0.03	0.11	0.08	d.l.	
Total	95.41		94.64		94.77		95.60		96.13		91.81		95.98	

The uncertainties (2 σ) represent the standard deviation of average mineral analyses with Nr. representing the number of analyzed mineral spots per thin section; (d.l.) below detection limit. The concentrations of Lu not reported here were all below detection limit.

TABLE 7. Average EMP analyses (in wt. %) of pyrochlore-(Nb) from Strange Lake granites and pegmatites (Peg).

	SL11-80	2 σ	SL11-179	2 σ	SL11-158	2 σ	SL11-9	2 σ	SL11-40	2 σ
Rock	Granite		Granite		Granite		Peg		Peg	
Nr.	14		10		10		15		3	
SiO ₂	1.19	2.20	0.69	0.72	0.28	0.39	1.15	0.40	1.31	0.13
TiO ₂	4.69	2.36	4.51	1.64	2.70	2.07	4.57	0.65	5.47	0.31
FeO	0.35	0.37	0.56	0.40	0.28		d.l.		d.l.	
MnO	0.11	0.15	d.l.		0.06	-	0.05	-	d.l.	
CaO	2.57	1.26	4.56	1.32	3.41	1.36	4.46	0.40	4.98	0.09
Na ₂ O	6.22	3.90	8.76	3.03	5.90	3.72	8.68	2.41	8.65	0.21
F	4.14	3.01	5.63	1.09	5.15	1.51	5.26	0.90	6.17	0.66
ZrO ₂	0.40	0.08	0.27	0.19	0.18		0.33	0.14	0.36	0.07
Nb ₂ O ₅	56.5	5.2	57.6	5.4	61.7	4.4	56.2	1.4	55.3	0.7
Ta ₂ O ₅	2.26	1.91	2.49	1.83	1.94	0.98	3.51	0.35	3.45	0.24
ThO ₂	0.20	0.17	d.l.		d.l.		d.l.		d.l.	
UO ₂	0.98	1.13	0.20	0.14	0.46	0.49	0.15	0.04	0.13	0.03
Y ₂ O ₃	0.29	0.20	0.17	0.05	0.15	0.07	0.17	0.06	0.18	0.07
La ₂ O ₃	4.39	0.46	4.64	0.62	5.61	1.47	4.24	0.24	4.25	0.18
Ce ₂ O ₃	10.82	0.69	10.75	0.52	11.19	0.59	10.51	0.30	10.32	0.10
Pr ₂ O ₃	1.01	0.15	0.97	0.08	0.90	0.33	0.99	0.10	0.98	0.09
Nd ₂ O ₃	2.33	0.31	2.47	0.15	2.18	1.03	2.47	0.17	2.28	0.06
Sm ₂ O ₃	0.23	0.15	0.19	0.04	0.18	0.07	0.22	0.05	0.20	0.03
Gd ₂ O ₃	0.18	0.12	d.l.		d.l.		0.14	0.02	0.13	
Dy ₂ O ₃	0.24	0.10	d.l.		d.l.		d.l.		d.l.	
Total	99.1		104.4		102.3		103.1		104.2	
O=F	1.7		2.4		2.2		2.2		2.6	
Total	97.4		101.5		100.1		100.9		101.6	

The uncertainties (2 σ) represent the standard deviation of average mineral analyses with Nr. representing the number of analyzed mineral spots per thin section; (d.l.) below detection limit. The concentrations of Lu, Yb, Er, Eu, Al and K not reported here were all below detection limit.

TABLE 8. Link between alteration types and bulk rock chemistry with key lithogeochemical vectors for alteration types related to ore mineralization.

Alteration type	Bulk rock ratios	Controlling reactions
High T acidic alteration (IIIa)		
<i>Aegirinization/hematization</i>		
Arf to Aeg+Hem+Qtz	Fe ₂ O ₃ /Na ₂ O	$\text{Na}_3\text{Fe}^{2+}_4\text{Fe}^{3+}\text{Si}_8\text{O}_{22}(\text{OH})_2 + 2\text{H}^+ = \text{NaFe}^{3+}\text{Si}_2\text{O}_6 + 2\text{Fe}^{3+}_2\text{O}_3 + 6\text{SiO}_2 + 2\text{Na}^+ + 2\text{H}_{2(\text{g})}$
<i>Ca-metasomatism (pseudomorphs)</i>		
Elp to Git+Qtz	CaO/Na ₂ O	$\text{Na}_2\text{ZrSi}_6\text{O}_{15} \cdot 3\text{H}_2\text{O} + \text{Ca}^{2+} = \text{CaZrSi}_2\text{O}_7 + 4\text{SiO}_2 + 2\text{Na}^+ + 3\text{H}_2\text{O}$
Low T acidic alteration (IIIb)		
<i>Ca-F-metasomatism</i>		
Kfs to Git+Qtz	CaO/K ₂ O, CaO/Al ₂ O ₃	$\text{KAlSi}_3\text{O}_8 + \text{ZrF}_2(\text{OH})_2 + \text{Ca}^{2+} = \text{CaZrSi}_2\text{O}_7 + \text{SiO}_2 + \text{K}^+ + \text{AlF}_2^+ + \text{H}_2\text{O}$
Aeg to Zrn+Fl+Qtz	CaO/Na ₂ O	$2\text{NaFe}^{3+}\text{Si}_2\text{O}_6 + \text{ZrF}_2(\text{OH})_2 + \text{Ca}^{2+} = \text{ZrSiO}_4 + \text{Fe}^{3+}_2\text{O}_3 + 3\text{SiO}_2 + \text{CaF}_2 + 2\text{Na}^+ + \text{H}_2\text{O}$

APPENDIX

TABLE A1. Electron microprobe standards, count times and detection limits used in this study.

Element	Standard	Crystal	Background (sec)	Counting time (sec)	Detection limit (wt. % oxides)
Si	Diopside	TAP	10	20	0.02
Ti	TiO ₂	PETJ	10	20	0.02
Al	Orthoclase	TAP	10	20	0.02
Fe	Fe ₂ O ₃	LIF	10	20	0.02
Mn	Spessartine	LIF	10	20	0.02
Ca	Diopside	PETJ	10	20	0.02
Na	Albite	TAP	10	20	0.09
K	Orthoclase	PETJ	10	20	0.04
P	Apatite	PETJ	10	20	0.03
F	CaF ₂	TAP	10-50	20-100	0.08
Zr	Zircon	PETJ	10	20	0.02
Hf	Zircon	LIF	10	20	0.04
Nb	Na ₂ Nb ₂ O ₆	LIF	10	20	0.04
Ta	K ₂ Ta ₂ O ₆	LIF	50	100	0.20
Th	ThO ₂	PETJ	50	100	0.03
U	UO ₂	PETJ	50	100	0.05
Y	MAC-Y	PETJ	10	20	0.07
La	MAC-La	LIFH	30	60	0.05
Ce	MAC-Ce	LIFH	30	60	0.03
Pr	MAC-Pr	LIFH	30	60	0.06
Nd	MAC-Nd	LIF	50	100	0.06
Sm	MAC-Sm	LIFH	40	80	0.05
Eu	MAC-Eu	LIFH	50	100	0.04
Gd	MAC-Gd	LIFH	25-30	50-60	0.06
Dy	MAC-Dy	LIFH	30	60	0.06
Er	MAC-Er	LIF	40	80	0.04
Yb	MAC-Yb	LIFH	25-30	50-60	0.03
Lu	MAC-Lu	LIF	50	100	0.04



Click here to access/download
Electronic Appendix (Excel etc.)
Supplementary Material.xlsx

